KU LEUVEN

FACULTEIT WETENSCHAPPEN

Modelling of laser-atom interactions for improving efficiency in nuclear laser spectroscopy research.

Matthias VERLINDE

Promotor: Prof. Dr. Gerda Neyens
KU Leuven

Begeleider: Ruben de Groote
KU Leuven

Proefschrift ingediend tot het
behalen van de graad van
Master of Science in de Fysica

Academiejaar 2015-2016

Abstract

This thesis deals with the application-oriented study of laser-atom interactions in nuclear physics research methods.
In the first part of this work, the continuation of the study of a quantum mechanical model, first reviewed in [1], describing the interaction between a coherent light source and free atoms in space, is presented. This model allows for simulations which are of vital importance to better control the resonant ionization laser spectroscopy experiments (RIS), which are developed to obtain detailed information about the electromagnetic structure of the atomic nucleus by probing the hyperfine interaction. In this work, the existing model has been supplemented with some theoretical features, such as spontaneous decay of discrete quantum levels. Including these additional physical effects should make the model more realistic. The added theoretical considerations are interpreted and their influence on experimentally important parameters is discussed in both a mathematical and an intuitive manner.
Previous work in [1] already synthesized a method for optimizing the spectral resolution in RIS experiments. In light of these improvements, the current thesis presents a method which additionally allows maximizing the experimental efficiency of such a RIS experiment. Both results are in line with the new general recommendations made in this work, favoring the use of weak atomic transitions with small Einstein A parameters for high resolution and high efficiency laser spectroscopy research using RIS. Finally, the improved model is tested on experimental data sets, confirming its validity.
As a second part of this thesis, a similar mathematical model is applied to a three-level scheme with the sole purpose of maximizing coherent light excitation between atomic levels, via an intermediate state. The model is first extensively characterized and then followed by a study of a number of possible applications in nuclear physics laser spectroscopy experiments. For each proposed experimental situation, this new scheme is compared to an already existing procedure while its advantages and downsides are discussed. The optical pumping method employed in some beam-lines for atomic population transfer to a meta-stable state is one application for which this method promises improvements.

Samenvatting

De focus van deze thesis rust op een toepassingsgerichte studie van laser-atoom interacties. In het eerste deel van deze thesis wordt onderzoek gedaan naar een reeds bestaand model dat werd uitgewerkt in [1]. Dit model bracht de interactie tussen coherente laser straling en vrije atomen in kaart, zowel theoretisch als via simulaties, met de focus naar het optimaliseren van resonante laser ionizatie experimenten (RIS). Deze RIS-experimenten hebben als bedoeling de karakteriserende momenten van de atoomkern te bepalen aan de hand van de hyperfijn interactie.
De bedoeling van dit werk is, vertrekkende van [1], de experimentele laser-gerelateerde omstandigheden verder te optimaliseren aan de hand van theoretische argumenten en simulaties op het model. Deze thesis biedt een 'in depth' beschrijving van dit model, aangevuld met theoretische observaties om het zo dicht mogelijk de werkelijkheid te laten benaderen. Deze addities worden eerst en vooral toegelicht en daarna toegevoegd aan de simulatiecode. De invloed van deze toevoeging wordt achteraf besproken. Ten slotte wordt aan de hand van experimentele data de validiteit van het model besproken.
Volledig parallel met de optimalisatie procedure omtrent de spectrale resolutie, besproken in [1], wordt in deze thesis extra materiaal ter versterking hiervan aangeboden. Daarbovenop wordt een nieuwe methode toegelicht die toelaat om de experimentele efficiëntie te optimaliseren. Als conclusie worden atomaire transities met kleine Einstein A parameters uitgelicht als ideale studiebronnen voor laser spectroscopie experimenten.
Het tweede deel van deze thesis draait rond de beschrijving van een methode die toelaat om de excitatie efficiëntie tussen twee discrete kwatummechanische toestanden in het ideaal geval tot 100 percent te verhogen. Dit is mogelijk door gebruik te maken van een drie-staps kwantumschema en twee coherente laser bronnen. Deze methode wordt met de hulp van literatuur gekarakteriseerd en een model, die het mogelijk maakt fysische fenomenen te simuleren, werd ontwikkeld. Potentiële toepassingen in kern-fysische experimenten worden daarna voorgesteld. In alle gevallen worden zowel voordelen als nadelen van deze techniek besproken in vergelijking met bestaande methodes. Concreet, voor experimenten waarin via optisch pompen de populatie van een atomair ensemble in een metastabiele toestand wordt gebracht, wordt aangetoond dat deze nieuwe methode toelaat om minstens even efficient alsook in een veel kortere tijdspanne populatie overdracht te realiseren.

Layman's Summary

The atomic nucleus is a complex entity for which, to this day, no exact theoretical description is developed. In an effort to describe this nucleus experimentally, nuclear physics has devoted great interest towards measuring nuclear parameters, which could help in understanding more about the foundations of matter. These parameters are called the nuclear moments. They describe the electromagnetic structure of the nucleus and they can be compared directly to predictions from state of the art nuclear theories to test their validity. One of the experimental methods used to obtain these nuclear moments and on which the main focus of this thesis lies, is called Resonant Ionization Spectroscopy (RIS). Individual electrons, surrounding the nucleus, can only occupy discrete levels, called atomic orbitals, determined by the rules of quantum mechanics. These orbitals determine the whereabouts and a set of features for a particular electron. Via the interaction with laser photons, these electrons can jump from one orbital to another by absorbing a photon, as long as the law of conservation of energy is obeyed. Laser transitions, matching the energy splittings, thus allow for a determination of the energy differences between particular orbitals, via a very precise control of laser photon energy. Considering the fact that the energy levels of the individual orbitals are influenced by the electromagnetic interaction between the electronic fields and the nuclear moments, RIS experiments can determine the nuclear moments in an indirect way from these energy splittings. However, the contribution of the nuclear-moment interaction to the energy levels of the orbitals is often rather small and the most interesting elements, nuclei with very unstable configurations of neutrons and protons, are very rare and short lived. Therefore, the focus in RIS experiments lies in obtaining a maximum spectral resolution alongside as high as possible efficiency. The resolution will determine the maximum precision in measuring the orbital's energy differences while the efficiency concludes on the minimum production rate of the specific element required for it to be measured at all. A proper understanding and control of the interactions between atoms and laser photons is thus a vital element in possible optimization procedures for these RIS experiments.

With the info obtained via simulations on a model, an array of general guidelines is presented, concerning the laser and atomic-orbitals characteristics, to optimize a laser spectroscopy experiment like RIS in precision, accuracy and efficiency.

In the second part of this thesis, the developed simulation code will be further extended with the goal to simulate a recently developed theoretical method. In this method, one tries to maximize the efficiency of exciting electrons from one orbital to the other, which is located at a higher energy level via a radical new scheme. For this to work, the method requires two lasers and one additional orbital next to the two of interest. The two lasers work in sync to make the transition process as efficient as possible by using the additional level as a stepping stone. The particular characteristics of this level are however of minor importance, explaining the robustness of the method. This thesis will present a feasibility study concerning the application of this technique in multiple nuclear physics methods.

Vulgariserende samenvatting

De atoomkern is een complex geheel, waarvoor tot op heden nog geen exacte theoretische beschrijving ontwikkeld is. Omwille van het feit dat de kern de hoeksteen van de materie vormt en de nood aan experimentele input voor opkomende theorieën bestaat, wordt momenteel in de experimentele kernfysica aandacht besteed aan het bepalen van enkele meetbare parameters die de kern karakteriseren. Deze parameters worden de kernmomenten genoemd. Ze bepalen in algemene termen de elektromagnetische structuur van de kern en kunnen rechtstreeks berekend worden met huidige kernmodellen, zodat aldus hun voorspellende waarde kan getest worden. Een van de manieren waarop deze momenten experimenteel bepaald worden, en waarop de focus van de thesis ook ligt, is de RIS techniek, ofwel 'resonante laser ionisatie spectroscopie'. De individuele elektronen rondom de atoomkern kunnen slechts in welbepaalde, door de kwantummechanica gedicteerde discrete, atomaire orbitalen aanwezig zijn. Via de interactie met lasers kunnen elektronen echter van atomaire toestand veranderen, zolang aan de wet van behoud van energie voldaan wordt. Via laser transities, met een correcte overgangsenergie, kunnen, met een precieze controle van de laser foton energie, deze energieverschillen gemeten worden. Aangezien de energie van deze atomaire toestanden beïnvloed wordt door de kernmomenten kan een RIS experiment dan aan de hand van deze waardes de kernmomenten bepalen. Omdat deze energieverschillen, die bepaald worden door de interactie met de kern, enorm klein zijn en de meest interessante, exotische atomen in kwestie zeldzaam, ligt bij deze experimentele methode de focus op een zo hoog mogelijke spectrale resolutie en efficiëntie te bekomen. De maximaal haalbare spectrale resolutie zal bepalen wat de precisie is op het bepalen van de energieverschillen terwijl de efficiëntie bepaalt hoe zeldzaam de specifieke kern mag zijn opdat deze nog meetbaar zou zijn. Een goed begrip van en controle over de interactie tussen atomen en laser fotonen is dus een belangrijk element in de optimalisatie procedure voor deze experimenten.
Met behulp van simulaties op een model, zal een lijst van algemene richtlijnen, met betrekking tot de laser-atoom interacties, geformuleerd worden voor het optimaliseren van een laser spectroscopie experiment in precisie, nauwkeurigheid en efficiëntie.
In een tweede deel wordt de ontwikkelde code verder uitgebreid om een relatief recente methode theoretisch te simuleren. In deze methode probeert men de transitie van een atomaire toestand naar een ander (energetisch hoger gelegen) zo efficiënt mogelijk te laten gebeuren, via het gebruik van een tussenliggende toestand en twee lasers. Hierbij wordt dit extra atomaire niveau via 2 lasers zowel aan het initiële als aan het finale orbitaal gekoppeld. Intuïtief gezien, wordt het middelste orbitaal in feite amper bevolkt worden door elektronen maar het maakt de overtocht naar het uiteindelijke niveau eenvoudiger. In deze thesis wordt een toepasbaarheidsstudie ondernomen die nagaat of deze methode zou kunnen toegepast worden in bestaande technieken van de nucleaire fysica.

Acknowledgments

> Wanderer, your footsteps are the road, and nothing more; wanderer, there is no road, the road is made by walking. By walking one makes the road, and upon glancing behind one sees the path that never will be trod again. Wanderer, there is no road, only wakes upon the sea.
>
> *Antonio Machado, Campos de Castilla*

Aangezien deze thesis schrijven een volledig hopeloze onderneming zou zijn geweest wanneer ik het helemaal op mijn eentje had moeten doen, lijkt het mij gepast enkele mensen te bedanken.

Eerst en vooral zou ik graag een woordje van dank richten tot mijn promotor, prof. dr. Gerda Neyens. Hoe druk bezet uw agenda ook was, uw deur stond altijd open voor een gesprek of discussie. Het enthousiasme waarmee u uw werk doet en erover vertelt zou een voorbeeld mogen zijn voor eender wie. Bedankt!
Next a word of gratitude aimed towards the nuclear moments group at IKS and the people at CERN, Xiaofei, Hanne, Agi, Wouter, Greg, Shane, Kara, Thomas and Ronald. Thank you for coming to my aid at any moment with every question I had, the stupid ones and the little bit less stupid ones, during both my thesis and my time at CERN. Wouter, thank you for solving so many of my computer related issues. Thanks!

Als volgende zou ik mijn begeleider extra willen bedanken. Bedankt Ruben voor het koeltjes volhouden met de eindeloze stroom aan vragen, mijn soms ongefundeerd enthousiasme te temperen, mij op dode momenten van onwaarschijnlijk nuttige vragen en antwoorden te voorzien en tijd te maken om met mij te skypen wanneer je het meer dan druk had in CERN. Maar vooral bedankt om mij een glimps te laten opvangen van jouw manier van denken, de sessies aan het bord hebben mij geleerd elk aspect van het probleem geen twee, maar drie keer te bekijken, een heel waardevolle les. Heel hard bedankt!

Als volgende zou ik mijn vrienden willen bedanken, vanaf de eerste weken van mijn studie carrière zijn jullie een bron van ontspanning en plezier geweest, meer dan bedankt hiervoor!

Ten slotte, zou ik graag mijn ouders bedanken. Ten eerste voor het cliché dat ik hier zonder jullie nooit had gestaan. Clichés blijken echter vaak juist te zijn... Bedankt vervolgens voor de nooit aflatende steun en raad die jullie altijd op eender welk moment klaar hadden staan. Merci!
Ik weet dat het jullie droom was geweest mij talen te zien studeren. Het spijt me zeer dat die droom nooit in vervulling is gegaan ☺.

Ik hoop dat ze toch even gedacht heeft dat ik haar vergeten was. Last but certainly not least, zou ik Alexandra willen bedanken. Ik heb meer aan haar dan ze ooit zal beseffen en ik zou het voorbije jaar niet eens kunnen, laat staan willen, inbeelden zonder haar aan mijn zijde.

-Matthias -

Contents

List of Acronyms and Symbols

RIS: Resonant Ionization Spectroscopy

ISOLDE: Isotope Separator On Line DEvice, experimental nuclear physics hall at CERN

CERN: Conseil Européen pour la Recherche Nucléaire

COLLAPS: COLlinear Laser SPectroscopy

CRIS: Collinear Resonant Ionization Spectroscopy

STIRAP: STImulated Rapid Adiabatic Passage

gs: Ground State

es: Excited State

$\mathbf{A}_<$ Weak Transitions, Einstein A parameter $< 10^6$MHz

$\mathbf{A}_>$ Strong Transitions, Einstein A parameter $> 10^6$MHz

$\boldsymbol{\Omega}$**:** Rabi Frequency, $-\vec{d} \cdot \vec{E}/\hbar$

$\boldsymbol{H}$**:** Hamiltonian

$\boldsymbol{\Delta}$**:** Laser Detuning

$\boldsymbol{\rho}$**:** Density Matrix

$\boldsymbol{\Lambda}$**:** Lindblad Super Operator

A: Einstein A parameter (s^{-1})

I: Laser Intensity ($J/(m^2 s)$)

I,L,S,J,F: Nuclear Spin, Electronic Angular Momentum, Electronic Spin, Coupled L and S, Coupled I and J

Foreword

Standard shell model calculations and other nuclear theories are sufficiently accurate in describing and predicting new properties of the nuclei close to stability. Once more exotic nuclei are probed, having a growing instability in their proton-neutron configuration, new and unexpected features, not covered by basic theories, are brought to light. One of the most striking deviations is found in the evolution of the well-known magic numbers. For example, adding neutrons to already exotic isotopes can alter the shell structure of the protons and even induce new magic numbers. It is therefore clear that theoretical models should include these features, thus they should be updated. Without experimental data to compare with new theoretical predictions, this is however a futile attempt.
Experimental observables shedding light on this topic include g-factors, charge radii and nuclear quadrupole moments. These nuclear moments are highly interesting as they can be measured in a model independent way. In addition to this, they can be compared to predictions by different theoretical models to test their validity. To state the significance of these observables, one can look at the g-factors which are very sensitive to the outer occupied nuclear orbits and therefore highlight nuclear structure properties. On the other hand, the electric quadrupole moment of a nucleus offers information on the geometrical electromagnetic architecture of the nucleus. In a high-resolution laser spectroscopy experiment both the g-factor and quadrupole moment, but also the charge radius and the nuclear spin can be determined. One of the possible places to do this kind of experiments is the ISOLDE facility at CERN, Geneva. Two collinear laser spectroscopy beam lines are operational there, COLLAPS since more than 40 years and CRIS since 2012.
In this report, the focus is put on the CRIS (RIS in general) setup, which has been constructed for improving the efficiency of high-resolution laser spectroscopy and thus allowing studies on the most exotic species. Details on this experimental technique are given in **appendix A**. The spotlight of this work is on the atomic physics part of the technique. In a CRIS experiment, the atoms of particular interest are resonantly excited to an unstable excited level above the atomic ground state and afterwards ionized by a second laser. By scanning the first laser, the possible underlying hyperfine structure of the ground or excited state, which is due to the interaction between the electron cloud and the nuclear moments, can be brought to light. This underlying structure contains vital information on the nuclear moments.

Two experimental parameters are strongly dependent on the interaction of the laser photons with the atoms of choice: resolution and efficiency. Improvements on the resolution front offer a more precise determination of the underlying hyperfine level structure, and thus the nuclear moments. On the other hand, the more exotic the nucleus is, the smaller its production rate and therefore the larger the required experimental measuring efficiency has to be. The subject of this thesis is focused on simulations that can help in optimizing a laser spectroscopy

experiment, like for example CRIS, by altering the laser set-up characteristics to achieve the highest possible efficiency and resolution which is of uttermost importance in tackling these very exotic isotopes.
An existing model, describing the interaction between different kind of lasers and multiple quantum mechanical levels, will be elaborated on and discussed in **Chapter 1**. New theoretical features will be implemented in this model and their influence on the vital characteristic parameters and goals for such laser spectroscopy experiments is examined in **Chapter 2**. To tackle the optimization process, the available python simulation code, based on the existing model was updated with new features. A graphical user interface has been developed, allowing easy and fast simulations of ionization laser spectroscopy experiments in the future.

Previous work, [1], studied one degree of freedom which reveals itself when working with pulsed lasers, namely the relative position in time of the two pulses with respect to each other. This work will elaborate further on this degree of freedom and will formulate an array of features, all involving resolution and efficiency, in favor of using weak atomic transitions for laser spectroscopy experiments. Two of these features are inherent to the weak transitions: they possess a smaller inherent linewidth and they are easier to saturate. In addition to this, probing weak transitions with separated laser pulses should optimize the precision and accuracy as argued in [1]. For a weak transition, delaying the ionization pulse with respect to the resonant excitation pulse has no significant effect on the efficiency because of their inherently slow spontaneous decay. Finally it seems that the ionization efficiency when using weak transitions in RIS-experiments can be maximized by playing around with a new degree of freedom; the laser pulse length of the resonant step. All of these features will be thoroughly explained and their influence checked by simulations in **Chapter 3**. The validity of the model is also scrutinized by experimental comparison in **Chapter 4**. In **appendix B** a paper, which is in preparation, is presented using a few of the results from this work and more details on the experiments and results discussed in chapter 4.

As a second part to this thesis, another interesting feature of laser-atom interactions is studied, STImulated Rapid Adiabatic Passage or STIRAP. STIRAP presents a two- or more laser based efficient excitation procedure and is explained in **Chapter 5**. In a roughly defined ideal parameter range, the population transfer mechanism presented by STIRAP offers 100 percent efficiency by sculpting an adiabatic pathway through a multilevel scheme. This method has been around for a long time in a wide array of physics-branches, however it has as far as we know, never been used for nuclear physics related applications. Often laser related methods in nuclear physics, as for example the before mentioned laser spectroscopy methods, evolve around efficient excitation from one quantum level to another. Therefore considerations on the relevance of the excitation efficiency are of vital importance. Thus, a few applications are simulated from the ground onward in **Chapter 6** with the intention of testing their possible applicability for nuclear physics experiments. Practical and theoretical considerations are presented. One particular application, employing STIRAP as efficient and fast optical pumping, offers promising results.

Part I

Atom-Photon Interactions

Chapter 1

Theoretical Background

In this chapter, a basic model for describing photon-atom interactions is introduced. Starting from the description of this phenomenon in a two level system, a scheme is introduced which allows for a generalization towards an arbitrary number of states. Both coherent excitation and incoherent ionization via lasers will be discussed. This model will constitute the basis of all following chapters. The focus will lie on the relevant laser-atom interactions in a RIS experiment. An example of such an experiment, including collinear geometry, is called CRIS, which is introduced in appendix A. This appendix is important to keep in mind when coupling theory and experiment as is done at the end of each section in this chapter.

1.1 Introduction

The work covered in this chapter is a review of previous work in [1]. In this work, the interaction between two monochromatic laser beams (pulsed and continuous) and an atomic system is described via a quantum mechanical model, complemented with experimental input parameters. In this way, the simulation results can be more easily compared with experimental results.
The main focus of the study in [1] is to understand the influence of inter laser characteristics on the obtained ionization spectra of for example a CRIS experiment. To understand the origin of this spectrum, the reader is referred to appendix A. In this work the intra characteristics are supplemented to the discussion. The inter laser characteristics contain the information on the time delay between both pulses while the intra laser characteristics focus more on the temporal behavior of a particular laser pulse itself. In the following sections, the theoretical description covered in [1] is briefly presented such that the basics in laser-atom interactions are clear and can be used as a starting point in the following chapters. There, the model will be extended to include physics processes that were omitted so far.

1.2 Two-Level Excitation

In this section, the coherent excitation of a simplified two-level atomic scheme is presented. Describing a two level atom interacting with laser light of frequency ω_a is done here in the degenerate bare atom-photon quantum mechanical basis $|0, n\rangle, |1, n-1\rangle$ following the Jaynes-Cummings model [2]. Here $|0, n\rangle$ is interpreted as the atom being in its ground state (gs) surrounded by n laser photons. $|1, n-1\rangle$ can then be seen as the same atom being now in the

excited state (es) surrounded by one photon less. In this bare basis, the laser-atom interaction can be described by the following Hamiltonian (in rotating wave approximation):

$$H = \begin{pmatrix} \omega_0 & g \\ g^* & \omega_1 - \omega_a \end{pmatrix}. \tag{1.1}$$

The off-diagonal elements represent the coupling between the gs and es of the atom due to the laser-atom interaction. From now on, the coupling g will be assumed real. This can be assured by including an arbitrary phase factor. The time dependence of the oscillating electric field of the laser pulse has been taken into account by moving the problem into the rotating frame, explaining the $-\omega_a$ on the diagonal. As a consequence of this coupling, the chosen atomic basis is not an eigenbasis anymore of the Hamiltonian (1.1) and transitions between the bare states are allowed. An easy way to see this, is by looking at the quantum dynamics. Schrödinger's equation of motion can be solved for the state vector to obtain the population of the excited level as a function of the laser frequency and time. Doing this for a time-independent Hamiltonian (which implies the use of cw lasers) results in the famous Rabi oscillations. Applying the time-evolution operator to the initial state causes the state vector to become an oscillatory linear combination of both gs and es. The Rabi oscillations therefore imply that the population in the es will oscillate between empty and populated with a particular frequency and amplitude which depends on the laser frequency, laser intensity and internal coupling strength. The transition efficiency, or the overlap between the excited bare state and the state vector, will be greatly enhanced, depending on the frequency ω_a of the laser, when the off-diagonal terms become comparable in magnitude with the nearly degenerate diagonal terms (the degeneracy is complete when $\omega_a = \omega_1 - \omega_0$). Tackling the solution for a more general time-dependent Hamiltonian (meaning $g = g(t)$, for pulsed lasers for example) requires the adiabatic principle, on which will elaborated later on. The model however will remain the same.

From this discussion it is clear that the g parameters in the off-diagonal terms are related to the transition strength. They are in general determined by the matrix element $\langle\psi_i|O|\psi_f\rangle$. In this general matrix element, ψ_i and ψ_f represent the atomic wave functions which interact with an operator O. In the case of electron excitation via laser photons, often only dipole interaction is considered. This dipole operator $O = -\vec{d}\cdot\vec{E}$ is the interaction energy from the interplay of the electric field vector $(\vec{E})$ of the incoming photon and the dipole moment $(\vec{d})$ of the atom. The energy contained in this interaction can induce therefore a jump in the atomic wave function. Theoretical work done in [3] leads to an expression for this interaction strength, which not only depends on the quantum numbers J and F of the initial and final states, but also on the laser photon density P and the nuclear spin I.:

$$\begin{aligned} g^2 = {} & \frac{e^2\pi}{m\epsilon_0}\frac{P_1}{\omega_1-\omega_0} f(J_0,J_1)(2J_0+1)(2F_0+1)(2F_1+1) \\ & - \begin{pmatrix} F_1 & 1 & F_0 \\ -m_{F_1} & 0 & m_{F_0} \end{pmatrix}^2 \begin{Bmatrix} J_1 & F_1 & I \\ F_0 & J_0 & 1 \end{Bmatrix}^2. \end{aligned} \tag{1.2}$$

The oscillator strength f now depends only on the fundamental matrix element and values can be found for example in the NIST Atomic Spectra Database from the National Institute of Standards and Technology, Gaithersburg, MD. The normal brackets present a Wigner $3J$ symbol while the curly brackets imply the presence of a $6J$ symbol.

Having found the relevant Hamiltonian, diagonalization of this matrix will reveal the eigenstates of the interacting laser-atom system. It follows that these 'dressed' states can be written as a linear combination of the bare states:

$$\begin{pmatrix} |-,n\rangle \\ |+,n\rangle \end{pmatrix} = \begin{pmatrix} cos(\theta) & -sin(\theta) \\ sin(\theta) & cos(\theta) \end{pmatrix} \begin{pmatrix} |0,n\rangle \\ |1,n-1\rangle \end{pmatrix}, \tag{1.3}$$

where $\theta = \theta(t) = 0.5 \arctan\left(\frac{2g(t)}{\Delta_{01}}\right)$ and $\Delta_{01} = \omega_1 - \omega_0 - \omega_a$, the laser detuning from resonance. These 'dressed' states are also called the adiabatic states. A deeper understanding of these quantum states is given later.
As described in appendix A, in a RIS experiment, the excitation laser frequency is scanned. The population in the excited state then forms a Voigt profile in frequency space around the resonance frequency of the transition.

1.3 Two-Level Ionization

In this section, the interaction of an incoherent ionization laser with the atomic system is described. An intuitive way of adding the ionization process to the previous model description implies dealing with non-Hermitian Hamiltonians. For these kinds of Hamiltonian operators, the total population in the system is not preserved. This feature is the quantum mechanical equivalent of population loss from the atomic system due to ionization. Non-Hermitian Hamiltonians can have by definition imaginary eigenvalues. This imaginary nature of the eigenvalues will be responsible for exponential damping of the population in the states for which the imaginary part of the eigenvalues is non zero. Taking one state $|1\rangle$ coupled to a continuum via an ionization laser modeled by $V = V(t)\cos(\omega_b t + \Phi(t))$ at frequency ω_b one can start from:

$$|\psi, t\rangle = b_1(t)|1\rangle + \int d\epsilon b_\epsilon |\epsilon, \omega_\epsilon\rangle. \tag{1.4}$$

With the structure less continuum described by the states $|\epsilon, \omega_\epsilon\rangle$. Using this description of the system and applying the Schrödinger equation, RWA and Markov approximations to (1.4) gives a complicated expression for the time derivative of the population of state $|1\rangle$. Introducing however following variables is enlightening:

$$\Gamma(\omega_\epsilon, t) = \frac{\pi}{2}|\langle 1|V(t)|\epsilon, \omega_\epsilon\rangle|^2 \rho(\omega_\epsilon), \tag{1.5}$$

$$\delta\omega(t) = \frac{1}{4} P \int_0^\infty \rho(\omega_\epsilon) \frac{|\langle 1|V(t)|\epsilon, \omega_\epsilon\rangle|^2}{\Delta_{\epsilon 1}}. \tag{1.6}$$

Rewriting the time dependent overlap between the state vector and $|1\rangle$, $c_1(t)$, by introducing these two definitions reveals their influence on the quantum dynamics. Simplifying further by assuming a time independent Hamiltonian (cw ionization laser), one obtains following equation,

$$c_1(t) = \exp(-\Gamma t) \exp(-i(\omega_1 + \delta\omega)t))\, c_1(0). \tag{1.7}$$

(1.7) shows that $\delta\omega(t)$ represents an energy shift to the original level due to the coupling with the continuum. This energy shift is called an ac-Stark shift. The $\Gamma(\omega_\epsilon)$ term will cause the exponential damping of the level population. Therefore this factor will be approximated by the expression $\Gamma = \sigma P_2$, where σ is the cross section for ionization and P_2 is the power density

in the ionization laser. This definition will also be utilized in the simulations. The validity of the approximation can be made more plausible by looking at the expression defining Γ and its influence on the energy shift. In this work, the focus of the ionization laser is aimed towards ionizing a hyperfine multiplet. The electron configuration in such a multiplet has the same wave function for all F-states and therefore the matrix elements defining (1.5) will be of similar value for every atomic state. This means that instead of requiring each matrix element to be calculated from theory separately, this approximation will give one general energy shift and ionization rate to the entire hyperfine multiplet. The addition of an ionization laser to the atomic system therefore causes population damping and possibly a shift in the energy of the atomic states it ionizes.
To conclude this first attempt at describing the excitation-ionization process, the total Hamiltonian (for simplicity with the energy of the gs equalized to zero) in the bare atomic basis, with rotating coordinates, governing this process is shown,

$$H_{tot} = \begin{pmatrix} 0 & g(t) \\ g(t) & \Delta_{01} - \frac{1}{2}i\Gamma \end{pmatrix}. \tag{1.8}$$

In a RIS experiment, for each value of the excitation laser wavelength, the population in the excited state is ionized and the ions are then counted. The final result of a RIS experiment will therefore consist of a peak in the ion count rate, corresponding to the resonance, as a function of the excitation laser frequency. Important features of this resonance peak are the precision and accuracy. Both are strongly influenced by the specific laser-atom interactions and should be as high as required by the experimental circumstances.

1.4 Power Broadening

The laser intensity of excitation or ionization laser is an important parameter determining the obtained precision in a RIS experiment. Increasing this intensity will increase the yield of ions at each frequency step, but at the same time it will deteriorate the precision due to power broadening.
The effect of power broadening can be explained using the formulas obtained in previous sections and also in a more intuitive way. The mathematical explanation can be found in [1]. Here, one deals with the fact that when the population on resonance is starting to saturate, the population off resonance increases more rapidly with laser power than the population on resonance. The intuitive explanation is also briefly explained here. First of all, one can use the uncertainty principle applied to the quantum states of the atom. Increasing the power on the excitation laser will increase the rate of stimulated emission, which implies a decrease of the lifetime of this state resulting in an increase of the energy uncertainty. The same can be said for the ionization laser power. Increasing this also decreases the lifetime of the excited state. Therefore increasing the power of both lasers in a two-step excitation-ionization process, as in RIS, leads to a superposition of broadening mechanisms which will worsen the final spectral resolution of the resonance peak.

1.5 Multilevel Approach

From the relatively simple two-level atomic system interacting with a coherent excitation and incoherent ionization laser, the generalization towards multiple levels is made here.

1.5.1 Excitation

Extending the description of excitation from section 1.2 towards a two-level atomic system with a hyperfine substructure, boils down to a generalization of the previous. This multilevel model can for example exist of ground and excited state hyperfine multiplets. The off-diagonal elements in the Hamiltonian at position (i, j) will be interpreted here as the coupling of hyperfine level i with hyperfine level j, being non zero whenever state i is belonging to the ground state multiplet and state j to the excited state multiplet.

1.5.2 Ionization

The extension of the quantum mechanical description of the ionization process of section 1.3 towards a multilevel atomic scheme is found again in [1]. Here only the results will be stated. In contrast with the excitation step, the ionization step for a multilevel system is not just a standard generalization. Allowing more than 1 excited level to be coupled to the continuum leads to an internal coupling between these excited levels. Therefore population transfer is possible between the excited states, not due to direct coupling as is the case for the excitation step, but due to indirect coupling of every state to the continuum by the ionization laser. It is clear then that the presence of this ionization laser influences the obtained ionization spectra in a subtle way by distorting the quantum level structure.

1.5.3 Multilevel Excitation-Ionization Hamiltonian

As a conclusion to this section, the general Hamiltonian governing the dynamics of an excitation-ionization scheme on a ground and excited state multiplet is shown:

$$\left[\begin{array}{ccc||ccc} \omega_{i1} & \dots & 0 & g_{i1,f1} & g_{i1,f2} & \dots & g_{i1,fl} \\ \vdots & \ddots & \vdots & \vdots & \vdots & \ddots & \vdots \\ 0 & \dots & \omega_{ik} & g_{ik,f1} & g_{i1,f2} & \dots & g_{ik,fl} \\ \hline\hline g_{i1,f1} & \dots & g_{ik,f1} & \omega_{f1}-\omega_a-\frac{i}{2}\Gamma_{f1} & -\frac{1}{2}\Gamma_{f1f2}(q_{f1f2}+i) & \dots & -\frac{1}{2}\Gamma_{f1fl}(q_{f1fl}+i) \\ g_{i1,f2} & \dots & g_{ik,f2} & -\frac{1}{2}\Gamma_{f2f1}(q_{f2f1}+i) & \omega_{f2}-\omega_a-\frac{i}{2}\Gamma_{f2} & \dots & -\frac{1}{2}\Gamma_{f2fl}(q_{f2fl}+i) \\ \vdots & \ddots & \vdots & \vdots & \vdots & \ddots & \vdots \\ g_{i1,fl} & \dots & g_{ik,fl} & -\frac{1}{2}\Gamma_{flf1}(q_{flf1}+i) & -\frac{1}{2}\Gamma_{flf2}(q_{flf2}+i) & \dots & \omega_{fl}-\omega_a-\frac{i}{2}\Gamma_{fl} \end{array}\right]. \tag{1.9}$$

Matrix (1.9) presents the description of a two-step resonant excitation followed by a non-resonant ionization process, for two random hyperfine multiplets (i, f). 4 sub-blocks forming together the total Hamiltonian can be distinguished. The upper left block is the ground state multiplet with on the diagonal elements the energy of each hyperfine level $\omega_{i,j}$. The lower right block describes the excited state multiplet under the influence of ionization. On the diagonal are the excited state hyperfine energies with the excitation laser frequency subtracted. The imaginary term that is also subtracted from these energies describes the loss of excited state population due to non-resonant ionization. The non-diagonal terms in this block describe the coupling between the upper state hyperfine levels, due to their interaction with the continuum through the ionization laser (Γ in these terms depends on the ionization power density and non-resonant cross section, it will be considered the same for each es hyperfine level in the simulations). The Fano factor, q, is another remainder of the ionization coupling of the excited state levels. It is equal to:

$$q_{ab}(t) = \frac{\delta\omega_{ab}(t)}{\Gamma_{ab}(t)}, \tag{1.10}$$

with $\delta\omega$ and Γ coming from respectively (1.6) and (1.5). The upper right and lower left block contain the couplings induced by the excitation laser, between a hyperfine level from the ground state and a hyperfine level in the excited state. For simplicity, the $\delta\omega$ has been absorbed in the energies on the lower right sub-matrix. Once the Hamiltonian (1.9) is acquired, the Von Neumann equations contain all their parameters.

$$i\frac{d\rho}{dt} = H\rho - \rho H^{\dagger}. \tag{1.11}$$

Solving these equations to obtain the time and frequency dependent behavior of the populations of all states involved will be the main piece of coding for the simulations.
In a RIS experiment, the hyperfine splitting will most often lead to a multilevel system. Therefore, the final result will consist of a collection of resonance peaks corresponding to specific transition frequencies of this system.

1.6 Time Dependent Hamiltonian

So far, only time independent interactions between lasers and atoms were interpreted via the model. However when studying the effect of pulsed lasers in the model of (1.9), a new degree of freedom rises which bears great importance for optimizing a RIS experiment: the time delay between the laser pulses.
In normal practice the high power laser pulses are overlapped in time to maximize the ionization efficiency. However, as proven in [1], separating both laser pulses in time has a significant enhancing effects on the final resolution of a RIS experiment. The effect of this separation is two-fold, which will be discussed on the basis of the intuition built from the previous sections and the notion of adiabatic following.
First and foremost, the laser power of both excitation and ionization lasers broaden the resonance, as explained in section 1.4. Delaying the ionization laser cancels its power broadening effects on the excited state during the time the excitation laser is probing the hyperfine sublevels. On top of this, due to the adiabatic principle also the power broadening from the excitation laser is minimized, as will be explained in this section.
Secondly, the indirect coupling and energy shifting of the excited states from incoherent radiation by the ionization laser is delayed and the excitation step will therefore not feel its influence, again improving the overall accuracy and precision of the ionization spectrum. One will, in this way, distort the ensemble after the probing is already performed.
The sole reason of not delaying the second laser step, lies in a possible fast decay of the intermediate state. This will be discussed further on. To continue to clarify this statement a brief discussion follows regarding the adiabatic principle. This principle is employed to explain in a more intuitive way why this separation of pulses implies a better resolution on the excitation front. Also one example is considered where surprisingly this theoretical approach predicts for a certain kind of pulse shape, a power narrowing effect instead of power broadening. The adiabatic theorem will also be important for the second part of this thesis.

1.6.1 Adiabatic Theorem

To explain briefly the adiabatic theorem, its meaning is presented here in words because of its importance for the rest of this work. A deeper understanding and mathematical description of this theorem is found in [4]. When talking about the adiabatic theorem, a system governed by a time-dependent Hamiltonian is considered. If it is assumed that the system is in one of the eigenstates of the Hamiltonian at time $t = -\infty$ and if $H(t)$ is slowly varying in time, one can show that if the system started in an eigenstate of the Hamiltonian at the beginning of the interaction, it will follow the corresponding instantaneous eigenstate of the time-varying Hamiltonian, throughout the interaction.
In the case being studied here, this statement is extremely useful. Consider a laser pulse interacting coherently with a two-state system. If the pulse power is slowly varying as a function of time, the adiabatic theorem states that the population will remain in the instantaneous eigenstates of the interaction Hamiltonian. These states were encountered before in the first sections of this chapter and were then called adiabatic eigenstates. However if it is assumed that this Hamiltonian will never break the assumption of a slowly varying operator, one will end up again in the ground state of the system, being an eigenstate of the non-interacting Hamiltonian, after the laser pulse has passed. There would have been no population transfer to the higher lying multiplet possible. This is of course contradicted by what is seen in experiment. The error lies in the fact that when for small detunings and high laser power density, the total Hamiltonian can no longer be seen as slowly varying and the adiabatic theorem does not hold anymore. Disregarding the failure of the adiabatic principle in the case of efficient population transfer, the theorem still leads to important considerations. Pictures 1.1,1.2 and 1.3 will explain the implications of the adiabatic theorem for two-level coupling more thoroughly. Focusing on figure 1.3, two regions of population transfer in frequency space are distinguished. First of all, there exists the narrow region around the resonance frequency where non adiabatic evolution occurs. Secondly, during the presence of the excitation laser, transient population transfer is still possible outside the narrow non-adiabatic detuning range, see figure 1.2. Therefore, the lineshapes after ionization will strongly depend on the timing characteristics of this second laser.

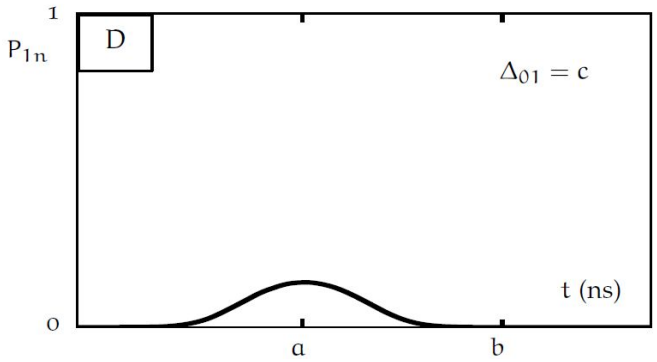

Figure 1.1: *The population of the excited state is depicted as a function of time at a certain detuning from resonance when interacting with a pulsed excitation laser. In this case the detuning is such that it causes almost perfect adiabatic evolution. The state vector will therefore follow one of the adiabatic eigenvectors to end up in the original eigenstate, the ground state of the Hamiltonian. [1].*

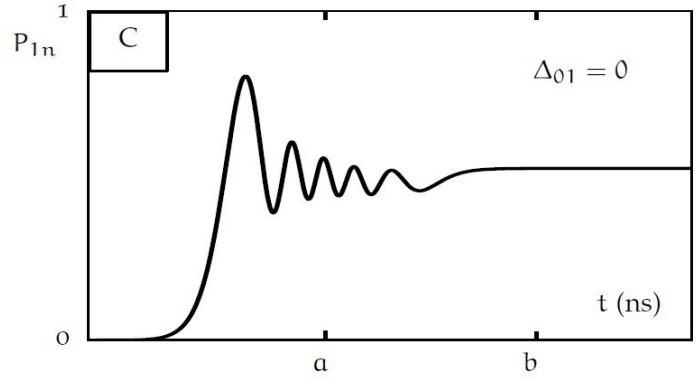

Figure 1.2: *The population of an excited state is depicted as a function of time at a certain detuning from resonance for a pulsed excitation laser. In this case non adiabatic evolution is evident, which can be seen from the non-zero population in the excited state, even when the laser pulse has already passed [1].*

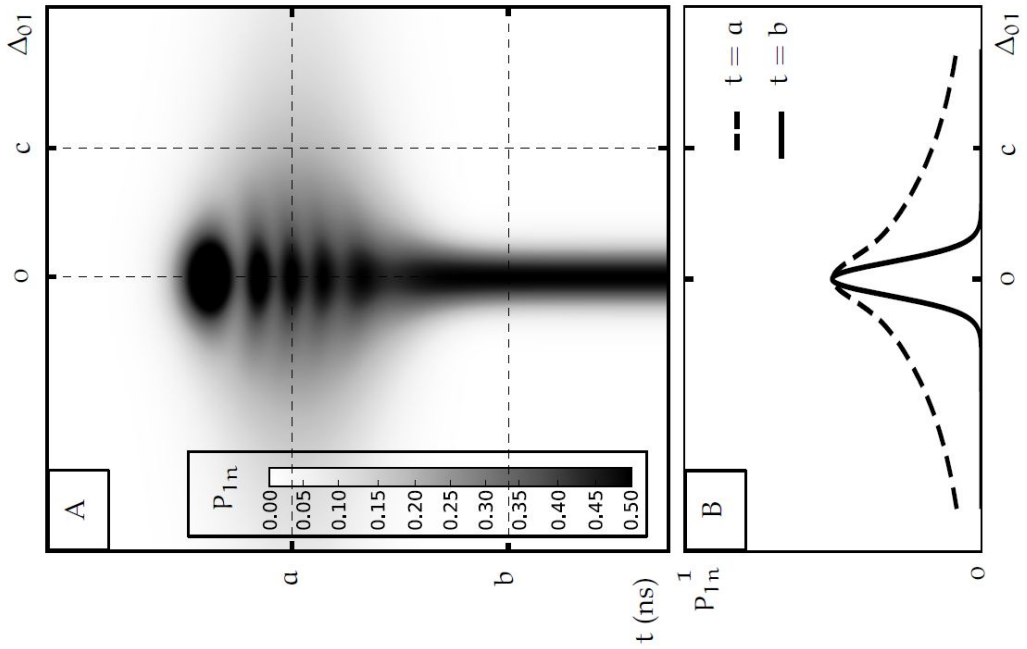

Figure 1.3: *left: Graphical representation of the excited state population as a function of detuning and time. One can obviously spot the detuning range for which non-adiabatic evolution occurs, as the efficient line around the resonance. Beyond this range, adiabatic following applies and only during the presence of the excitation pulse, some transient population transfer is visible. Right: Firing an ionization laser at time a will form a spectrum with much wider tails. Firing the ionization laser at time b will improve the resolution [1].*

Referring to [5], a more theoretical explanation is given concerning the non-adiabatic detuning range, founded by an example. Here the Hamiltonian, governing the process described in this report, is written in the adiabatic basis. Assuming the ionization laser is turned off or delayed in comparison to the excitation laser, following expression is obtained:

$$H = \begin{pmatrix} \lambda_- & -i\dot{\theta} \\ i\dot{\theta} & \lambda_+ \end{pmatrix}. \tag{1.12}$$

In this equation: $\tan(\theta(t)) = \frac{g(t)}{\Delta}$, with g the already used symbol for the coupling strength and Δ the symbol for the detuning of the excitation laser. One can see that even though the adiabatic states are supposed to be the instantaneous eigenstates of the Hamiltonian, the rate of change of the θ factor determines if they are in fact constants of motion. Already one can see that when this time derivative is large in magnitude, the adiabatic states are not perfect eigenstates of the instantaneous Hamiltonian and coupling between them can occur. Therefore intuitively, the condition for adiabatic evolution can be understood. For a rigorous mathematical expression of this condition, a reference is given to [4]. The conclusion is that for adiabatic evolution to occur, following condition has to be fulfilled:

$$|\langle a^+|\dot{a}^-\rangle| \ll |\lambda_+(t) - \lambda_-(t)|. \tag{1.13}$$

Here $|a^-\rangle$ and $|a^+\rangle$ represent the adiabatic states. From this, it is clear that the off-diagonal element, $\dot{\theta}$, should be small in comparison to the time dependent difference between the adiabatic energies. As long as this condition is fulfilled, no population transfer takes place. For this condition to make sense, also the instantaneous eigenvalues should be calculated. Here λ_-, λ_+ are the eigenvalues of the corresponding adiabatic states when there is no ionization. These are given by the expressions:

$$\lambda_\pm = \frac{1}{2}\left(\Delta \pm \sqrt{g^2(t) + \Delta^2}\right), \tag{1.14}$$

where Δ is the known detuning of the excitation laser and $g(t)$ is the coupling strength already encountered in (1.2). One can show now that the adiabatic evolution theorem is valid under the assumption that:

$$\begin{aligned} &|\dot{\theta}(t)| \ll \lambda_+(t) - \lambda_-(t) \\ &\Leftrightarrow |\Delta\dot{g}(t)| \ll 2\left(g^2(t) + \Delta^2\right)^{3/2} \\ &\Leftrightarrow f(t) \ll 1. \end{aligned} \tag{1.15}$$

Where $f(t)$ is trivially defined from the equation directly above. Again, hand wavingly, this condition can be translated as follows: when the off-diagonal terms of the Hamiltonian in the adiabatic base are large compared to the energy splitting of these adiabatic eigenvalues, adiabatic evolution will be hindered. Therefore, analyzing the dynamics of this two-state system governed by a time-dependent Hamiltonian requires knowledge on the detuning and the time evolution of the coupling strength and the eigenvalues. When at the same time eigenvalues approach and coupling terms are large, the adiabatic condition will fail. Differentiating the function $f(t)$ to detuning and equating this to zero brings the values of Δ ($\Delta = \frac{1}{\sqrt{2}}g(t)$) for which $f(t)$ is maximal ($|f(t)| = \frac{\dot{g}(t)}{3\sqrt{3}g^2(t)}$). This maximal value for $f(t)$ is now only dependent on the pulse shape (remember this is included in the definition of $g(t)$). It has become rather trivial to then calculate or estimate the detuning ranges for which the evolution of the populations is adiabatic and non-adiabatic. In the next section, two examples will be given for different pulse shapes.

1.6.2 Gaussian, Exponential and Lorentzian Laser Pulses

Looking at the expression for the maximum value of $f(t)$, it is clear that the values of $g(t)$ at early and late times are critical in determining the adiabaticity of the evolution if the peak value

of the pulse is centered around $t = 0$. At $t = 0$ the derivative will be 0 after all. Therefore 3 pulses will be considered [5]: a realistic Gaussian pulse, one that is vanishing exponentially and a Lorentzian one. Laser pulses are normally Gaussian shaped, for these kind of pulses, a detuning range in which non adiabatic evolution occurs is obtained (with T, the pulse time):

$$|\Delta| \sim \frac{\sqrt{\log(g/\Delta)}}{T}. \tag{1.16}$$

Therefore, by performing delayed laser ionization, the width of the resonance peak will increase logarithmically with laser power. In comparison, for cw irradiation, the power dependence of the resolution goes with the square root of laser power. If resolution is vital to the RIS experiment, it is therefore recommended to fire the ionization laser after the excitation laser in time to avoid the transient population transfer, outside detuning range (1.16), to contribute to the resonance peak.
For an exponentially vanishing pulse shape ($g(t) = g_0 sech(t/T)$), the derivative of $g(t)$ will be proportional to $g(t)$ itself. Replacing relevant terms in the definition of $f(t)_{max}$ (remembering that there is a connection between the detuning and $g(t)$ at this maximum value) brings:

$$|\Delta| T \gtrsim 1. \tag{1.17}$$

An interesting fact about this equation is the absence of the power of the laser. This means that for pulse shapes like this one, no power broadening will be seen. Only in a certain detuning range, independent of power, non-adiabatic evolution will be possible. A more striking example is found when considering Lorentzian pulse shapes. In this case following the same arguments as before, it can be shown that the detuning range where non adiabatic evolution is possible is inversely proportional to the laser power. This is therefore an example of power narrowing!

1.7 Experimental Considerations

Via previous sections, the general recipe for obtaining a model describing the laser-photon interactions for a two-step excitation-ionization procedure was obtained. Solving the Von Neumann equations of motion for density matrices in the case of non-hermitian Hamiltonians offers then the time and laser frequency dependence of the level populations. These level populations are then probed in laser spectroscopy experiments as a function of excitation laser frequency. There are however three extra considerations that have to be taken into account making the model more realistic and therefore more comparable to experiments: The broadened frequency spectrum of the laser photons, the spontaneous decay of the atomic levels and the laser intensity profile in space.
The actual addition of the laser linewidth and spontaneous decay to the recipe will be discussed in the next chapter. Now however, a small note can already be made regarding the laser linewidth. A simple convolution product between the obtained ionization spectra and the laser frequency profile could seem to incorporate this effect. However in this case one can not trust the amplitudes of the resulting spectra because each amplitude then results from a multiplication of the amplitude in the frequency spectrum with its corresponding spectral shape. The relation between an obtained spectrum and the laser frequency is however of a more complicated nature. A way of incorporating the laser linewidth, with some limitations, is explained the next chapter.

1.7.1 Spatial Average

The other experimental factor to be taken into account is the spatial laser profile. This should be included because of the fact that the laser beam intensity is not perfectly homogeneous over the volume but constitutes normally a 2D Gaussian-like intensity profile around the beam axis. Therefore the atoms, interacting with the beam off center, will interact with lower laser power than those interacting with the center of the laser beam. This problem is solved in the calculations by averaging the obtained spectra over a range of laser powers following a 2D Gaussian distribution. This would remove the well-known Rabi-oscillations from the picture as well as other distinct laser power characteristics. To be able to link simulations with experiments properly, this averaging procedure is also available in the code.

1.7.2 Approximations

The goal is to supply realistic simulations, therefore the exact input should be summarized. **To end this section, it must be stated that not all factors included in the total Hamiltonian of this process are considered in the simulations.** The **Fano factor** can be included but is most of the time taken to be approximately zero. Next, **the couplings between states of the excited multiplet induced by the ionization laser are all taken to be of the same magnitude.** Finally another important factor is **neglected at first**, **these are the so called ac-Stark shifts which are the energy shifting terms on the diagonal for the levels of the excited multiplet**. Their importance will be stated in one of the next sections, supported by experimental data.

Chapter 2

Theoretical Additions

As introduced in 1.7, some improvements and additions to the existing model of [1], as an attempt to make it more closely resembling nature, are possible. These will be discussed in this chapter before their influence on the RIS experimental parameters is discussed in the next.

2.1 Introduction

As an extension to the work of [1], this report will provide an update to the theoretical basis and simulation code. This extension consists of adding spontaneous decay and laser linewidth to the model discussed in the previous chapter. In addition to this, a new simulation code was written allowing any number of excitation steps to be studied.

2.2 Spontaneous Decay

The atomic levels, on which the focus was in chapter 1, can all decay via photon emission to the ground state. These photons have an exactly defined energy but they can be emitted in any direction if the ensemble has a randomly oriented atomic spin (which is the normal situation). To include this in the model, one has to go beyond the Schrödinger picture because of the infinite degrees of freedom the new system would possess. For the addition of this spontaneous decay to the Von Neumann equations of motion, concerning the density matrix approach, the reader is referred to [4]. To include the effect of relaxation, one considers the atom to couple to a reservoir that is initially in the vacuum state. The atom can then emit photons into this vacuum state. In the density matrix approach, one is capable of tracing out this reservoir making calculations possible only regarding the actual atomic system of interest. In [4], it is stated that the spontaneous decay or relaxation of the states can therefore be incorporated in the formalism developed before and mathematically written as (1.11), by adding the Lindblad super operator Λ. This operator is derived from a system-environment interaction and ensures that the evolution of the density matrix is completely positive. Following theoretical models, as for example presented in [6] or [7], one can eventually find this evolution. The generator can then be included in the Von Neumann equations, governing the dynamics of the density matrix ρ. These will become:

$$i\frac{d\rho}{dt} = H\rho - \rho H^{\dagger} - \Lambda\rho. \tag{2.1}$$

However the question remains, how this operator looks and if it can be added to the simulation code. Simplifying matters by looking at the matrix elements separately gives:

$$i\frac{d\rho_{ij}}{dt} = H_{ik}\rho_{kj} - \rho_{ik}H^{\dagger}_{kj} - \Lambda_{ijkl}\rho_{kl}. \tag{2.2}$$

Here the Einstein summation convention is assumed. For the diagonal terms of the density operator matrix ρ_{ii}, the elements of Λ are given by:

$$\begin{aligned}\Lambda_{iinm} &= -\lambda_{in}\delta_{nm}, \text{ for } i < n \\ &= \sum_{k<i}\lambda_{ki}\delta_{nm}, \text{ for } i = n \\ &= 0, \text{ for } i > n.\end{aligned} \tag{2.3}$$

In this equation, λ_{in} is interpreted as the decay rate of state n to state i. For the off-diagonal terms in the density matrix, one must use for Λ:

$$\Lambda_{ijnm} = \frac{1}{2}\left(\sum_{k<i}\lambda_{ki} + \sum_{k<j}\lambda_{kj}\right)\delta_{in}\delta_{jm}. \tag{2.4}$$

The form of these equations alongside knowledge of the decay terms λ, makes it possible to include the effect of spontaneous emission in the simulations as well.
The influence of this spontaneous decay operator on the dynamics is two-fold. First of all, the diagonal elements result in the exponential decay or relaxation of the excited state population as classically expected. In addition to this, non-classical off-diagonal elements are present in this Lindblad operator. These terms include the decoherence effect resulting from the spontaneous decay process. In crude terms, these off-diagonal elements will damp Rabi oscillations, which are a proof of coherence between two states. The spontaneous decay process will thus result in a steady state excited state population.
Important to note here is that until stated otherwise, the simulations will be done with the assumption that the decay of the excited state only populates the ground state. Addition of decay to quantum levels outside the system is possible with more imaginary factors on the Hamiltonian's diagonal.
The only parameter left to determine is the decay rate from level j to level i, λ_{ij}. Because decay rate and coupling strength are related, the two parameters will receive a reconstructed definition as function of the Einstein A parameter, highlighting their resemblance. This Einstein A parameter represents the decay rate from one finestructure level to another and is related to the oscillator strength from (1.2). The formula to describe the coupling strength between two levels of a hyperfine multiplet (F' to F) is according to [8] and similarly [9] (the coupling term g is replaced by the more common Ω in future calculations):

$$\begin{aligned}\Omega(F,F') &= (-1)^{1+2F+I+J'+S+L'+J} \\ &\quad * \sqrt{(2F+1)(2F'+1)(2J+1)(2J'+1)(2L+1)} \\ &\quad * \sqrt{\frac{3\lambda^3 AI}{4\pi^2 c\hbar}} \\ &\quad * \begin{Bmatrix} J & F & I \\ F' & J' & 1 \end{Bmatrix}\begin{Bmatrix} L & J & S \\ J' & L' & 1 \end{Bmatrix}.\end{aligned} \tag{2.5}$$

I, L, S, J, F representing the common quantum numbers with the primed ones being associated with the ground state. λ is the transition wavelength, I the laser intensity and A the decay rate (= Einstein A parameter). A similar formula describing the decay rate between states of a hyperfine multiplet that will be used in the simulation code is found in [10]:

$$\gamma(F,F') = |\langle L||r||L'\rangle|^2 \frac{4\alpha_{HFS}}{3}(2F'+1)(2J+1)(2J'+1)\frac{\omega^3}{c^2} * \left\{ \begin{array}{ccc} J & 1 & J' \\ F' & I & H' \end{array} \right\} \left\{ \begin{array}{ccc} L & 1 & L' \\ J' & S & J \end{array} \right\}. \tag{2.6}$$

Here similar symbols are used with the addition of the hyperfine parameter α_{HFS} and the energy difference between the levels ω. There is however an unknown matrix element $|\langle L||r||L'\rangle|$ remaining in (2.6), which should normally be calculated theoretically. This calculation can be circumvented when the total decay rate from a finestructure level is known experimentally. From theory one can obtain that a level corresponding to one of the hyperfine sublevels of this fine structure state should have exactly the same decay rate when all partial decay rates are summed over all hyperfine levels to which the decay is aimed. Using this prediction, one can cancel the unknown factor $|\langle L||r||L'\rangle|$.

Deriving previous expressions is a cumbersome but nevertheless illuminating task involving complex angular momentum relations, therefore a brief overview of the derivation of the Rabi frequency is presented. The Rabi frequency is defined as $\Omega = \frac{-\vec{d}\cdot\vec{E}}{\hbar}$. Instead of evaluating the scalar product in the common x, y, z base, the spherical base is chosen because of its superior symmetry characteristics. Assuming the laser beam is linearly polarized, one can fix the z-axis of the spherical base on the axis of the photon's electric field. Working this out, the matrix element or Rabi frequency for a transition between two hyperfine levels is written down as follows:

$$\Omega_q = (-1)^{(1/2)q(1+q)+1}\sqrt{\frac{2I}{\epsilon_0 c\hbar^2}}\langle n, F, m_F|D_q|n', F', m'_F\rangle. \tag{2.7}$$

In the case of linearly polarized light, the q can be taken equal to zero while n is an extra quantum number often necessary to describe the system such as the principal quantum number in the hydrogen atom system. The expression under the root is a representation of the electric field amplitude as a function of the intensity of the laser beam. Using the Wigner-Eckart theorem, the dependence on the m_F, m'_F factors of the matrix element can be contained in a Wigner 3J symbol. This is a translation of the fact that the orientation of the spin with respect to the electric field vector is not fundamental but mere a geometrical calculation. To keep track of the intermediate steps in the derivation:

$$\Omega \sim (-1)^{F-m_F}\langle n, F\|D_0\|n', F'\rangle \begin{pmatrix} F & 1 & F' \\ -m_F & 0 & m'_F \end{pmatrix}. \tag{2.8}$$

The next step is related to the fact that in the dipole approximation, the laser photon only interacts with the orbital-angular momentum L of the electron. Therefore two Wigner 6J symbols are needed. The first to return to the uncoupled I, J representation of the system. Next, another 6J symbol is required to take another step back and represent the matrix element in the elemental I, L, S basis. After all the dust has settled on these cumbersome calculations, the Rabi frequency has been reduced to a multiplication of several geometrical

Wigner expressions with a fundamental matrix element. This fundamental matrix element can be written as:

$$\langle n, L \| D_0 \| n', L' \rangle. \tag{2.9}$$

The matrix element given in (2.9) can be further reduced to a product between a radial integral and some more geometrical factors. This radial integral is many ways similar to the matrix element obtained in (2.6) and describes the interaction between the atom's dipole moment from the electron in the wave function with the electric field of the incoming photon. Via the assumed knowledge on the Einstein A parameter, this radial integral can be obtained without the need for theoretical input. Putting all pieces of the puzzle together, (2.8) is transformed into the initial equation (2.5). The presence of the decay rate in this expression is related to the radial integral as stated before.

2.3 Laser Linewidth

The lasers used in experiments to excite the atomic ensemble never consist of single frequency photons, but instead have a limited bandwidth. Following a discussion in [11] and [12] one can view the consequences of adding the finite laser linewidth as an increase of the dephasing rate of the off-diagonal coherences of the density matrix while leaving the diagonal terms completely unchanged. As before, for the spontaneous decay term, this can also be expressed in another Lindblad operator, defined by:

$$L_{ijkl} = \delta_{ik}\delta_{jl}\gamma_e, \text{ for } i \neq j. \tag{2.10}$$

The γ_e term represents the HWHM of the laser linewidth. This Lindblad operator should then be added to the Von Neumann equations of motion as before in (2.2). This is exactly what is done for the simulations.

$$i\frac{d\rho}{dt} = H\rho - \rho H^\dagger - \Lambda\rho + L\rho. \tag{2.11}$$

An important side note should be made regarding this procedure. The addition of this extra Lindblad term to the Von Neumann equation of motion boils down to a convolution of the ionization spectrum obtained for a single frequency with the Lorentzian frequency spectrum of the laser, see [12]. Therefore it is not derived from first principles. Employing this method was discouraged in section 1.7. However it is legitimized in certain conditions. First of all, the half laser linewidth should be comparable or smaller than the Einstein A parameter. Both A parameters and conventional laser bandwidths situate in the MHz-GHz range. This condition is therefore realistic but it should be handled with caution. In addition to this, the difference in energy between the coupled levels should remain far greater than the laser line width. This condition is normally met in laser spectroscopy applications. When both conditions are satisfied, the Lindblad term can safely be added to the equations of motion of the system.

To give an example of the Lindblad operators (2.3),(2.4) and (2.10) for a two state system, where ground state and excited state are coupled by a realistic laser:

$$i\frac{d\rho}{dt} = H\rho - \rho H^\dagger + \begin{pmatrix} \gamma\rho_{22} & -\frac{\gamma\rho_{1,2}}{2} \\ -\frac{\gamma\rho_{2,1}}{2} & -\gamma\rho_{22} \end{pmatrix} + \begin{pmatrix} 0 & -\gamma_e\rho_{1,2} \\ -\gamma_e\rho_{2,1} & 0 \end{pmatrix}. \tag{2.12}$$

2.4 Extra Considerations

2.4.1 Ac-Stark Shifts

The ac-Stark shift was already mentioned in 1.3 as being a possible energy shift for the levels incoherently irradiated by an ionization laser. Figure 2.1 found in [13] is a potential example of how experimentally obtained spectra can be influenced by this phenomenon. This ionization spectrum was obtained via resonant excitation of the $7s^2S_{1/2} - 8p^2P_{3/2}$ levels in ^{221}Fr in a CRIS experiment (a more detailed discussion on the experiment itself will be given in chapter 4).

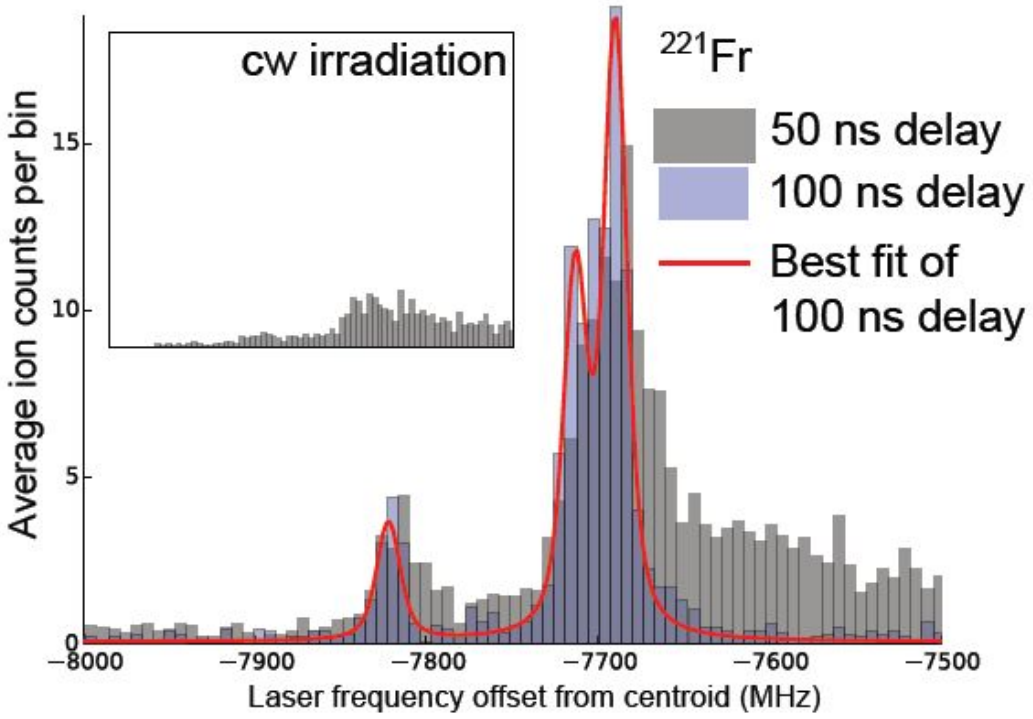

Figure 2.1: *Resonance ionization spectrum of ^{221}Fr obtained with a chopped cw beam of 100ns length. The ionization and excitation were separated by 50ns (partial overlap) in the gray plot and 100ns (complete separation) in the blue one. Interesting is the tail structure of the resonance peak on the right of the 50ns plot, [13]. The details of the experiment can be found in chapters 4 and appendix B.*

To explain the tail structure in 2.1, assume a much simplified example of a two-level scheme $|0\rangle, |1\rangle$ coupled to each other by an excitation laser and to the continuum (only $|1\rangle$) via an ionization laser. Concerning the Stark shift, this description is equivalent to a multilevel scheme. For completely separated lasers in time, the excitation laser scans the unperturbed states and therefore will return the spectrum as expected without the tail. Now consider two Gaussian laser pulses that overlap in time. As long as the excitation pulse is interacting with the atom without the presence of the ionization laser, similar dynamics as in the case of separated laser pulses are expected. As the ionization laser starts to interact however, it will perturb the states that the excitation laser is probing. Assume now this Stark shift induces a positive shift in the energy of the excited state. Then the excitation laser will probe the increasing energy value

of the excited level.
This picture could explain the broad continuum next to the resonance structure in the spectrum of figure 2.1 with the left or right appearance of the tail dependent on the sign of the perturbation to the energy. Adding this ac-Stark shift to the simulations will be non-trivial because of the theoretical problems one faces in calculating these shifts. Therefore in the simulations shown later in this report, when mentioned, the Stark shifts are added as diagonal terms in the Hamiltonian proportional to the ionization laser power according to [14]. This implementation is allowed via the derivation of the Stark shift in section 1.3, where it represents a shift in the energy of the excited state. The factor determining this proportionality is not known and is chosen such that it fits the data in a satisfactory manner.
An extra argument in favor of the Stark shift being the cause of the elongated resonance tail is found in the inset of figure 2.1. The inset shows exactly the same spectrum obtained by continuous wave laser excitation. In this case only the elongated tail is visible because optical pumping removes all other resonant behavior. During the presence of the ionization laser however, non-resonant irradiation can become resonant causing the tail to appear.

2.4.2 Multi-Step Simulations

For many years, multiple laser step schemes have been developed to obtain nuclear information otherwise non achievable for two-step schemes. Because of this, instead of the two-step process theoretically covered in previous sections, multi-step excitation-ionization procedures were allowed in the simulation code. Obviously some adaptations must be made to the existing code and its additions, before also these experiments can be simulated. Luckily the extension to the Hamiltonian and Lindblad operators which are governing the process is rather trivial. For example, instead of dealing with a two-block matrix in the Hamiltonian, adding another excitation step will require a third block to be added, 1 block for the ground state and two blocks for the two excited hyperfine multiplets. This extra middle block should then be coupled to the ground state by the first excitation laser and to the second excited multiplet by the last excitation laser. Because of this block structure of the Hamiltonian, an object oriented code was written in python which can handle any number of excitation steps for an arbitrary number of states and simulate the expected outcome.

2.5 Summary

To conclude this brief overview of the theoretical description one faces when dealing with atom-photon interactions encountered in a RIS experiment, a short summary of possible lineshape effects that are induced by the characteristics of these interactions is given.
At first, when the temporal shape of the lasers is close to Gaussian, power broadening has a big influence on the precision of the spectra. However as was theoretically shown, if one could alter laser pulse shape, also power narrowing would in principle be possible. Furthermore, the timing of the ionization laser with respect to the excitation laser has an import influence on the degree of broadening.
Next, two other effects, related to the presence of the ionization laser, influence the experimental spectral lineshape. The indirect coupling of the excited states to each other via the ionization laser, coupling them all to the continuum, could lead to a subtle change in the obtained spectrum, reducing the accuracy. Finally the ionization laser also shifts each excited

state energy level with a certain amount (ac-Stark shift). All of these effects can lead to asymmetric lineshapes as well as significantly alter the ionization spectra. This could lead to misinterpretation of the experimental data.
The summary given here applies to simultaneous excitation and ionization. Completely separating both in time, could have a drastically improving effect on the obtained data. Power broadening and level shifting effects of the ionization laser are drastically reduced which could improve the resolution significantly as is the conclusion in [1]. The only disadvantage of this technique, is the possible loss in efficiency for rapidly decaying excited states.

Part II

Simulations

Chapter 3

Simulations

This chapter deals with the study of the model described in chapter 1 with the additions discussed in chapter 2, via the use of a simulation code. The main focus of this study lies in the possible optimization steps in the laser-atom interaction part of a RIS experiment. To understand, interpret and employ the results that the simulations offer, an analytic model for the complete description of a two-level quantum system is used.

3.1 Introduction

The following sections will all come to a similar conclusion, namely that laser spectroscopy using transitions with small Einstein A parameters ($A_< = A \leq 10^6$ s^{-1} = weak) could prove beneficial in a number of ways compared to strong transitions ($A_> = A \geq 10^8$ s^{-1} = strong). As will be argued based on simulation results, the advantages of using $A_<$ transitions are five-fold. First of all, $A_<$ transitions have inherently smaller linewidth. Second and third, laser power broadening and line distortion effects can be minimized by delaying excitation and ionization laser pulses in time with respect to each other, the outcome of chapter 1, without losing efficiency due to spontaneous decay. Next, the ionization efficiency in ionization laser spectroscopy experiments can be optimized for $A_<$ transitions by adjusting the excitation laser pulse length. Finally, it seems that $A_<$ transitions are more easily saturated. Following these arguments, weak transitions could offer improvements to the experimental parameters such as precision, accuracy and efficiency. Each of these five potential advantages will be considered and examined in the following sections after describing first the structure of the simulation code.

3.2 Simulation Input

A short overview of the simulation code is presented here.

- Via a graphical user interface, the input parameters are easily changed and the output file can be chosen. The input parameters are then attached as meta-data to the output data file such that they can be revisited at any time. The graphical user interface and a pictorial drawing of the effect of the input parameters for a simple system consisting of an arbitrary two fine structure levels, is given in figure 3.1.

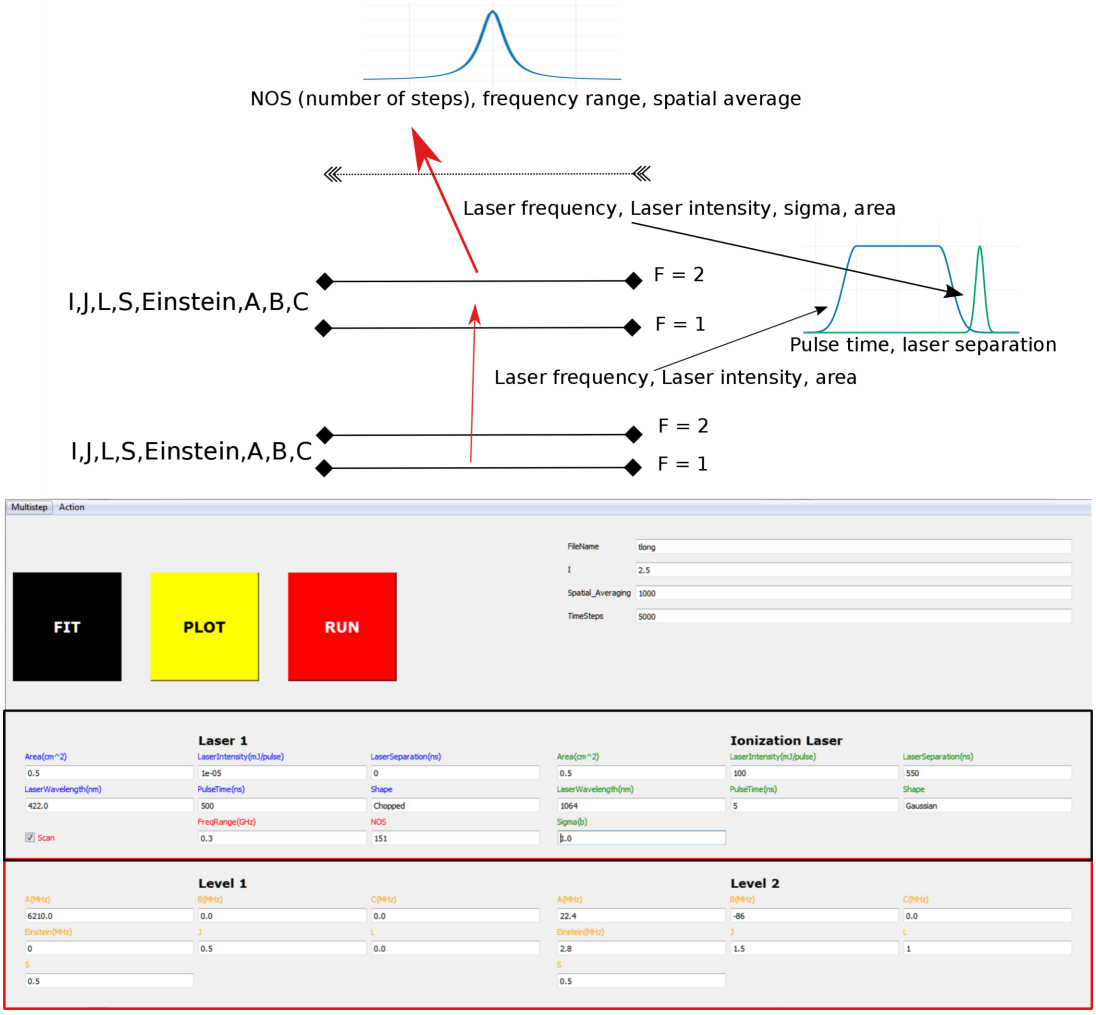

Figure 3.1: *Graphical User Interface employed to simulate RIS-spectra with a brief explanation of the influence of all input parameters. The amount of lasers steps can easily be changed.*

- Using the input parameters, the hyperfine level energies and transition intensities are calculated together with the extra couplings discussed in the theory chapters. These numbers are put into the Hamiltonian which is calculated for each frequency and time step. At the end, the Hamiltonian, presented in (1.9), is obtained without the time dependent terms of the laser pulses

- To complete the Von Neumann equation, the extra Lindblad term is calculated for each frequency and time step. This Lindblad operator configures the spontaneous decay and laser linewidth dependence, shown in (2.3), (2.4) and (2.12).

- The simulations are then started by choosing a number of excitation steps. For each frequency step of the scanned laser, the equations of motion are solved where for each time step the power dependent terms are multiplied with a time dependent factor representing the laser pulse shape. Unless explicitly stated otherwise, the excitation pulse shape will be shaped as in figure 3.1 (blue, flat top pulse with Gaussian edges). In this way, **separated pulses** are easily defined as shown in this figure while **overlapping pulses** are similar with the ionization pulse (green, Gaussian) fired in the center of the

excitation pulse. The full Von Neumann equation to be solved was presented in (2.11).

$$i\frac{d\rho}{dt} = H\rho - \rho H^\dagger - \Lambda\rho + L\rho.$$

- To show the ionization spectrum as a function of frequency or the populations of the quantum states as a function of time, the graphical user interface (GUI) presents a PLOT button. When analyzing the spectra is essential, a full χ-squared fitting routine, available via the FIT button on the GUI, is present (with the help of the SATLAS-package, [15]).
- **Important notes:**First, because of the close relation between angular frequency and photon energy $E = \hbar\omega$, the simulation code is written as a function of ω. All quoted frequencies in the following sections and chapters are therefore to be divided by 2π to obtain the result in regular frequency space. If normal frequency is used it will be clearly stated in the figure. In addition to this, the simulation code expects the laser intensity as an input given in energy per pulse and per unit of surface. Therefore figures and discussions dealing with laser intensity consequences will often quote the laser intensity as being of units J/m^2, per pulse.

3.3 $A_<$'s Linewidth

Transitions with a small Einstein A parameter posses an inherently small linewidth when studied in a RIS experiment. Probing these transitions will therefore improve the precision.
First of all, the diabatic range for Gaussian shaped laser pulses, which determines the resolution due to power broadening effects, is important. This range of frequencies defines the area in frequency space where efficient excitation can be done, see section 1.6. The diabatic detuning range is proportional to the coupling between the quantum levels, which is in turn dependent on laser intensity and Einstein A parameter:

$$\Omega \sim \sqrt{AI}. \tag{3.1}$$

With I the laser intensity. From (3.1), using $A_<$ transitions is equivalent to lowering the excitation laser intensity. Therefore $A_<$ transitions offer inherently smaller diabatic detuning ranges and by consequence smaller linewidths in ionization experiments. An experimental example of this smaller inherent linewidth can be found in section 4.2.
In addition to this, due to Heisenberg's uncertainty principle, all transitions possess an inherent linewidth even when very low laser intensity is used to reduce all power broadening effects. This effect contributes to the Lorentzian part of the final Voigt resonance profile as follows:

$$FWHM_{Lorentzian} = A. \tag{3.2}$$

Therefore, weak transitions offer, according to Heisenberg, a smaller uncertainty on their energy and thus a smaller linewidth when probed by laser spectroscopy. An example of this lifetime narrowing is shown in figure 3.2.
This inherent advantage of an $A_<$ transition presents the first argument in favor of using these kinds of transitions in laser spectroscopy experiments when high resolution is required.

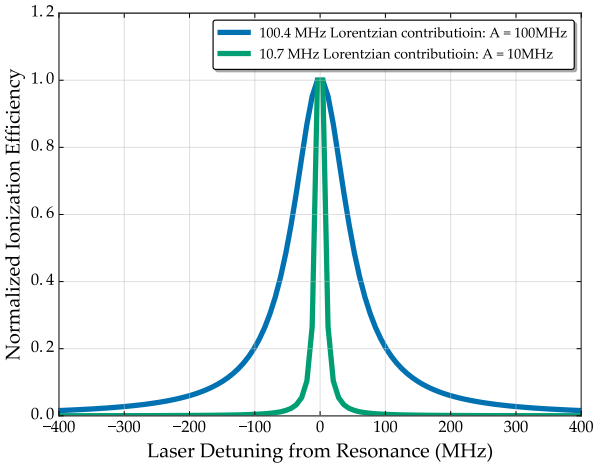

Figure 3.2: *Ionization spectra obtained with two different transitions. The first transition has a spontaneous decay rate of 100MHz while the other decays with a rate of 10 MHz. The influence of the natural linewidth on the Lorentzian contribution of the resonance profile is clearly visible, as predicted by* (3.2)*. The laser powers were intentionally low to reduce the power broadening effect.*

3.4 $A_<$'s Decay Rate

This section will deal with the influence of the slow spontaneous decay rate of weak transitions on ionization spectra. In addition to the lack of efficiency loss when delaying the laser pulses for $A_<$ transitions, also the optimization procedure to maximize this ionization efficiency will come from the spontaneous emission term in the Von Neumann equation. The analytical model used to interpret and place the simulation results in an experimental background is well known, with two clear discussions found in [6] and [7].

3.4.1 Delayed Ionization

As a clarification of the theoretical concepts explained in section 1.6 of chapter 1, a simulation considering the population transfer in a hypothetical excitation experiment will be discussed. For this case a simple two-level scheme $|0\rangle, |1\rangle$ is used.
Figure 3.3 shows the population of the excited state after being irradiated by a laser as a function of time as well as a function of laser frequency. The considerations made in section 1.6 of chapter 1 considering the Rabi oscillations and adiabatic broadening of the spectral line are again visualized. However, in this case, the decay of the excited level is taken into account, which was not done in [1]. This decay renders itself visible in the decreasing population of the excited state as a function of time after the excitation pulse has passed.
Figure 3.3 again clearly shows what the advantages and disadvantages are of laser separation when also ionization is taken into account. Firing the ionization laser in the smeared out region of the population surface, at the same time as the excitation laser, will as mentioned before reduce the experimental resolution and create possible accuracy losses or line distortions. Delaying the ionization laser with respect to the excitation laser will improve this resolution but at the cost of a lower efficiency because of the decay back to the ground state. An equilibrium between efficiency, resolution and line distortions should therefore be found.
The loss of efficiency will be minimized for $A_<$ transitions because of their slow decay rate.

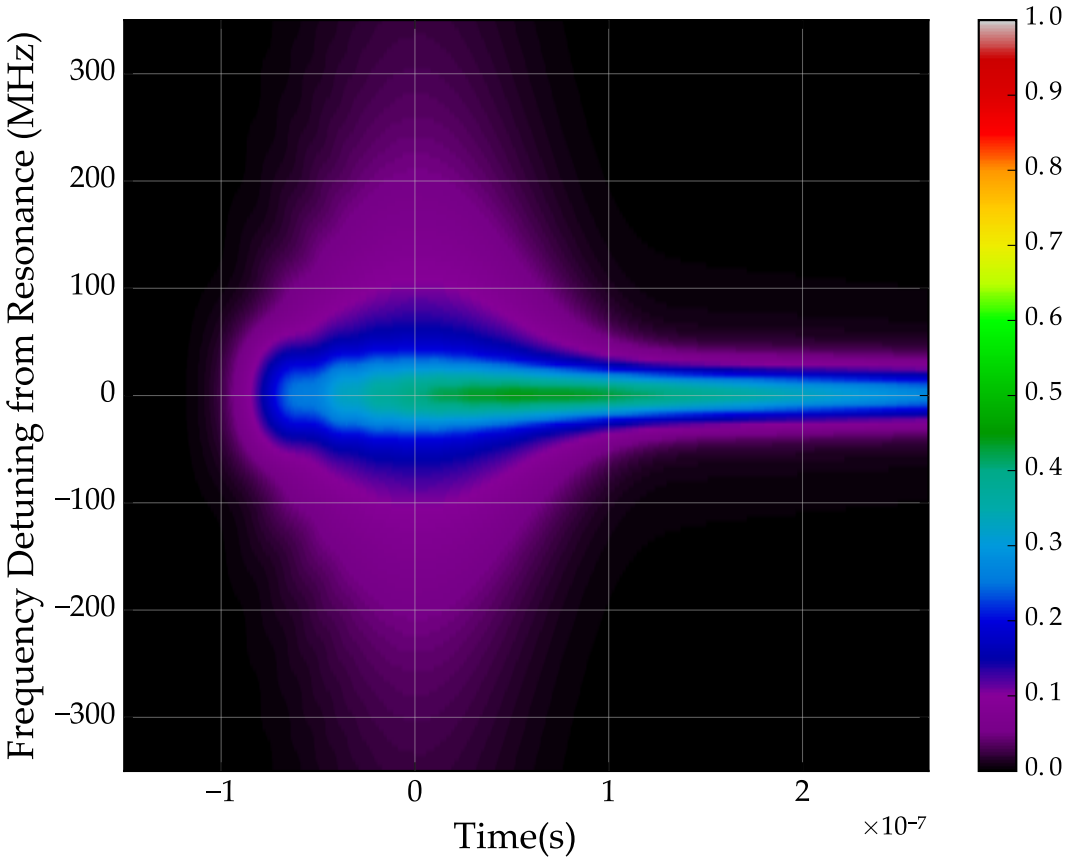

Figure 3.3: *Similar plot as figure 1.3, showing the increasing population of the excited level due to laser driven coherent coupling, as a function of time and detuning. Via the inclusion of spontaneous decay, up and downsides of delaying laser pulses can be seen as respectively the smaller linewidth at later times and the increasing population loss because of spontaneous emission. The excitation laser intensity drops to zero at time = 100ns.*

This means that the entire argumentation from [1] can be extended in the case of weak transitions. Probing these transitions by delayed ionization will therefore increase the precision by decreasing the power broadening and improve the accuracy and lineshape by canceling the distorting nature of the ionization laser. Via the addition of spontaneous decay, simulations can be done to estimate the potential efficiency loss to be expected with delayed ionization in future experiments.

Alongside the possibility to use delayed ionization to probe weak transitions in RIS experiments, their slow decay rate brings another advantage on the efficiency front. To understand this effect, a simple model describing a coherently coupled two-level scheme with the inclusion of spontaneous decay is presented in the following section. The influence of the pulse length will proof to be key to further efficiency optimization.

3.4.2 Population Transfer

An important feature of adding the spontaneous decay term to the Von Neumann equation has been touched upon briefly in section 2.2. As discussed in 1.2, cw-irradiation of a two-level

quantum system automatically leads to Rabi-oscillations in which the population oscillates between ground- and excited level. When the spontaneous decay term is added to the Von Neumann equations of motion, however, remaining Rabi oscillations are still present for small decay lifetimes but in general they grow towards an equilibrium population density in the excited state. Considering this in further detail, the reader is referred to chapter 4 of [7]. In this chapter, a clear system of differential equations is obtained, which describes the interaction of a two-level quantum system, coupled to an environment (spontaneous decay), with a coherent light source given by the Jaynes-Cummings model (only excitation). These equations are as follows [7]:

$$\begin{aligned} \frac{dX(t)}{dt} &= -\Delta Y - \gamma X, \\ \frac{dY(t)}{dt} &= \Delta X + \Omega Z - \gamma Y, \\ \frac{dZ(t)}{dt} &= -\Omega Y - A\left(Z + \frac{1}{2}\right). \end{aligned} \tag{3.3}$$

The variables Δ, Ω are respectively the detuning from transition resonance and the coupling strength induced by the coherent light source. A is in this case the decay rate, while $\gamma = \frac{A}{2} + \lambda$. This new kind of decay strength takes into account other dephasing mechanisms such as collisions, which are assumed to not change the populations but to affect the coherences. Disregarding the collisions, implies one can opt for $\gamma \approx \frac{A}{2}$. The system of differential equations (3.3) has been obtained via the Von Neumann equations of motion. The matrix elements of the density matrix have been rewritten in terms of X, Y, Z which are give by the following definitions:

$$\begin{aligned} (X(t) + iY(t))\,\mathsf{exp}(i\Omega t) &= \rho_{1,2}(t), \\ Z(t) &= -\frac{\rho_{2,2}(t) + \rho_{1,1}(t)}{2}. \end{aligned} \tag{3.4}$$

The reason why these matrix elements were written down in the form defined by (3.4) is for a reason. Writing the density matrix at any given time as follows:

$$\rho = \begin{pmatrix} \frac{1}{2} + Z & X - iY \\ X + iY & \frac{1}{2} - Z \end{pmatrix}, \tag{3.5}$$

it becomes clear that $\vec{a} = (X, Y, Z)$ is the Bloch vector, characterizing the density matrix completely and representing it by a point inside or on the Bloch sphere. This Bloch sphere is the unit sphere in three dimensions. For a two level system, a general density matrix can be written as follows:

$$\rho = \flat + \vec{a}\vec{\sigma}, \tag{3.6}$$

where $\vec{a}$ is the Bloch vector ($|\vec{a}| \leq 1$), $\vec{\sigma}$ the Pauli matrices and $\flat$ the unit matrix in two dimensions. Therefore, any two-dimensional density matrix can be completely determined by a point within the unit sphere. Density matrices describing pure states will lie on the Bloch sphere while mixed states are described by a point within the Bloch sphere.

Following this initial interpretation, the differential equations (3.3) are intuitively more understandable. As (X, Y, Z) represent respectively the x,y,z-projection of the Bloch-vector, according to (3.3), Δ, Ω, A represent respectively a rotation about the z-axis which shows the phase revolution, a rotation around the x-axis, explaining excitation and the shortening of the z-component of the Bloch-vector by spontaneous decay. For a maximum excitation efficiency the coupling should rotate the Bloch-vector from its initial condition, the negative part of the z-axis or fully populated ground state, towards the positive part, a π-rotation. The angular rate is represented by Ω, thus in this case $\Omega t \sim \pi$. Therefore, $A_<$ transitions will possess inherently slower rotation rates because of the A-dependence in Ω but the length of the Bloch-vector will have decreased less than for $A_>$ transitions. This geometrical intuitive picture of a rotating vector helps in understanding the influence of all parameters on the quantum dynamics of the system.
Returning to (3.3), equating all time derivatives in (3.3) tot zero,[6] obtains the steady-state excited level population:

$$\begin{aligned} P_{exc} &= \frac{\Omega^2}{2A\gamma} \frac{1}{1 + \frac{\Delta^2}{\gamma^2} + \frac{\Omega^2}{\gamma A}}, \\ &= \frac{\Omega^2}{A^2 + 4\Delta^2 + 2\Omega^2}, \end{aligned} \tag{3.7}$$

where the second equality sign is obtained by putting $\gamma = A/2$. The situation where only relaxation and dephasing due to spontaneous decay is included and other dephasing mechanisms, such as collisions, are assumed small, will be prolonged for the remainder of the discussion. Referring back to equation 2.5, it can be noticed that, only regarding the dependence on the Einstein parameter, $\Omega \sim \sqrt{A}$. Therefore, the eventual steady-state population depends on A in a first approximation as:

$$P_{exc} \sim \frac{1}{2 + A}. \tag{3.8}$$

Incorporating the laser intensity dependence of Ω, one obtains:

$$P_{exc} \sim \frac{1}{2 + \frac{A}{I}}. \tag{3.9}$$

The expression (3.8) hints towards a bigger steady-state excited level population for small decay rates. However, as can be obtained via (3.3), the time it takes the system to reach this equilibrium excited state population is inversely proportional to A, as already interpreted via the Bloch-vector. (3.9) shows the intimate relation between the intensity and Einstein A parameter. For maximum steady state population the factor A/I should be as small as possible. Increasing the intensity has therefore the same effect as decreasing the transition strength. However, for weaker transitions, the interaction time should be larger to allow the excited state to attain the steady-state population.
The preceding statements can be illustrated as follows. The original solutions of the Von Neumann equations without ionization constitutes a simulation for two different pulse lengths and two different A-parameter transitions. The excited population with the coherent laser on resonance ($\omega_a - \omega = 0$, when ω is one of the resonance frequencies and ω_a the laser frequency) is plotted as function of time in figure 3.4. In the top part of figure 3.4 the pulse length is

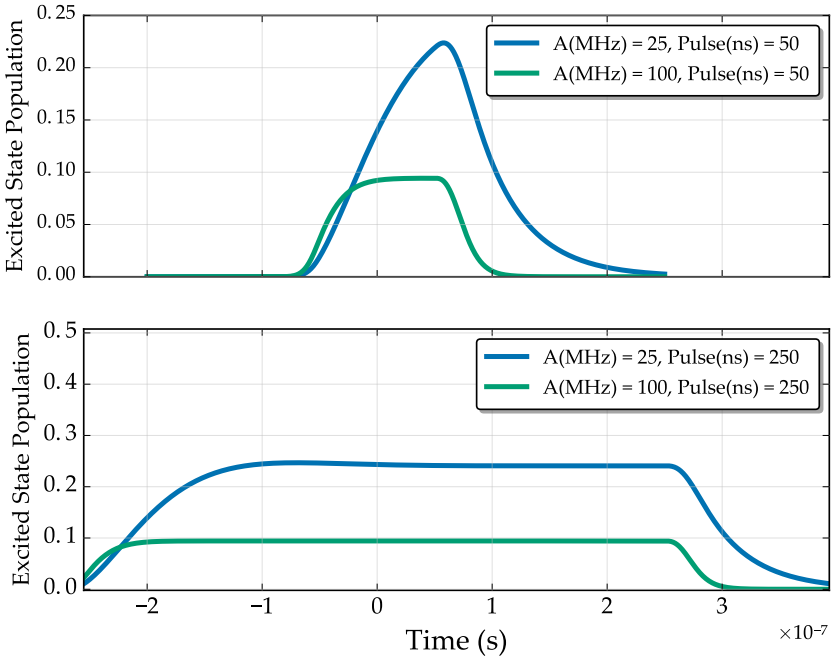

Figure 3.4: *Excited state population as a function of time for two different transitions and different pulse lengths. The difference in time before saturation and eventual saturation magnitude between different transitions is evident from the figure.*

not sufficiently long to allow the transition with the smallest A parameter to reach the steady state while it is more than long enough to reach saturation for the strongest transition. In the bottom part of figure 3.4, the pulse is of sufficient length to saturate both transitions.

In conclusion, the pulse length is important when optimizing the population transfer efficiency in the case the laser intensity is not the saturation regime of the transition (if $I \gg A_>$ in (3.5), the population density is independent of A). More importantly, the final steady state excited population is inherently larger for $A_<$ transitions than is the case for $A_>$ transitions when they are allowed time enough to saturate. The importance of the pulse length will be elaborated on further in this section.
The exact time dependent solutions of (3.5), are to be found in [6]. There, the solutions are obtained for the z-component of the Bloch-vector for on resonance excitation, to be compared to the Rabi-oscillations:

$$Z = -1 + \frac{\Omega^2}{\Omega^2 + A^2/2}\left[1 - \exp(-(3A/4)t)\left(\cos(\Omega_d t) + \frac{3A}{4\Omega_d}\sin(\Omega_d t)\right)\right]. \tag{3.10}$$

With $\Omega_d = \sqrt{\Omega^2 - \frac{A^2}{16}}$. Following (3.10), the steady state is reached exponentially with a factor $\exp(-(3A/4)t)$. Therefore, strong transitions equilibrate faster. Also in (3.10), the usual Rabi-oscillations are found; which now have an altered frequency determined by the decay rate.

3.4.3 Fixed Pulse Length

In figure 3.5, the ionization efficiency of a two-step RIS process is plotted as a function of the Einstein A parameter for the resonant excitation step. The second step is assumed to be none-resonant. Recall the influence of the Einstein A parameter on both the spontaneous decay lifetime and the coupling strength:

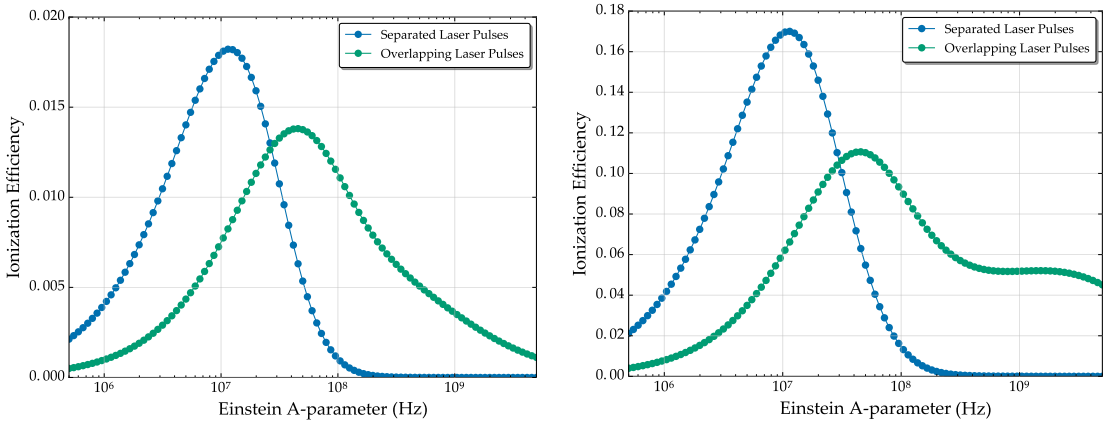

(a) *Excitation laser intensity = $10^{-3}J/m^2$, ionization laser intensity = $10^4J/m^2$*

(b) *Excitation laser intensity = $10^{-2}J/m^2$, ionization laser intensity = $10^5J/m^2$*

Figure 3.5: *Ionization efficiency as a function of Einstein A parameter for both overlapping and separated laser pulses. To show the influence of excitation and ionization laser intensity, (b) presents the same simulation results as (a) with both intensities increased by an order of magnitude. The competition between spontaneous decay and resonant excitation results in an optimal Einstein parameter for a given laser power. Differences between overlapping and separated pulses are explained in the text. The x-axis is plotted on a logarithmic scale.*

$$\tau = \frac{1}{A}, \Omega \sim \sqrt{A}. \tag{3.11}$$

Considering now a two-step excitation-ionization scheme for several A parameters, as explained in the previous section, an equilibrium will be found between excitation strength and decay. Figure 3.5 shows the results of the simulations. Here, the ionization peak efficiency for both completely separated and overlapping laser pulses is plotted as a function of Einstein A parameter for a fixed laser excitation pulse length.

In each case, three regions can be distinguished. In the first, for very low coupling strengths, one notices that the ionization efficiency has not had the chance to be built up. Next to this, for intermediate decay strengths, a clear rise in ionization is observed, which goes to a maximum. The third and final region of these graphs the represent a first geometrical difference in the curves represented by figure 3.5. The case in which excitation and ionization laser are separated in time, yields a near exponential decay of the ionization efficiency, conform the exponential decay of the excited state population. This tail eventually goes to zero when all population has decayed due to the strong spontaneous decay rate, leaving no population for the ionization laser to probe and thus rendering these lines useless for the purpose of laser delayed spectroscopy. For the overlapping lasers the story is markedly different. After a similar initial drop in efficiency after the maximum was reached, a much broader tail of the ionization efficiency for large decay strengths is obtained. The broader tail can be understood as follows: however strong the transition, as the ionization laser kicks in, the excitation laser still couples ground- and excited state. As can be seen at very large A parameters, the ionization peak will eventually also drop to zero due to the quantum overdamping effect [16] which renders any excitation impossible at very large Einstein A parameters, see section 3.5.

To understand the cause of the maximum in efficiency for a particular A-transition, the interplay between all parameters needs to be understood. As stated before, the maximum is a

competition between spontaneous decay, stimulated emission, resonant excitation and laser pulse length. Separating or overlapping the laser pulses changes the conditions in which RIS takes place, and therefore changes which value of the Einstein A parameter provides the best efficiency. To state this differently: depending on the timing properties of the lasers, the height of the resonance peak obtained in ionization experiments will be different because the presence of the ionization pulse during excitation changes the equilibrium conditions. Following the discussion in previous section, the A parameter offering this maximum efficiency is dependent on how long the resonant excitation pulse is compared to the time needed to reach the steady state population of the excited level. It is therefore intuitive to imagine that some A values will be optimal. The dependence on the pulse length, conform the theoretical predictions of section 3.4.2, is shown in figure 3.6. The A parameter offering maximum ionization efficiency is shifted towards lower values.
Important to note is that for the simulations discussed so far, the intensities of both laser were always the same. The (b) part of figure 3.5 now shows similar results for an excitation and ionization laser intensity which is increased by an order of magnitude compared to (a). The excitation laser power increases the parabola-like shapes and changes the width of the maximum. For laser intensities close to the saturation value the curve will grow towards a constant value for all A parameters. The ionization laser power on the other hand changes the ionization peak height. In addition, for overlapping laser pulses it increases the broad tail to a more saturation-like behavior. These observations alongside the previous discussion lead to the statement that depending on the fact whether both lasers overlap in time or not, a certain combination of powers can be found which maximizes the efficiency of the ionization process. However, changing laser powers is practically non ideal and therefore this optimization procedure was only a theoretical exercise.

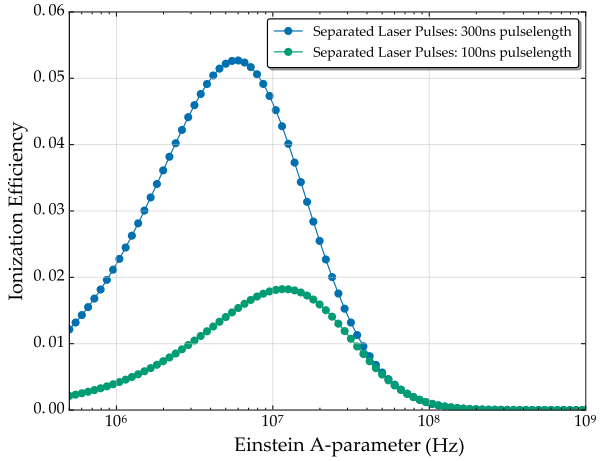

Figure 3.6: *Ionization efficiency as a function of Einstein A parameter for separated laser pulses for which the excitation laser pulse length has increased from* 100*ns (which has been the pulse length used until now) to* 300*ns to make the difference. The excitation intensity for the 100ns laser was chosen to be* 10^{-3}*J/m*^{2}*. To maintain the same laser power for larger pulse length, the excitation laser intensity was increased with a factor of three to* $3 \cdot 10^{-3}$*J/m*^{2}*. The markedly higher ionization efficiency plus the shift in the A parameter offering the maximum efficiency is as predicted in section 3.4.2. The x-axis is plotted on a logarithmic scale*

3.4.4 Variable Pulse Length

Alongside the inherent smaller linewidth that $A_<$ transitions present and the possibility for delayed laser ionization, sections 3.4.2 and 3.4.3 offer the ground work for a practical way of taking advantage of the higher steady state population obtainable for weak transitions. Via the combination of chopped cw-laser irradiation with low chopping frequency, a similar efficiency can be obtained as for pulsed laser application.
Recall (3.9), assuming that the excited state population reaches the steady state value, the efficiency can be maximized by choosing a weak transition, accompanied by long laser pulse lengths, or by increasing the power.

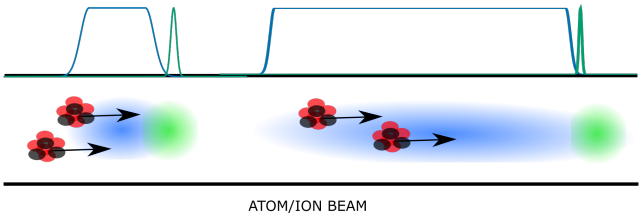

Figure 3.7: *Graphical representation of increasing pulse length for chopped cw-laser applications. The time dependence of excitation pulse (blue) and ionization pulse (green) are shown on the top. The direction of the particle beam is given by the arrows. Because of velocity of the photons, the particles are however almost standing still in comparison.*

In practice, assume two laser systems are available (the following situation is applicable for the CRIS experiment at CERN-ISOLDE), a high resolution, low power chopped cw-laser (see appendix section A.3.3) and and lower resolution, high power pulsed Ti-Sa (fixed pulse length) for the excitation step (the actual laser linewidth was not taken into account for the following simulations). The low power chopped cw-laser can be used to optimize the efficiency by increasing the pulse length (decreasing the chopping frequency, shown in figure 3.7. One could go to around $5\mu s$ pulse time for a 50keV beam in a meter of interaction length), while the pulsed laser systems will increase the power to achieve better ionization efficiency. Both systems can be applied to probe weak transitions with delayed ionization and all the advantages that it brings.
Figure 3.8, which presents simulations on a simple two-level scheme with a chopped cw-laser at varying chopping frequency, offers a graphical representation of the optimization process concerning the efficiency by increasing pulse length. For comparison with normal practice, overlapping pulsed lasers as well as separated pulse sequences are simulated.
Because strong transitions offer larger efficiency for short pulse length, overlapping lasers (bottom figure 3.8), these were until now the preferred transitions for laser spectroscopy purposes. However, it can be observed that increasing the pulse length inverts the most efficient transition to lower Einstein A parameters. The top part of figure 3.8 shows the same simulations for separated laser pulses. The trivial advantage of using weak transitions when delaying the ionization step is evident from the enormous efficiency difference with respect to the strong transitions.
If a pulsed laser system, with its superior intensity but fixed short pulse length, would be applied to this simulation, an efficiency which is shown on figure 3.8 is obtained. The fact that this efficiency coincides with that obtained by long pulse lengths again proves the interchangeability of both laser systems. A graphical representation of this is shown in figure 3.9. Using pulsed laser systems is equivalent to moving upward in the graph while using chopped cw-lasers

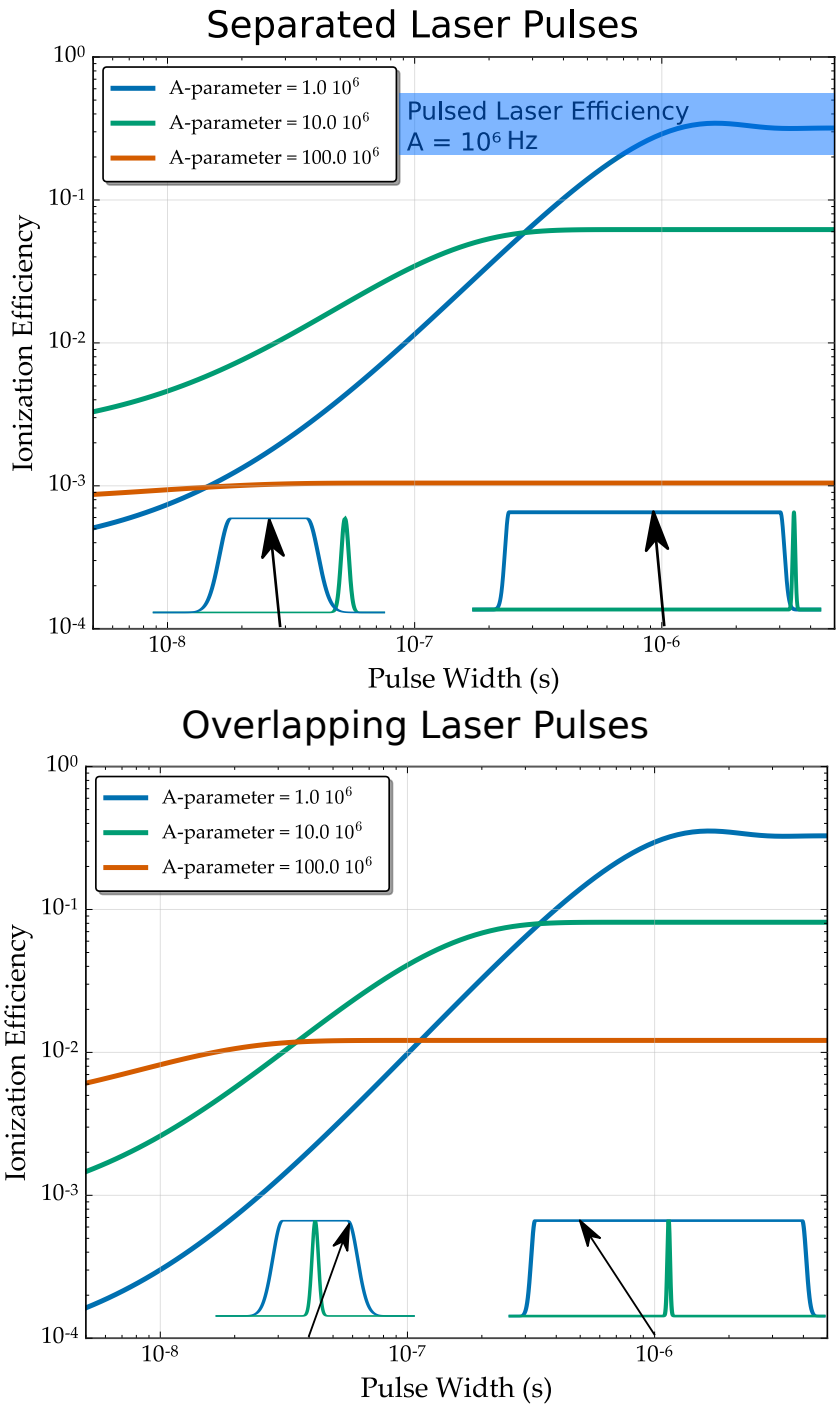

Figure 3.8: *Peak ionization efficiency as a function of laser pulse length for variable A-parameter transitions (given in units of Hz) obtained from both overlapping (bottom part) and separated (upper part) laser pulses (the insets show the exact time dependence of the laser pulses). The laser power is required to be independent of pulse length, therefore the total energy in the pulse scales with the pulse length. For short pulse length laser irradiation the expected higher efficiency is seen for strong transitions. By increasing the excitation laser pulse length however, one could clearly invert the efficiency behavior in favor of weak transitions. For separated lasers, using a much more powerful pulsed laser system which has inherent short fixed pulse length, the light-blue range of ionization efficiency can be obtained. Therefore making the excitation chopped cw-pulse longer brings the ionization efficiency closer to the one achievable with pulsed laser systems. Both graphs are plotted on a doubly logarithmic scale.*

with decreasing chopping frequency is moving right on the graph. Averaging out the Rabi oscillations for large excitation laser power brings the final efficiency in both cases to almost similar values.

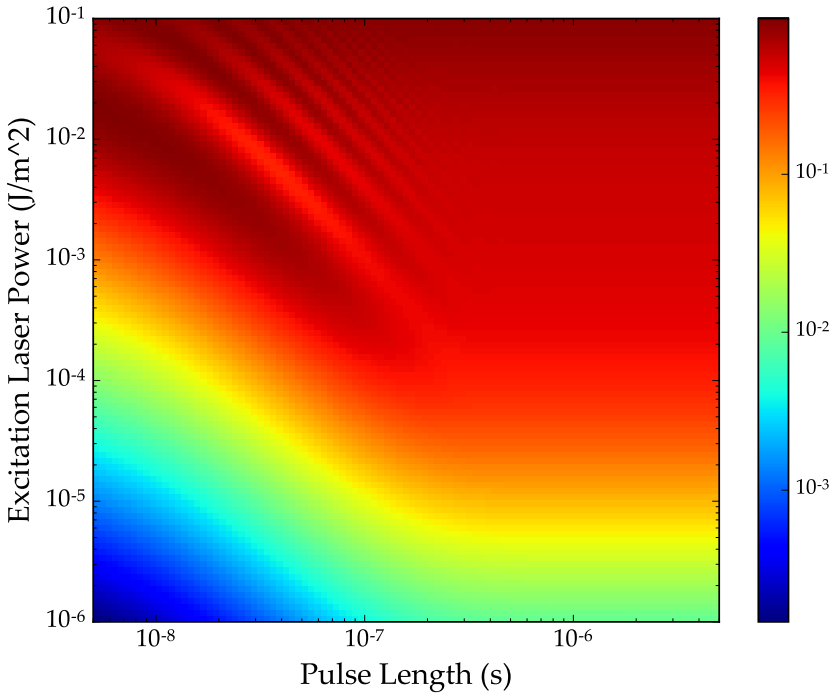

Figure 3.9: *Ionization efficiency as a function of pulse length and excitation intensity. This color plot shows the exact contribution chopped cw lasers could offer. The data is plotted on a doubly logarithmic scale. To obtain realistic values, the oscillating left upper part of the graph should be averaged. According to these simulations, both increasing laser intensity and increasing pulse length have similar influence on the acquirable efficiency.*

Therefore, assume the hyperfine parameters of a given weak transition require small bandwidth excitation lasers to acquire a clear splitting of level energies. In this case, the chopped cw-laser would be the laser system of choice due the superior linewidth characteristics of continuous wave lasers over pulsed lasers. Choosing for this low power option should decrease the efficiency. The preceding discussion however states that for low chopping frequency, no significant loss in efficiency should be observed.

Extending the discussion to multilevel schemes, gives figure 3.10, where the ground- and excited state are split into two sublevels and the excitation laser is tuned to one transition. Strong similarity between figures 3.8 and 3.10 is observed. However, while for the two-level simulations, indefinitely increasing the pulse length did not show any problems, multilevel-scheme simulations result in a decrease of efficiency for long pulse lengths. The reason for this is the optical pumping effect, which causes more and more population to reside in the dark state of the ground level which is not being probed, losing it for ionization purposes. Again for short pulse lengths, probing strong transitions with overlapping, fixed pulse length laser, remains the most efficient.

As an extra example, figure 3.11 is given, showing how the ionization efficiency dependents on the power in the excitation laser (two powers are presented). This graph summarizes a lot of the statements given above. First of all, one can see that the weak transition is saturated

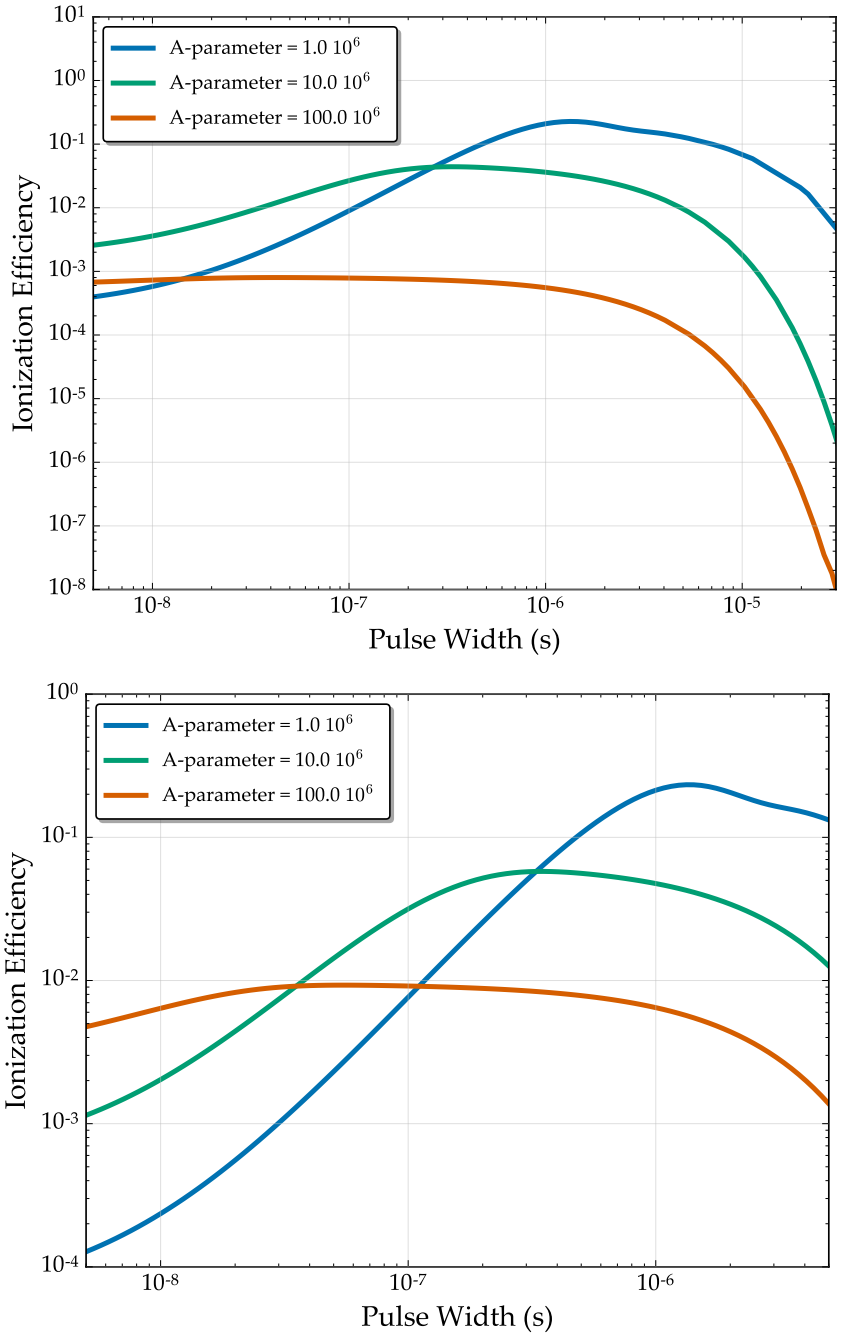

Figure 3.10: *Peak ionization efficiency as a function of laser pulse length for variable A-parameter transitions (multilevel scheme with the A parameters given in units of Hz), to be compared with figure 3.8. By increasing the excitation laser pulse length too far, one will enter the optical pumping region, losing population transfer efficiency. The data is plotted again on a doubly logarithmic scale.*

because of the similar ionization efficiency for long pulse lengths in both cases. However obtaining this steady state population requires longer time for smaller laser intensities. Similar conclusions can be obtained for the strong transition. In this case however the difference in the efficiency for both laser powers show the fact that strong transitions appear more difficult to saturate. This will be discussed in the next section. The efficiency for short pulse length, strong transition, excitation or long pulse length, weak transition, excitation grow towards each other for increasing power as the transitions both start to saturate. This observation confirms that powerful enough laser pulses will not distinguish between A parameters and short pulse lengths should be suffice in this case. The curves in figure 3.11 with low power are obtained with intensities comparable to experimental continuous wave lasers (chopped).

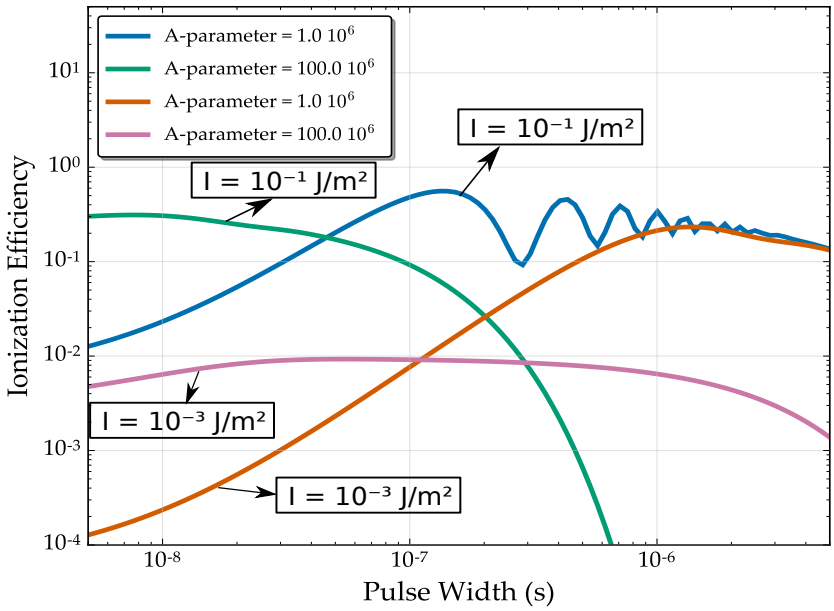

Figure 3.11: *Ionization efficiency as a function of pulse lengths obtained with two excitation laser intensities, two orders of magnitude different for two A parameters (given in units of Hz). The data is plotted on a doubly logarithmic scale.*

As a conclusion, in addition to their inherently smaller linewidth, $A_<$ transitions offer low efficiency losses when delaying the laser pulses. This delaying procedure offers improvements on precision and multiple line distortion effects as discussed before. Alongside this, a weak transition can be optimized to obtain greater ionization efficiency with variable excitation pulse length irradiation, obtained via chopped cw-lasers. Additionally, this chopped cw laser carries an inherently smaller laser linewidth, further improving the spectral precision. Employing this procedure, an experimental efficiency close to the one obtained for pulsed laser sequences is achieved.

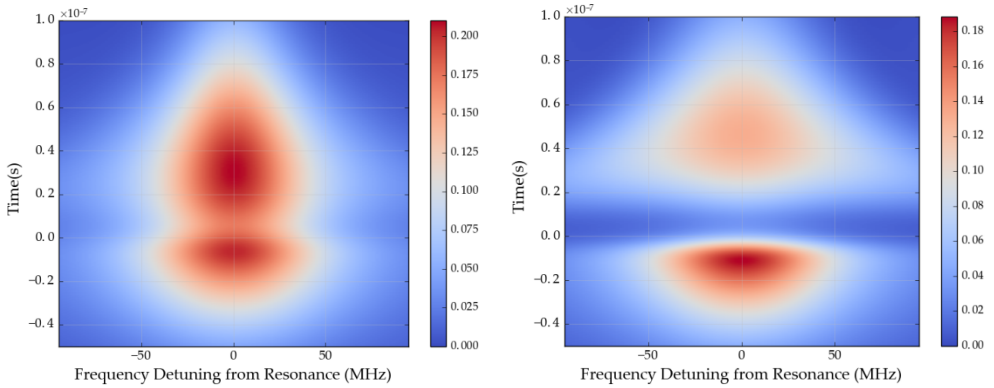

(a) *Non-saturating ionization laser power* ***(b)*** *Saturating ionization laser power*

Figure 3.12: *These simulation results show the population of the excited state as a function of time on the vertical axis and frequency on the horizontal for a long excitation pulse and overlapping short ionization pulse. In (a), one can clearly see that the ionization laser, which is interacting at a central time in the figure, is not ionizing all available population residing in the excited state. The converse is true in (b), where the ionization power was chosen in the saturation range of the transition, thus depleting all population from the excited level into the ionization continuum.*

3.5 $A_<$'s saturation

As a next subject of interest in laser spectroscopy experiments, the saturation curves of a transition were simulated for a normal pulse length. Again, these simulations will show that $A_<$ transitions have beneficial characteristics for application in spectroscopy experiments. The saturation curves show the ionization efficiency, or the height of the ionization peak of one particular transition, as a function of both the ionization laser power and the excitation power. One expects a saturation-like behavior for both cases. For example the ionization laser will clear out the excited state population until the power reaches the saturation value for which all population in the excited state has been ionized and further increasing the power has no effect. An example of saturating the ionization laser is shown in figure 3.12. Saturation curves are important in experimental practice. Employing laser powers which do not come close to the saturation value will result in low efficiency, while too large laser powers induce large power broadening effects in the spectral resonances.

3.5.1 Ionization Saturation

First of all, saturating the ionization laser will prove to be more easily achieved for weak excitation transitions. To begin, the peak height of the ionization spectrum was plotted for multiple A parameters as a function of ionization laser intensity. All saturation curves are plotted with a logarithmically spaced x-axis to increase the dynamic range.
Figure 3.13 shows the saturation of these transitions, obtained via simulations for separated laser pulses for a simple two-level scheme. The (b) part presents the absolute efficiency values. For separated laser pulses, the fact that delaying the pulses has a significant detrimental effect on the ionization efficiency of strong transitions is clear. For these simulations however, the interest goes to the saturation behavior of the different A-parameter transitions. To cancel out the effect of the spontaneous decay for separated pulses, the different saturation curves

were normalized to their saturation value. This is shown in the (a) part of figure 3.13.
From this, clearly $A_<$ transitions reach their saturation value for lower powers. Intuitively this can be understood as follows: for separated laser pulses and a fixed excitation laser power for all A transitions, a certain population in the excited level is presented to the ionization pulse. When the ionization pulse starts to interact with the atom, the fraction of the population which will be ionized is governed by the competition between the ionization process and the spontaneous decay. Note that the ionization laser only affects the ionization process while the value of the A parameter on the other hand only affects the strength of the competing spontaneous decay. Therefore, for $A_>$ transitions, more population will decay back to the ground state rather than be ionized and the ionization laser will need a larger increase in power to obtain the same increase in efficiency as for a $A_<$ transition.

The preceding simulations were done for separated laser pulses to further highlight the loss in efficiency for $A_>$ transitions. The same exercise can be done for overlapping laser pulses. The simulation results are shown in figure 3.14. The saturation behavior for different A-parameter transitions is although less pronounced, similar to the curves in 3.13. However a difference is observed in the apparent decrease of ionization efficiency for large ionization laser powers. This effect could be assigned to the quantum overdamping effect discussed in [16]. Assume a simple excitation-ionization model, without spontaneous emission, is treated. For a two-level scheme and cw laser irradiation, one can obtain following differential equations governing the time evolution of the overlap between the sate vector with both the ground state ($\alpha(t)$) and the excited state ($\beta(t)$):

$$\begin{aligned} \frac{d\alpha(t)}{dt} &= -i\frac{\Omega\beta(t)}{2}, \\ \frac{d\beta(t)}{dt} &= -i\frac{\Omega\alpha(t)}{2} - \frac{\Gamma\beta(t)}{2}. \end{aligned} \tag{3.12}$$

In this equation, Ω represents the Rabi coupling parameter and Γ controls the ionization rate. Numerically solving these equations for arbitrary parameters and displaying them as saturation curves gives figure 3.15. Similar as to figure 3.14, a decrease in ionization efficiency is predicted for large ionization laser power. Following the aid of this simple model, this decrease can thus be explained as a consequence of the quantum overdamping effect, in which too large loss rates render the excited state invisible for the ground state level.
This argument can be extended to a pulsed laser application. For overlapping pulses, the excitation efficiency will decrease when the ionization laser is present and therefore the overall ionization efficiency will drop for large laser powers. For separated pulses however, no excitation occurs when the ionization laser fires and therefore, the quantum overdamping effect will remain invisible in this case as can be seen when comparing figure 3.13 with 3.14.

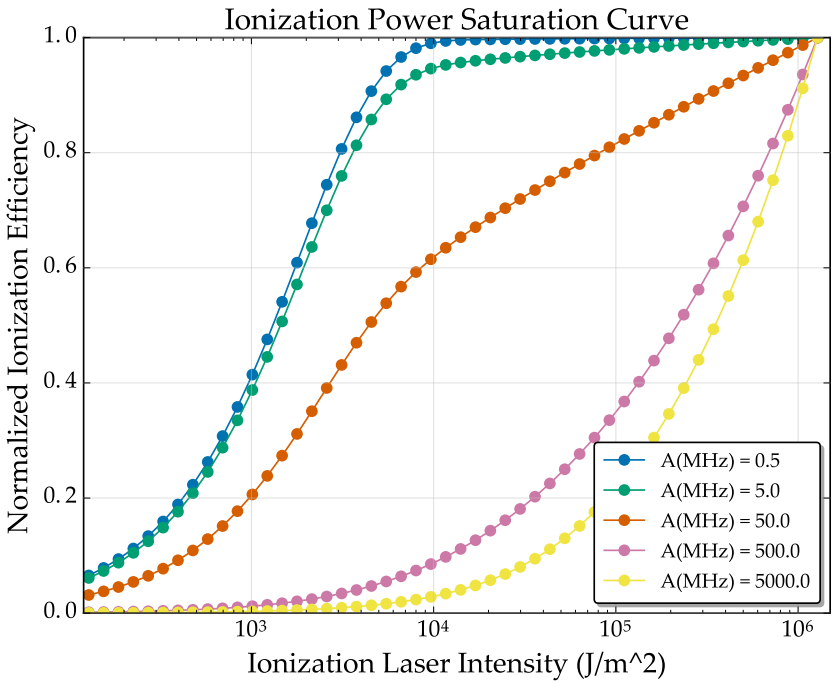

(a) *Normalized ionization efficiency as a function of ionization laser power for a range of A parameters*

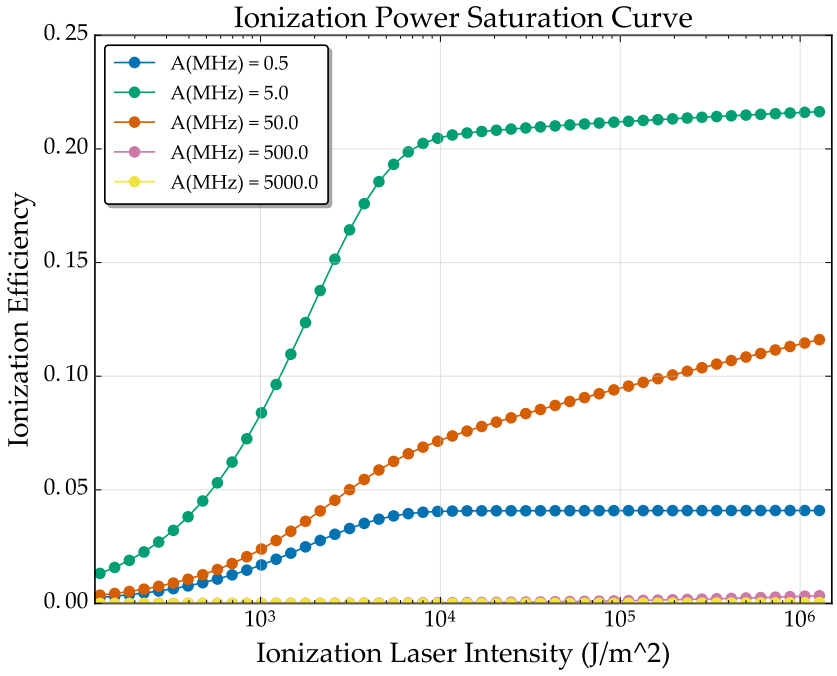

(b) *Absolute ionization efficiency as a function of ionization laser power for a range of A parameters*

Figure 3.13: *Saturation spectra as a function of ionization laser intensity for a range of A-parameter transitions simulated in the case of separated laser pulses. (a) Showing the normalized curve while (b) contains the absolute efficiencies. The differences both in the drop of absolute efficiency and the lower saturation rate for $A_>$ transitions compared with $A_<$ transitions, show two arguments why one should opt for $A_<$ transitions. The exact value of the saturation efficiency depends on the excitation laser power and pulse length. The x-axis is shown on a logarithmic scale to improve the visibility of the effect.*

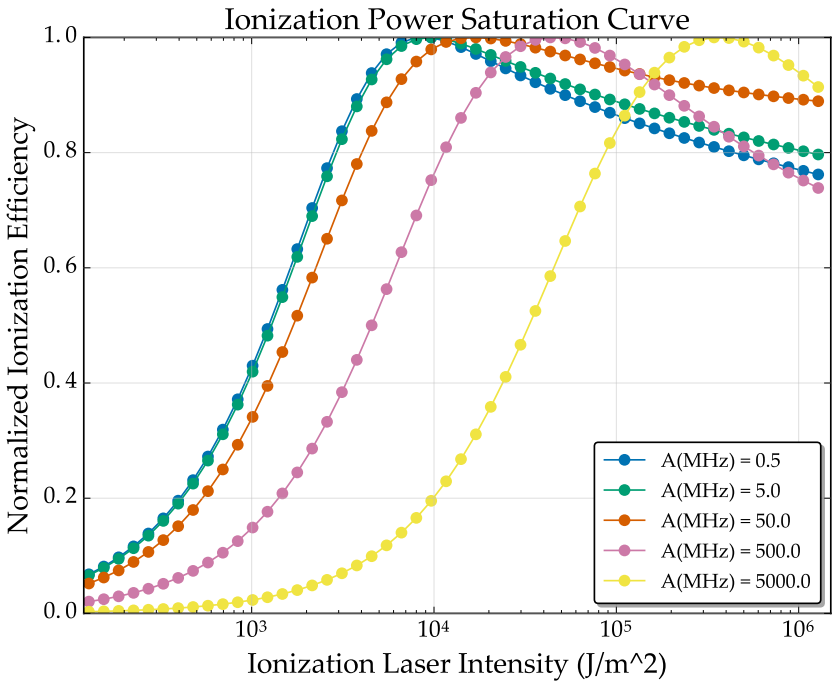

(a) *Normalized ionization efficiency as a function of ionization laser power for a range of A parameters*

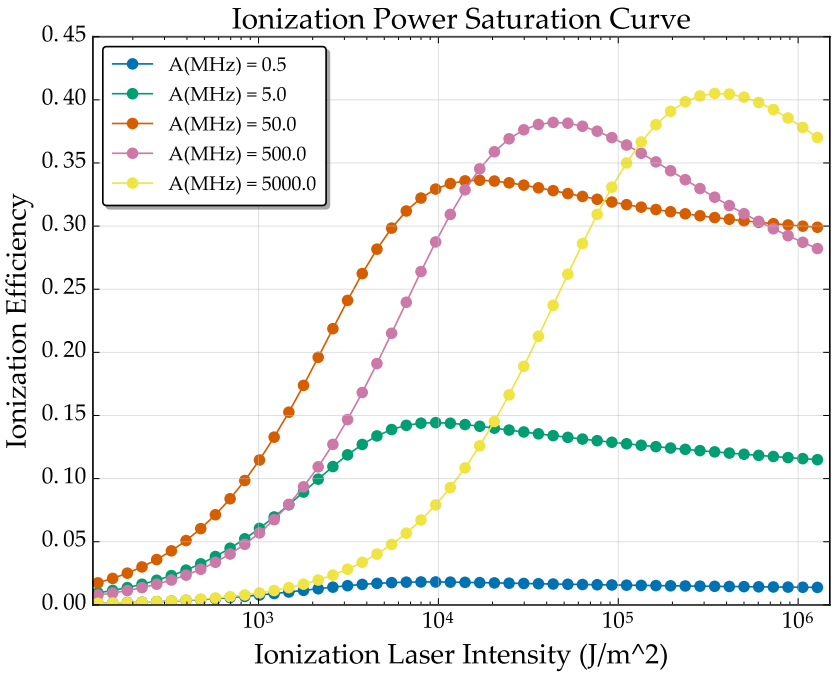

(b) *Absolute ionization efficiency as a function of ionization laser power for a range of A parameters*

Figure 3.14: *Saturation spectra as a function of ionization laser power for a range of A-parameter transitions simulated in the case of overlapping laser pulses. (a) Showing the normalized curve while (b) contains the absolute efficiencies. Similar conclusions as for figure 3.13, except for the decreasing efficiency at large laser intensity. The ionization laser power is shown on a logarithmic scale to improve the dynamice range.*

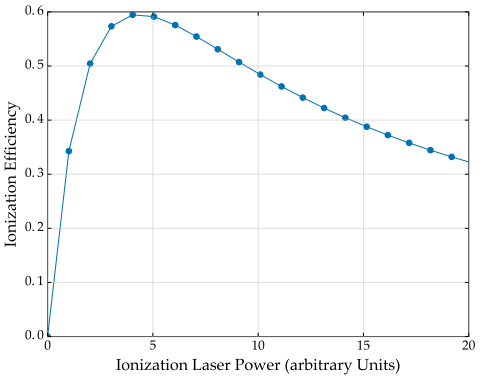

Figure 3.15: *Numerical integration of the first order differential equations* (3.5.1) *offered the ionization efficiency dependence on ionization rate. For this simple model, the drop in efficiency for large laser power found in 3.14 is also predicted.*

3.5.2 Excitation Saturation

Similar simulations as for the previous section were performed to obtain the dependence of the ionization efficiency on excitation laser power. Both cases of separated and overlapping laser pulses were treated again separately. Figure 3.16 shows the absolute ionization efficiency as function of intensity obtained in both these simulations.
For overlapping laser pulses no significant change in saturation behavior can be distinguished. The description of the process in this case is rather difficult because the ionization laser disrupts the excitation dynamics. As a result of this, also saturation values beyond 50 percent are obtained.
For separated laser pulses however, a very similar graph to figure 3.13 is obtained. A$_>$ show once again a decreased saturation rate compared to A$_<$ transitions. To understand the saturation behavior for separated pulses which is of interest in this report, the model of [7] and [6], already discussed in 3.4.2, is consulted. In this case the ionization pulse is taken to be constant and the excited state population as a function of the excitation laser power is of interest. Going back to (3.7) in section 3.4.2 and including equality (3.1), one obtains:

$$\begin{aligned} P_{exc} &= \frac{\varrho/2}{1+\varrho}, \\ \varrho &= \frac{2\Omega^2/A^2}{1+4\Delta^2/A^2}, \\ \varrho &\sim \frac{I}{A}. \end{aligned} \tag{3.13}$$

To recapitulate, A and I are respectively the Einstein parameter and the laser intensity which are put into an easier form by defining ϱ . To give a qualitative understanding of the difference in saturation behavior, one could look at low powers, where the efficiency is roughly linear. Therefore taking (3.13) and expanding it as a Taylor series, following equation is obtained:

$$P_{exc} = \left(\frac{\varrho}{2} - \frac{\varrho^2}{2} + \frac{\varrho^3}{2} + ...\right). \tag{3.14}$$

The slope of the saturation curve for small powers is inversely proportional to the Einstein A parameter of the transition. This behavior is recovered in the full simulations of figure 3.16, when shown on a linear scale. At small powers however still familiar Rabi-oscillations are found.

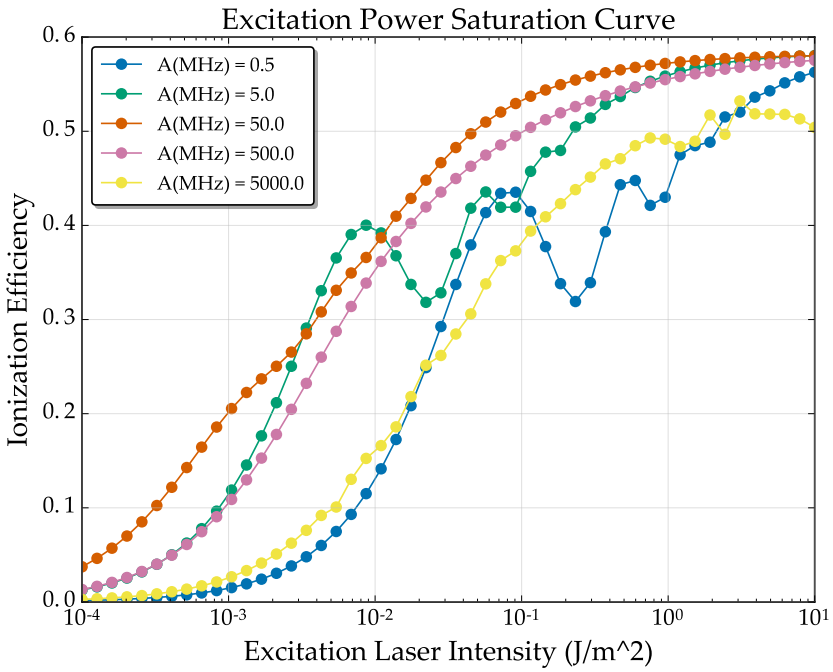

(a) *Ionization efficiency for overlapping pulses*

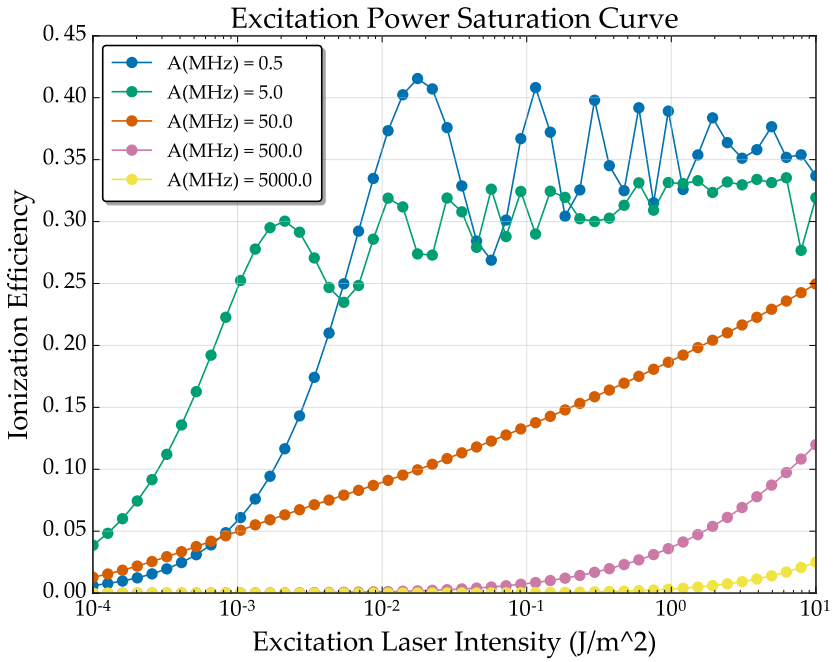

(b) *Ionization efficiency for separated pulses*

Figure 3.16: *Saturation spectra as a function of excitation laser intensity for a range of A-parameter transitions simulated in the case of overlapping laser pulses in (a) and separated in (b). Both graphs show absolute efficiencies. Again for $A_<$ an larger saturation rate is obtained. Laser itensity is again shown on a logarithmic scale.*

One can conclude that weak transitions are inherently easier to saturate. From (3.13), the conclusion can be drawn that for sufficiently large excitation laser power, the saturation population of the excited state becomes $1/2$, independent of A. Applying pulsed lasers, this translates into the fact that for large enough laser pulse lengths, all transitions saturate at $1/2$ for sufficiently large laser intensities. These transitions start to saturate from laser intensities of around $10^1 \mathrm{J/m}^2$ for the system simulated in the figures.

3.6 Fourier and Laser Linewidth

Alongside the inherent lifetime and power broadening contribution to the Lorentzian profile of the resonance peak, two other additions to the linewidth can be distinguished in the absence of any collisional or pressure effects.
First of all a Gaussian contribution to the frequency domain comes from the Fourier transform of the Gaussian laser pulse in time. An example is given in (a) of figure 3.17. A long Gaussian pulse in the time domain results in a small Gaussian contribution to the spectral linewidth while the reverse statement is true for the opposite case. The Gaussian contribution should be as follows:

$$FWHM_{Gaussian} = 2\sqrt{2\ln(2)}\frac{1}{\sigma_{Gaussian}}. \tag{3.15}$$

In (3.15), $\sigma_{Gaussian}$ stands for the standard deviation of the Gaussian laser pulse in time space. Indeed as the simulations in (a) of figure 3.17 show, for a single frequency, low power, weak transition, ionization spectrum, the Voigt profile is almost entirely Gaussian.
In addition to this, the assumed Lorentzian limited bandwidth of the excitation laser brings an extra Lorentzian contribution to the spectral linewidth, as discussed in 2.3. To work out the validity of the laser linewidth influence on the spectra, the laser coupling the two levels was simulated first as photons of one unique frequency only and then with a limited bandwidth of

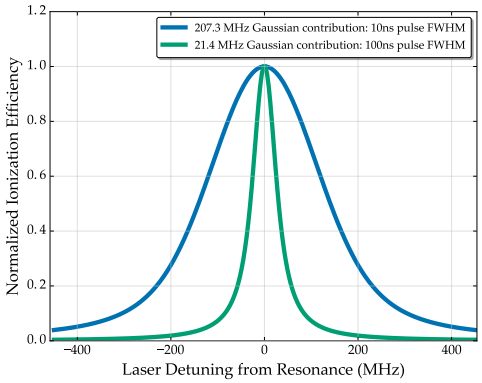

(a) *Ionization spectra obtained with two excitation laser pulses. The first is a pulse which has a duration in the time domain of 100ns FWHM while the other lasts for 10ns FWHM. The Gaussian contribution reduces indeed by a factor of 10.*

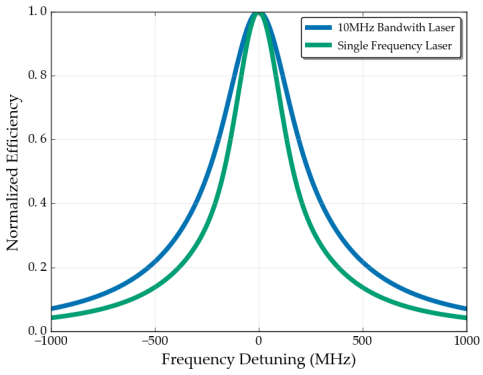

(b) *Ionization spectra obtained with two excitation laser pulses. The first is an ideal laser with singular frequency, the other is a realistic laser having a bandwidth of 10MHz. The extra Lorentzian contribution in the second case is indeed 10MHz*

Figure 3.17: *The influence of both the Fourier transform of the excitation pulse and of the laser linewidth on obtained precision is presented.*

10MHz. The results are shown in (b) of figure 3.17.
Finally, one should recall the conditions raised in section 2.3. In the light of the theoretical discussion held in that section, the addition of the laser linewidth can not be done when the magnitude of HWHM of the Lorentzian frequency profile of the laser beam is greater than the decay rate or close to the energy splitting between the levels. In this case, the decoherence time will completely be determined by the laser linewidth which is not allowed by this model.

3.7 Extra Considerations

3.7.1 Ac-Stark Shifts

As an attempt to explain the broad tail behavior of figure 2.1, section 2.4.1 proposed the inclusion of the ac-Stark shift to the energy value of the states coupled to the continuum. To understand the consequences of the addition, the influence of the Stark shift to simple simulations was investigated first. Then, in the next chapter, an attempt is made to simulate the experimental data in figure 2.1.
As explained before, a rigorous form of this ac-Stark shift is theoretically known, see (1.6), but very difficult to include in the simulation code. The problem lies in the determination of the matrix element $|\langle 1|V(t)|\epsilon,\omega_\epsilon\rangle|^2$. Luckily, one can show that the matrix element can be approximated by a function which is linearly proportional to the ionization laser power [14]. Therefore, it was chosen to represent the Stark shift, which is an adaptation of the excited state energy levels as an unknown factor times the incoherent lasesr power. The unknown

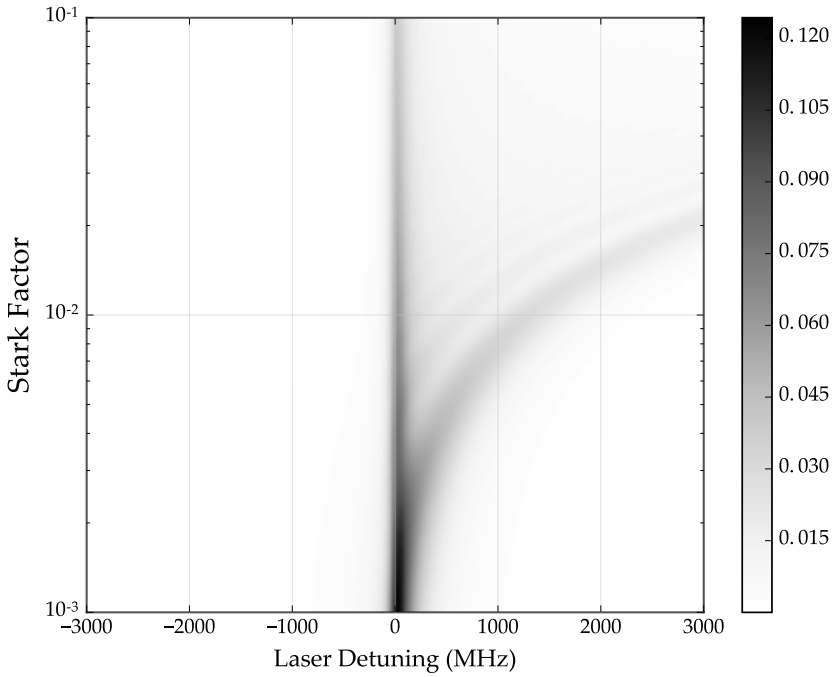

Figure 3.18: *Ionization peak efficiency as a function of both Stark factor and excitation laser frequency. The appearance of the Stark tail is clearly visible for increasing Stark factors. The rise of the secondary peak and waves in between both peaks are caused in this model by the Gaussian ionization pulse shape and the Rabi oscillations.*

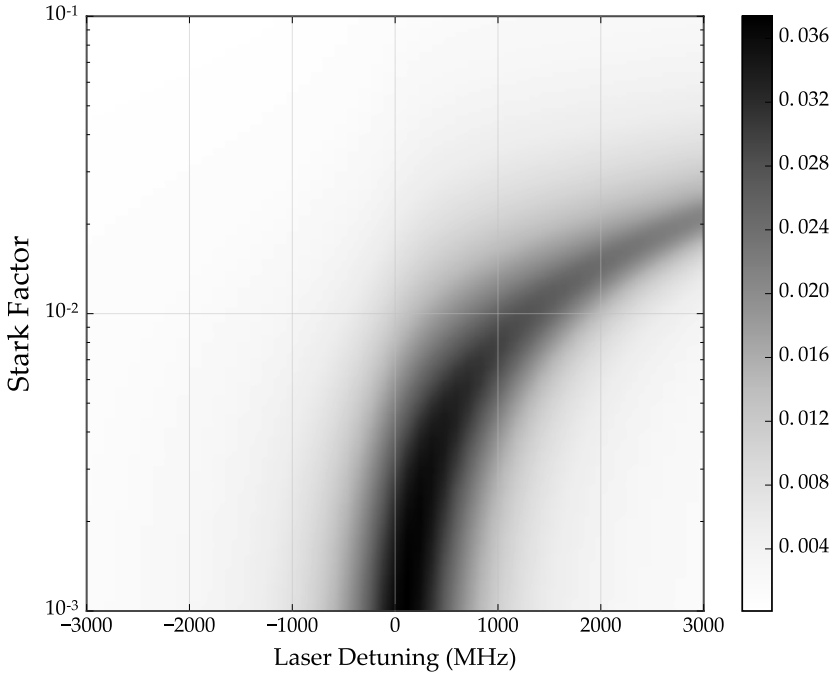

Figure 3.19: *Ionization peak efficiency as a function of both Stark factor and excitation laser frequency for an Einstein A parameter an order of magnitude bigger than in figure 3.18. The disappearance of the primary resonance alongside the blurring of the Rabi waves is significant.*

factor is called the Stark factor in the following discussion. The influence of the Stark factor to the spectral lineshapes will now be discussed for weak and strong transitions.
Simulations were performed for a range of Stark factors with overlapping excitation and ionization lasers. To visualize the simulations more clearly, the ionization efficiency of the two-level system as a function of the unknown Stark factor and the laser detuning are shown in figures 3.18 and 3.19. A horizontal slice would present a common ionization spectrum.
Figure 3.18 shows the results obtained for simulations on a weak transition. The appearance of the tail, can be understood from the arguments of section 2.4.1. In this model the time dependent Stark shift mimics the Gaussian time dependence of the ionization laser. Therefore it shifts the energy level continuously up (or down, dependent on the sign of the Stark factor) and back down to the original energy value when the ionization pulse dies out. Therefore, non-resonant laser photons could become resonant at a certain time for a particular ionization laser power, explaining the resonance's tail. Changing the sign of the Stark factor would then mirror the tail around the resonance frequency. For large Stark factors, this tail evolves into a distinct secondary peak. This asymmetry appears in this particular model because the state energy goes up and down again in time as a function of the Gaussian time dependence of the laser intensity. The excitation mechanism has therefore more time to accumulate population in the excited state while the Stark shift is maximal. Slightly altering the shape of the ionization laser therefore could have a significant influence on the appearance of the secondary peak according to this model.
In figure 3.19, similar simulations are shown as in figure 3.18 for a strong transition. In addition to the increased linewidth, the actual resonance line disappears. This disappearance of the resonance line is because all population that is excited prior to the arrival of the second laser

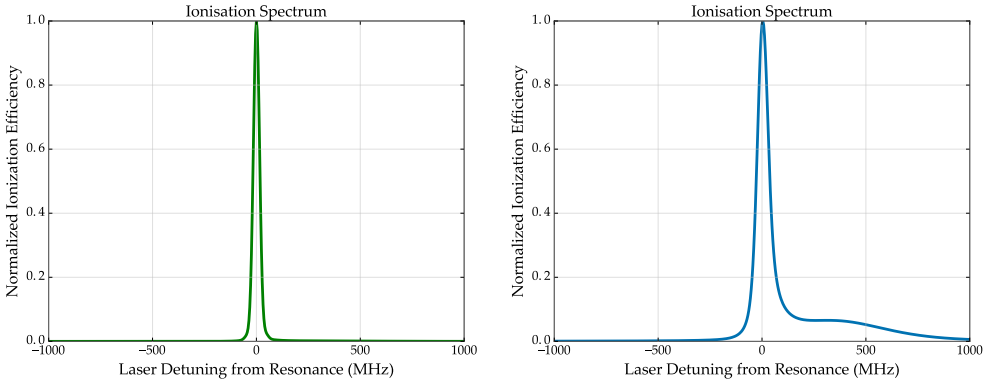

(a) *Delayed Laser Pulses.* ***(b)*** *Overlapping laser pulses .*

Figure 3.20: *Single transition ionization spectrum for delayed and overlapping laser pulses with included Stark shift. Excluding the perturbing ionization laser from the excitation process explains the absence of the Stark shift for delayed laser pulses. For overlapping laser pulses however the distinct Stark tail arises.*

will have decayed back to the ground state and will not lead to ionization. Excitation followed by ionization occurs only during the time that the ionization laser is present. Potentially, this effect could shift the resonance peak in frequency space and reduce therefore the accuracy of the experiment.

The Stark tail can be completely canceled when both laser pulses are fully separated in the time domain. Therefore, powerful ionization lasers can be used for delayed ionization on weak transitions, without any distorting effects, see section 4.1.
The influence of the power of both lasers on these simulations can be explained as follows. Increasing the excitation laser power will only increase the height of the tail in the spectrum due to increasing excitation efficiency during the presence of the ionization laser. Increasing the power of the ionization laser will have a similar effect as increasing the Stark factor because both are linearly added to the diagonal of the interacting Hamiltonian.
Finally an example of the line distorting nature of the Stark-shift is shown in figure 3.20.

3.7.2 Multi-Step Simulations

More advanced three-level schemes to even four-level schemes were already used in experiments, for example see [17], as explained in section 2.4.2. In that section, the recipe for developing the code to deal with this arbitrary number of laser steps and number of levels was explained.
To allow for simulations on an arbitrary choice of laser excitation steps, the simulation code was completely rewritten in an object oriented way. Via a new integrated graphical user interface, an array of classes can be called which grants the user the possibility to study the relevant parameters of multi-step laser excitation-ionization experiments via the use of simulations.
As a simple example, the level scheme shown in figure 3.21 is simulated for completely overlapping pulses. The result is shown in figure 3.21. The addition of the extra quantum level in the simulation code will be used in the next chapter as well.

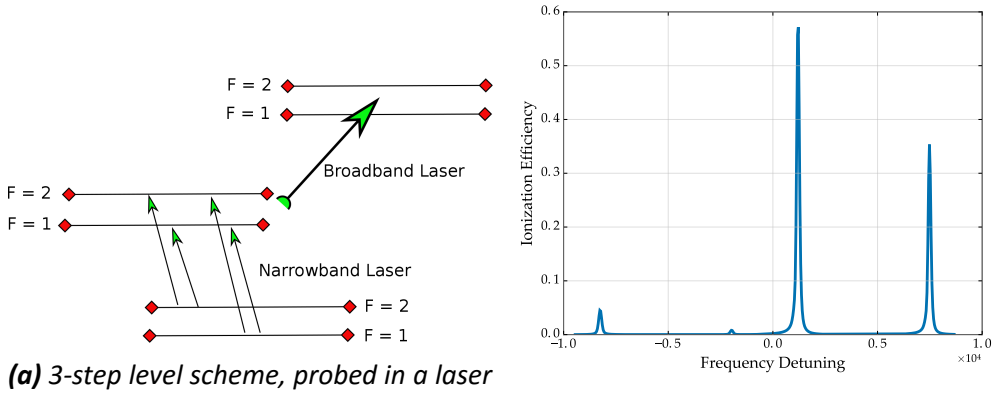

(a) *3-step level scheme, probed in a laser spectroscopy experiment.*

(b) *Overlapping laser pulses simulation.*

Figure 3.21: *On the left, a 3-step level-scheme being probed by 3 lasers (the ionization laser is not shown). In this example, a narrowband laser scans the first step while a second laser is applied to reach the level from which the third laser can ionize the ensemble. On the right, a simulated ionization spectrum for this 3-step level-scheme. The second excitation laser was closely tuned to one of the resonances (not sufficiently broadband), reducing therefore the amplitude of two out of four transition lines*

3.8 Conclusion

In the introduction, 5 properties of weak transitions were presented which showed that they are more suitable for laser spectroscopy purposes than strong lines. First of all, these transitions have an inherently small linewidth. Furthermore, they offer the possibility to delay excitation and ionization laser pulses in time. By doing this, the experimental resolution can be improved and spectral line distortions (such as the ac-Stark effect) removed without reducing the efficiency. In addition to this, weak transitions offer an alternative towards very efficient, high resolution spectroscopy by using long excitation pulse lengths combined with a delayed ionization laser. Finally, $A_<$ transitions show advantageous saturation characteristics. All of these elements were confirmed by simulations using the models developed in this work and in [1]. Depending on the particular goals and restrictions of the experiment, the simulation code allows for the determination of a range of suitable small A parameters to optimize the conditions. Or alternatively, if a transition with a specific A is used, the laser power, laser pulse length and ionization laser delay time can be optimized for the optimal experimental efficiency, using the simulations.

Chapter 4

Experimental Comparison

To make a qualitative judgment on the model and objectify stated assertions on improving the quality of experimentally obtained data via laser related characteristics, the model was compared to experimental results obtained in 2 campaigns. In previous work, other experimental comparisons can be found [1]. More details on the experiment and a more profound discussion of the results can be found in appendix B.

4.1 Fr Campaign: CRIS

In this section, the simulation code will be applied to the experimental data already mentioned in section 2.4.1. This RIS data was obtained by exciting ^{221}Fr from the electronic $7s^2S_{1/2}$ ground state to the $8p^2P_{3/2}$ excited level at 23658.306cm^{-1}, with a transition strength of $2.8 \cdot 10^6$Hz [13], in the CRIS experimental setup at ISOLDE, CERN. Afterwards this excited state was non-resonantly ionized to the continuum via 1064nm laser light at 100Hz. The level scheme and the transitions studied here are shown again in 4.1. The spectra present strong line shape distorting effects which could be related to the high ionization laser power, see figure 4.2. As can be observed in the experimental data, these line distortions disappear when both laser pulses are delayed, enforcing the argument that the powerful ionization laser is the cause.
The experimental data obtained in this experiment represents therefore an ideal subject for investigation for its a clear example of how a small-A transition accompanied by delayed ionization improves resolution, removes line distortions and retains ionization efficiency.

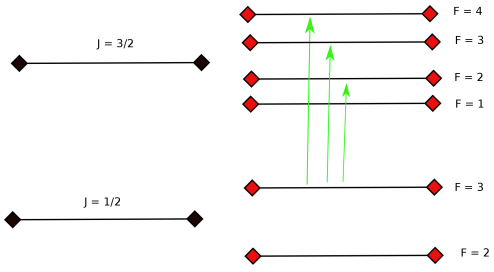

Figure 4.1: *Francium-221 level scheme probed in the CRIS experiment at ISOLDE-CERN as explained in section 4.1.* ^{221}*Fr has a spin of* $5/2$.

As input to the simulation code, several parameters from the experimental setup are gathered (see table 4.1). In addition to electronic quantum numbers, Einstein A parameter, laser

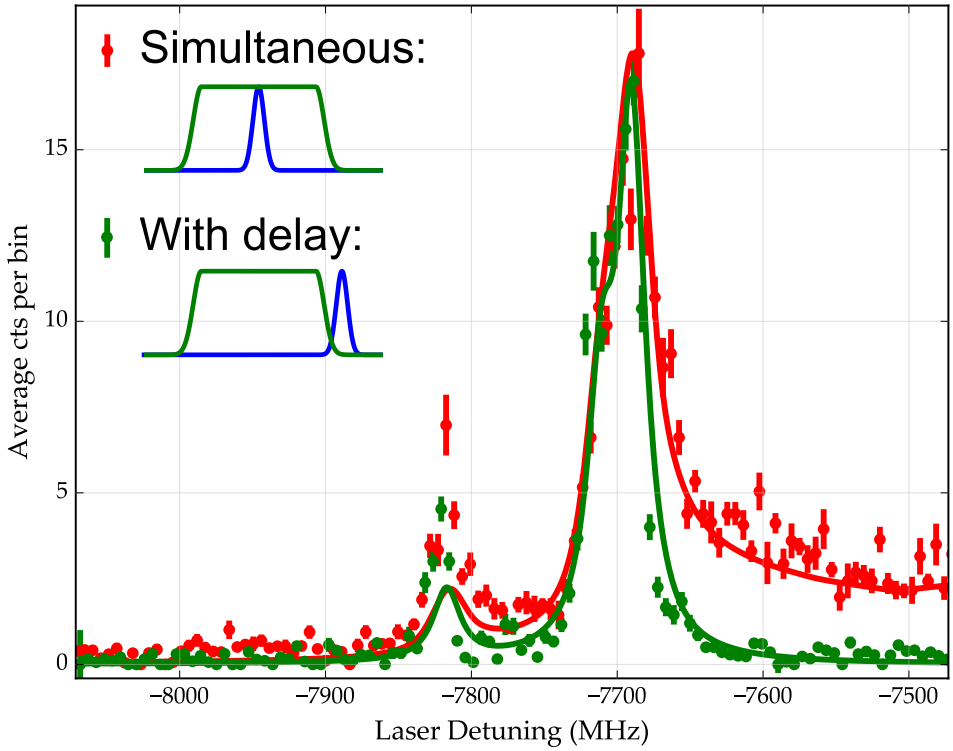

Figure 4.2: *Simulated resonance ionization spectrum for ^{221}Fr data obtained with partially overlapping excitation and ionization lasers shown in the inset. Only the lowest energy multiplet that is expected is shown. Experimentally obtained data is visualized by points while the simulations are provided as a solid line . The influence of the added stark-shift is remarkable, as it forms a continuous tail at the back end of the peaks. Important note: in order to compare with experimental data, the simulations were converted from angular frequency space to regular frequency space. To match the data, the simulated spectrum was scaled to the amplitude of the highest spectral resonance.*

wavelengths and obtained hyperfine parameters, the pulse lengths and laser power densities are required as input. The laser pulse sequence in time used for this experiment is shown in the inset of figure 4.2. To take advantage of the smaller linewidth of cw lasers, the excitation pulse is a chopped cw laser pulse, of length 100ns, as explained in section A.3.3. The excitation laser provided 250mW/cm^2 at the CRIS beam line while the ionization laser produced 32W/cm^2. The input data for the simulations requires input intensity, presented in mJ/pulse. For a cw laser, the intensity is continuous in time. Therefore to obtain the number of mJ per pulse, one just has to multiply 250mW/cm^2 by the pulse length. For pulsed lasers however, the repetition rate of the laser is important. In this case, dividing 32W/cm^2 by the repetition rate will give the intensity needed. More information about the experiment and the results can be found in appendix B.

The solid line simulations plotted on top of the experimental data points are visible in figure 4.2. Quoted experimental linewidths constitute of around 4MHz Lorentzian contribution and around 13MHz Gaussian for the data of 4.2. Applying a fitting procedure on the simulations, for the delayed laser pulses of figure 4.2 respectively a few MHz Lorentzian (strongly dependent on the exact input of the excitation laser intensity) and 6MHz Gaussian is recovered, therefore not

quite resembling the experiment. The relatively large Gaussian contribution to the experimental linewidth is not understood. The simulations also fail to reproduce the intensity of the left-most peak. This could be explained by a slightly different value of the laser power for the excitation step which alters the relative intensities. Except for this, the simulations fit the data remarkably well, with the focus on the asymmetric Stark tail. Eventually a Stark shift of $S(t) = 4\Gamma(t)$ proved to offer the best overlap between data and simulations. Important to add is the lack of ionization efficiency loss for the spectrum obtained with separated laser pulses. This is a result of using a weak transition.

Two side notes should be made concerning the simulations.
First of all, the pulse shape of the ionization laser was parametrized as follows: a Gaussian-like peak with an asymmetric long tail at the right. This parametrization was chosen to match the specifications provided by the manufacturer of the laser. Using this parametrization, the secondary peaks observed in simulations with pure Gaussian shape, see section 3.7.1, are flattened out. This observation that the Stark shift is significantly dependent on the ionization pulse shape is surprising and would be interesting to investigate experimentally. By the design of the laser, the ionization pulse consists of two temporally overlapped laser pulses. By for instance delaying these two pulses with respect to each other, interesting data on the details of the role of the pulse shape might be obtained.
The simulations also revealed resonance effects coming from the interplay between the stark shift and the excited state-continuum coupling. These resonance effects showed a series of secondary bumps at the right side of the spectrum. The simulations in figure 4.2 no longer show these bumps. They disappear when the spatial power distribution of the laser is taken into account, as described in section 1.7.1.

4.2 Cu Campaign: RIS

The following RIS experiment was conducted at the IGISOL facility at the University of Jyväskylä. In this case ^{63,65}Cu atoms were resonantly excited from their $3d^{10}4s\ ^2S_{1/2}$ ground state by a 244.237nm laser to the excited $3d^9 4s4p\ ^4P^o_{1/2}$ level at 40943.78 cm^{-1}. As a next step, the excited state was again ionized by exciting to an auto-ionizing level $3d^9 4s\ ^3D\ 5s$, at 63584.65 cm^{-1}. The A parameter for the first excitation is $2.03 \cdot 10^6$ Hz. The level scheme is given in figure 4.4. The laser intensities were quoted to be 300mW/cm^2 for the excitation laser and 1.6W/cm^2 for the ionization laser, which leads to respectively 0.03 mJ/cm^2 per pulse and 0.16 mJ/cm^2 per pulse (see table 4.1). Both laser pulses were Gaussian shaped. The details of the laser setup can be found in [18]. In this experiment, several hyperfine scans were taken with various combinations of laser powers and delays between excitation and ionization laser. Therefore, this data set presents an opportunity to compare experimental laser power broadening effects with simulations. More information on the experiment and some other results can be found in appendix B.
An analysis of the experimentally obtained data is shown in figure 4.4. The conclusion which can be drawn from these graphs is that for delayed laser pulses, the power broadening of both lasers, contributing to the Lorentzian width of the resonance, can be decreased significantly compared to the overlapping case. Via the parameters quoted at the beginning of this section, simulations were performed with the goal to study the same Lorentzian linewidth contribution to the spectrum as a function of laser pulse delay. The result is shown in figure 4.4. The

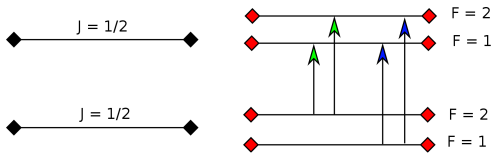

Figure 4.3: *Copper-63,65 level scheme probed in the Jyväskylä experiment at the IGISOL facility explained in section 4.2. Both ^{63}Cu and ^{65}Cu have a spin of $3/2$.*

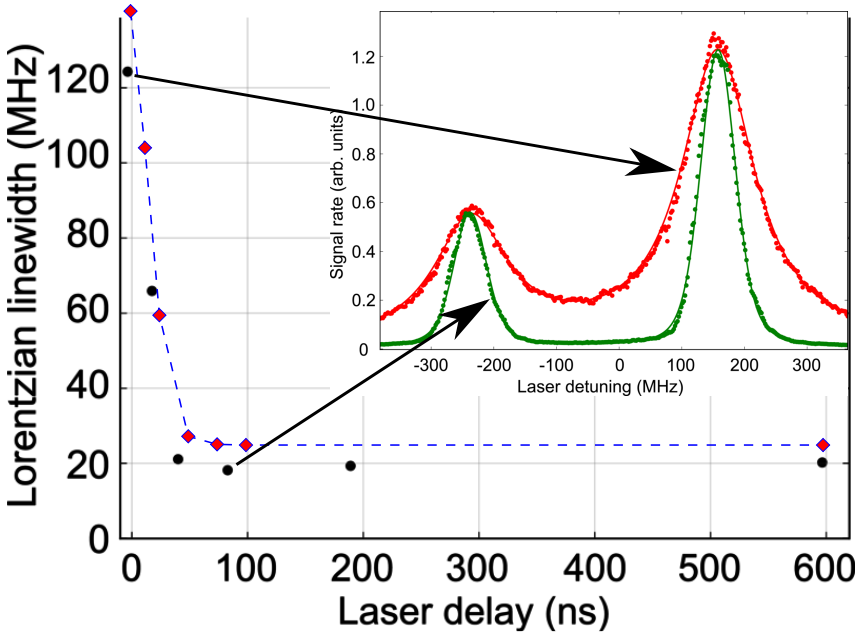

Figure 4.4: *Lorentzian linewidth of Voigt profiles fitting the combined spectra of ^{63}Cu and ^{65}Cu isotopes. Black dots are experimentally obtained values while red diamonds, connected by the dotted line, represent simulation data recovered with the same parameters as in the experiment. The decreasing trend is unmistakably reproduced by the simulations. The offset at large delays can be explained by a slight change in the laser powers or other uncertainties. Comparing to experimental data required rescaling the Lorentzian linewidth from angular frequency to regular frequency space. In the inset, two experimental peaks, with applied fit, corresponding to a resonance from ^{63}Cu and one from ^{65}Cu are shown for 2 different delays. The narrowing of the resonance is clear.*

simulated copper spectra were fitted by Voigt profiles, with the known quantum numbers and hyperfine parameters as the input. Again no efficiency loss is observed when delaying both laser pulses. Clearly model and reality offer close resemblance, reinforcing the belief in the applicability for the model.

As a side note, the $F' = 1$ to $F = 1$ transition shows a clear deviation from the linewidth of the other peaks both in the experimental data and in the simulations. For the $F' = 1$ to $F = 1$ transition, indeed the coupling strength is significantly smaller than for the other transitions, explaining this phenomenon, which is expected from section 3.3. The simulations showing this effect are shown in figure 4.5.

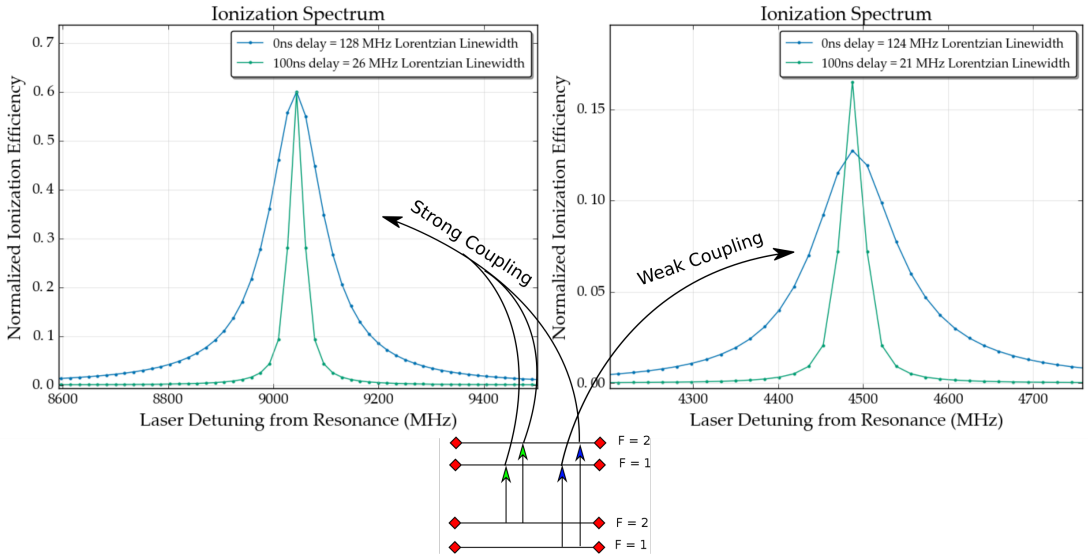

Figure 4.5: *Simulations done on the copper parameters showing the fact that the weakest coupled transition, $F' = 1$ to $F = 1$, results in a smaller linewidth. On the left one of the other resonances is show for comparison*

	^{221}Fr		$^{63-65}$Cu	
I	5/2		3/2	
A(MHz)	2.8		2.0	
	Ground State	Excited State	Ground State	Excited State
J	1/2	3/2	1/2	1/2
L	0	1	0	1
S	1/2	1/2	1/2	1/2
A(MHz)	6210	22.4	5868	2279
B(MHz)	0	-86	0	0
C(MHz)	0	0	0	0
	Excitation Laser	Ionization Laser	Excitation Laser	Ionization Laser
Area (cm^2)	0.5	0.5	0.1	0.1
Laser Intensity (mJ/pulse)	$3 \cdot 10^{-6}$	100	0.03	0.16
Laser Wavelength (nm)	422	1064	244	412
Pulse Time (ns)	50	5	15	15
sigma (b)	0	1	0	1

Table 4.1: *Experimental parameters from section 4.1 and 4.2 used as input for the simulations discussed in this chapter. Most input parameters are self explanatory. The laser pulse time is defined as the standard deviation of the pulse in time.*

4.3 Conclusion

A general conclusion of the simulations part is presented here. In the introduction of chapter 3, the claim was made that $A_<$ transitions could provide clear benefits compared to strong transitions in RIS experiments. Simulations following the model presented in chapter 3, have supported the claim that $A_<$ transitions could be useful for optimizing the resolution as well as the efficiency.

In the work of [1], the advantages of delaying the ionization pulse in a RIS experiment to optimize the resolution were theoretically and experimentally illustrated. The delay between the laser pulses leads to a minimization of the power broadening effect on the lineshapes and to the removal of possible line distortions due to the presence of often high powered ionization lasers. Therefore the experimental precision is improved. This delayed ionization approach has only a significant disadvantage for strong transitions for which the experimental efficiency is drastically reduced due to decay losses. For $A_<$ transitions, this problem is irrelevant as the decay is slow enough to keep the population in the excited level until the ionization laser fires. Therefore, as concluded in [1] and supported by this work, RIS experiments on $A_<$ transitions with delayed laser pulses improve the experimental precision and accuracy without a noticeable decrease in efficiency.
Weak transitions offer further advantages. First of all, there is the inherently smaller linewidth they possess. Secondly, their saturation behavior is more desirable than strong transitions as they reach their respective maximum efficiency at lower powers.
Finally, $A_<$ transitions offer an inherently higher excited state population after sufficiently long excitation pulses, allowing the population to equilibrate. This increase in efficiency for long pulses, which are obtained with chopped cw-lasers, offers competition to the efficiency obtained for higher powers obtained when using pulsed laser systems.

Therefore, as conclusion, weak transitions offer an array of advantages over strong transitions for RIS experiments in optimizing experimental resolution and at the same time maximizing ionization efficiency. The model has been put to a series of tests, in [1] and in this work, proving the applicability of this density matrix approach to real life experiments. The previous claims were backed up by experimental data which could be reproduced with simulations, providing confidence in subsequent predictions by the model. Experimentally exploring the pulse length in chopped cw experiments on weak transitions should therefore be the next step in studying the validity of the model.

Part III

STIRAP

Chapter 5

Theorectical Background

This chapter deals with a relatively recent way of efficiently exciting population from one quantum level to another, called **STI**mulated **R**apid **A**diabatic **P**assage (STIRAP). Its basic characteristics and some extra theoretical features are discussed in this chapter.

5.1 Introduction

Many of experimentally used laser-atom interactions are performed with one general goal: exciting population from one electron quantum level to another. STIRAP achieves this goal by including an additional level into a three-level scheme with the help of two coherent lasers, as shown in figure 5.1. These laser pulses are historically called the Stokes and pump pulse. They couple respectively the additional state with the excited level and the additional state with the ground level. Therefore, now three different ways of achieving population transfer are in general possible, which all try to maximize the population stored in the excited state.

(1) First of all, one can try using monochromatic light from for example a lamp to excite population. This so called incoherent excitation is described by Einstein's rate equations.

(2) Secondly, one can apply a coherent light source to the ensemble of atoms, as for example a laser. The consequences of doing this for continuous irradiation was discussed in chapter 1.

(3) Finally, of which STIRAP is an example, multi-level schemes supported by a number of different coherent radiation sources allow for new pathways to obtain efficient population transfer from the initial towards the final level.

In figure 5.2, the population transfer efficiency of these three methods is presented. Solving the rate equations for a two-level system with continuous incoherent irradiation, (1), reveals a maximum population transfer efficiency of 50 percent for large enough laser intensities. Therefore only half of the initial population of the ground state can be excited to a higher level in this case [19]. For the two-level coherent case, dependent on the strength of spontaneous decay of the levels of interest, respectively Rabi oscillations and damped Rabi oscillations are obtained as a function of time (Rabi oscillations are shown in figure 5.2). Because of the coherence between ground and excited state, the population transfer oscillates with a particular amplitude and frequency dependent on laser intensity and detuning. In experimental practice with atomic levels, 50 percent transfer efficiency is averaged. As can be seen in figure 5.2, the

STIRAP method is able to induce a rapid population transfer between an initial ground state and final state, which can possibly reach a 100 percent effectiveness under circumstances that will be discussed later on.
To conclude this introduction, STIRAP offers a robust, efficient excitation mechanism between two quantum levels with the help of an intermediate state for whose characteristics it is relatively insensitive. The physics behind these properties will be explained in the following theoretical sections.

The STIRAP method is already employed in a variety of physics branches. Applications of this technique can be found in Matter-wave optics, Atomic and Molecular physics (facilitating atom-molecule conversion, preparing photon number states), solid-state physics and quantum information. As an example, a few of these applications can be found in [20], [21], [22] and [23]. Possible explorations of STIRAP in nuclear physics related subjects, will be the main domain of research in the following chapter as the greatly improved excitation efficiency could prove to be beneficial for a variety of methods.

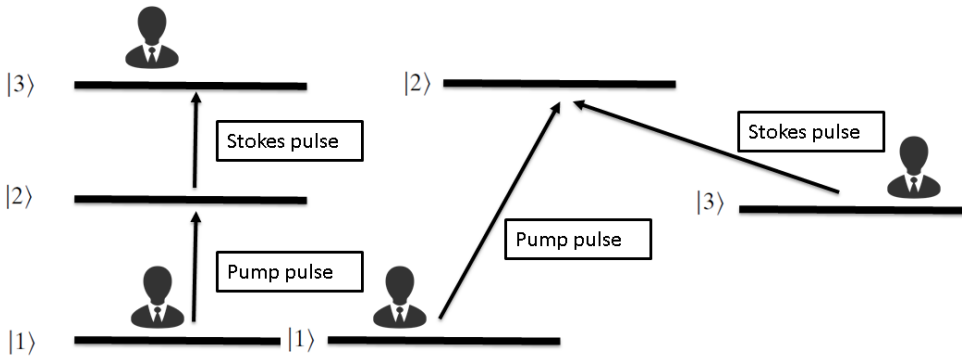

Figure 5.1: *Two possible pathways in which STIRAP can be used. In both cases the pump pulse couples the ground level with an intermediate level and the Stokes pulse does the same with the intermediate level and the final level. Under ideal circumstances a full transfer of population between initial and final level can be achieved. Both cases depicted here are equivalent in the description of STIRAP, therefore the final state could be any excited atomic level or meta stable level in the atom. The left scheme scheme will from here onward be referred to as the ladder-scheme while the right is the Λ-scheme*

5.2 Theory

5.2.1 STIRAP Hamiltonian

From [25], in the simpler case of three naked states without any hyperfine substructure, magnetic splitting or spontaneous decay, the Hamiltonian for a STIRAP process can be obtained (to be compared with the interaction Hamiltonian from chapter 1):

$$H = \hbar/2 \begin{pmatrix} 0 & \Omega_P(t) & 0 \\ \Omega_P(t) & 2\Delta_P & \Omega_S(t) \\ 0 & \Omega_S(t) & 2(\Delta_P - \Delta_S) \end{pmatrix}. \tag{5.1}$$

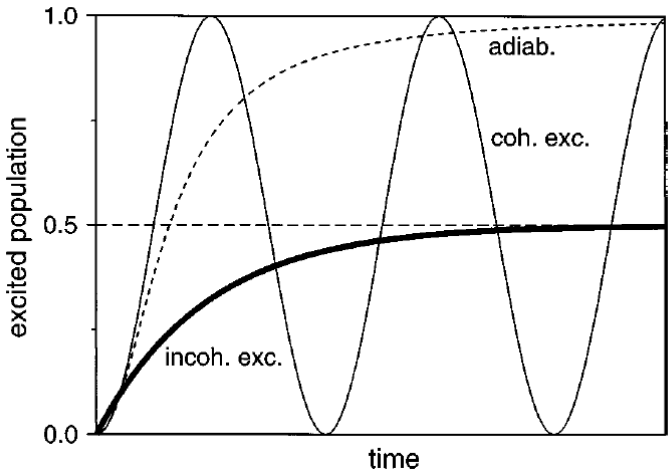

Figure 5.2: *A comparison of the population transfer efficiency as function of time between two levels for the three cases discussed in 5.1. The incoherent line corresponds to (1) in the text while the coherent case and the adiabatic (STIRAP) case correspond respectively to (2) and (3)[24].*

In (5.1), the Ω_P and Ω_S represent the Rabi frequencies or the coupling strength, due to pump and Stokes laser respectively, between the corresponding levels. The laser excitation step in the STIRAP process is exactly the same as the excitation step for a RIS experiment, therefore both can be described by Rabi frequencies which represent the same physical observable as discussed before in section 2.2. Because of the definition for Stokes and pulse lasers, $\Omega_P(t)$ for example represents the coupling between ground level and intermediate state. Δ_P and Δ_S represent respectively the detuning of the pump laser and Stokes laser with respect to the resonance frequency existing between the corresponding two levels.
(5.1) represents thus the Hamiltonian governing the time evolution of a STIRAP process. Simulating such an evolution and paying close attention to the population of all levels will be the topic of many of the following sections. The STIRAP Hamiltonian is clearly time dependent because of the time dependency of both Ω's, which boils down to the fact that the evolution is critically dependent on the temporal properties of the laser pulses. Given the Hamiltonian's time dependence, the adiabatic principle will play an important role in the dynamics of the system.

5.2.2 STIRAP Adiabatic Base

For the sake of simplicity in understanding the STIRAP process, a Hamiltonian closely related to the one in (5.1), with the exception of the fulfillment of double photon resonance (which is the expression that will be used to denote $\Delta_P - \Delta_S = 0$ for the Λ scheme and $\Delta_P + \Delta_S = 0$ for the ladder scheme in the remaining of this thesis), will be discussed. In this case, one can write down the adiabatic base or instantaneous eigenbasis of the time dependent Hamiltonian, which is three dimensional in this case (to be compared with the adiabatic base in 1.2).

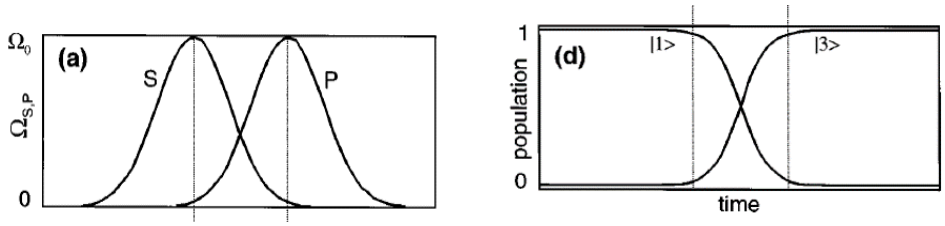

(a) *Temporal behavior of pump and Stokes laser pulse in a STIRAP configuration. The overlap will prove to be essential in causing the characteristic STIRAP population transfer [26].*

(b) *Population transfer between initial and final state in a STIRAP process when laser are fired in counter intuitive manner [26]. Complete inversion of population appears possible.*

Figure 5.3: *A particular way of firing the two lasers in a counterintuitive manner (a) as explained in the text, causes under certain circumstances the rapid adiabatic passage characteristic of STIRAP in (b)*

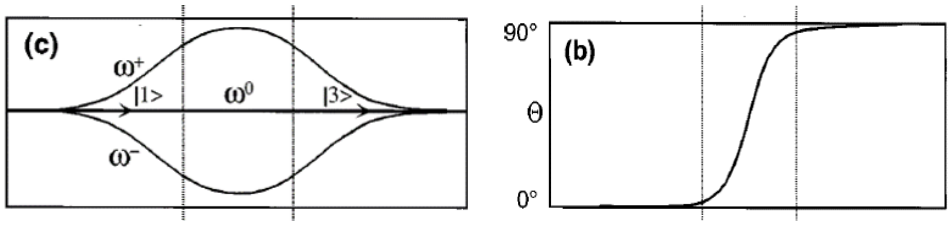

(a) *Temporal behavior of the adiabatic eigenvalues of the Hamiltonian for the case when double photon resonance is satisfied. Important is the large energy splitting at the time of overlap[26].*

(b) *The evolution of the θ parameter, defined in* (5.3)*, essential for the flopping of the adiabatic $|a^0\rangle$ state [26]. Keeping the derivative small while at the same time allowing an evolution from 0° to 90° is vital.*

Figure 5.4: *Together with figure 5.3, the behavior of the eigenvalues and the parameter θ completely describe the STIRAP system at double photon resonance.*

$$|a^+\rangle = \sin(\Theta)\sin(\Phi)|1\rangle + \cos(\Phi)|2\rangle + \cos(\Theta)\sin(\Phi)|3\rangle, \tag{5.2a}$$
$$|a^0\rangle = \cos(\Theta)|1\rangle - \sin(\Theta)|3\rangle, \tag{5.2b}$$
$$|a^-\rangle = \sin(\Theta)\cos(\Phi)|1\rangle - \sin(\Phi)|2\rangle + \cos(\Theta)\cos(\Phi)|3\rangle. \tag{5.2c}$$

In this equation,

$$\tan(\Theta) = \frac{\Omega_P(t)}{\Omega_S(t)}, \tan(2\Phi) = \frac{\Omega_{eff}(t)}{\Delta}. \tag{5.3}$$

Here $\sqrt{\Omega_P^2 + \Omega_S^2} = \Omega_{eff}$ and $\Delta = (\Delta_P + \Delta_S)/2$. The states $|1\rangle, |2\rangle, |3\rangle$ represent the atomic dressed degenerate states (basis of the non-interacting Hamiltonian), with respectively 0,1 or 2 photons added. These eigenstates are no longer an eigenbasis of the Hamiltonian when the system starts interacting with the two lasers.

To understand this population transfer, a close study of the adiabatic states is key. Focusing only on the $|a^0\rangle$ state, two observations can be made. First of all, this state does not have any

overlap with the intermediate state of the atomic base. Secondly one could make $|a^0\rangle$ evolve from state $|1\rangle$ towards $|3\rangle$ during the interaction if Θ is made to go from $0°$ to $90°$ during the time evolution of the system. Because of the fact that the time evolution of Θ is solely dependent on the time evolution of the Rabi frequencies, the temporal pulse sequence will be essential. Firing the pulses in exactly the way as depicted in part (a) of figure 5.3, causes this $0° - 90°$ evolution of Θ. This pulse sequence therefore drives the $|a^0\rangle$ adiabatic state from the initial atomic state to the final atomic state without interference from the intermediate state. The pulse sequence itself is called counter-intuitive because the Stokes laser is fired before the pump laser. This Stokes laser therefore couples two quantum states that are not populated at the beginning of the interaction. The overlap between both pulses will thus be vital to the population transfer. Using continuous lasers, firing them perpendicular to a particle beam with the primary axis of both lasers displaced by a certain amount, reduces to the required pulse sequence.
If the $|a^0\rangle$ adiabatic state would be the state vector of the system at all times, the complete 100 percent population transfer of a STIRAP process is explained. At time $t = 0$, at the beginning of the evolution, when no lasers are interacting with the system, Θ is zero and the $|a^0\rangle$ state equals to the initial atomic ground state. At this moment $|a^0\rangle$ represents a complete description of the system. Because this state is a member of the adiabatic instantaneous eigenbasis of the Hamiltonian, the system will follow this state under the adiabatic following conditions. Therefore if adiabatic evolution is guaranteed, the system will follow the $|a^0\rangle$ state and full population transfer will be possible, as shown in part (b) of figure 5.3. This full population transfer is translated in 100 percent certainty of finding the population in the final state.

5.3 STIRAP Adiabatic Evolution

As explained in section 5.2.2, the adiabatic evolution of the system is crucial for the existence of a 100 percent efficient population transfer pathway between two quantum states. As explained before in section 1.6, the essential factors defining the adiabaticity of the evolution are the off-diagonal terms in the STIRAP Hamiltonian, written down in the adiabatic basis:

$$H_{ad} \sim \begin{pmatrix} \Omega_{eff}\cot(\Phi) & i\dot{\Theta}\sin(\Phi) & i\dot{\Phi} \\ -i\dot{\Theta}\sin(\Phi) & 0 & -i\dot{\Theta}\cos(\Phi) \\ -i\dot{\Phi}+ & i\dot{\Theta}\cos(\Phi) & \Omega_{eff}\tan(\Phi) \end{pmatrix}. \tag{5.4}$$

Via theoretical arguments [4], the off-diagonal elements of interest ($\langle a^{\pm}|H|a^0\rangle$), which evolve like $\dot{\theta}$ must be small compared to the splitting of the adiabatic energies to make the coupling between the adiabatic states as small as possible. In this case, the adiabatic states are closely resembling constants of motion. The mathematical description of this statement is as follows (first in general for states $|a_k\rangle$ from [27]):

$$\sum_{k\neq 1} \frac{|\langle a_k|\dot{a_0}\rangle|^2_{max}}{|\omega_k - \omega_0 + \dot{\theta_{0k}}|^2_{min}} \ll 1. \tag{5.5}$$

For the specific case here:

$$\langle a^{\pm}|H_{STIRAP}|a^0\rangle \sim \langle a^{\pm}|\dot{a}^0\rangle \ll |\omega^{\pm} - \omega^0|. \tag{5.6}$$

Where $\omega^{+,-,0}$ represent the eigenvalues corresponding to the adiabatic eigenstates. Via the Hamiltonian (5.1) written down in the adiabatic eigenbasis, one obtains $\langle a^{\pm}|\dot{a}^0\rangle = -\dot{\Theta}\sin(\Phi)$.

Therefore the adiabaticity condition translates into:

$$\dot{\Theta} \ll |\omega^{\pm} - \omega^{0}|. \tag{5.7}$$

For adiabatic evolution to occur this inequality must be fulfilled at all times during the evolution, it is therefore a local condition. To make this requirement more tractable, a global condition can be defined. This global condition reduces $\dot{\Theta}$ to its time averaged form $\langle\dot{\Theta}\rangle = \frac{\pi}{2\Delta t}$. In this time averaged form, Δt represents the time of overlap between the two laser pulses. To accommodate the adiabatic condition, this should be a lot smaller than $|\omega^{\pm} - \omega^{0}|$, which is defined as Ω_{eff}. Bringing these together, the global adiabatic condition is:

$$\Omega_{eff}\Delta t > 10. \tag{5.8}$$

The 10 in this equation has been obtained via experimental data. It has been seen that any delay between one and one and a half times the HWHM of the laser pulse in time is sufficient for efficient population transfer. The amount of overlap between the two laser pulses is thus important when considering adiabatic evolution. In addition to this, important parameters to keep a close eye on, are the eigenvalues of the Hamiltonian. On the double photon resonance line, the eigenvalues are the energy expectation values of the adiabatic states: $\langle a^{+,-,0}|H|a^{+,-,0}\rangle$. The time evolution of these eigenvalues was presented in figure 5.4. This graphical representation helps to understand the adiabatical evolution. One can see that at the point of maximal $\dot{\Theta}$, the LHS of the adiabatic condition (5.7), the eigenvalue energy splitting is also maximal, therefore enhancing as much as possible the adiabatic condition.

The influence of the laser power comes down to the statement: 'the more power the better'. This statement is strengthened by the fact that the above global condition for adiabatic following only applies for laser pulses with a transform-limited bandwidth. Most pulsed lasers have however inferior coherence properties and for those the adiabatic condition equation should be adapted to [25].

$$\Omega_{eff}^{2}\Delta t > \frac{100}{\Delta t}\left\{1 + \left(\frac{\Delta\omega_{L}}{\Delta\omega_{TL}}\right)^{2}\right\}\Gamma. \tag{5.9}$$

The last term in this equation corresponds to the ratio of the actual bandwidth compared with the transform-limited bandwidth. Γ is a factor taking into account the pulse shape and is of the order of unity. This equation represents the fact that to compensate large incoherences, more power is needed.
To conclude, if adiabatic conditions are fulfilled, and all external conditions are as discussed in 5.2.2, the $|a_0\rangle$ adiabatic state will overlap completely with the state vector describing the system during the interaction. Therefore full 100 percent efficient population transfer is possible due to the transformation of the $|a_0\rangle$ state from $|1\rangle$ to $|3\rangle$.

5.4 Intuitive Pulse Sequence

To present a complete picture of the STIRAP process, the population transfer pathway for the intuitive pulse sequence is compared to the counter-intuitive way following some remarks raised by [28].

For the intuitive laser pulse sequence, the pump laser precedes the Stokes laser with some overlap between the two, similar as in the STIRAP sequence but with Stokes and pump laser interchanged in time. In this case, Θ evolves from $90°$ to $0°$ and two different possibilities exist (the double resonance postulation is still assumed).
First of all, when $\Delta_P \neq 0$, the adiabatic evolution will follow the $|a^-\rangle$ adiabatic state which emerges as the $|3\rangle$ state after starting from the atomic ground state. This situation is of course very similar to the counter-intuitive one, described above, where the state vector, complying to adiabatic conditions, followed the same evolution. However, as one can see from (5.2c), this $|a^-\rangle$ state has some overlap with the intermediate level, which was absent in the STIRAP description.
For $\Delta_P = 0$, $\Phi = \pi/4$, and therefore both the $|a^-\rangle$ and the $|a^+\rangle$ states are populated before interaction. The population evolution now involves oscillatory transfers to and from the final state and the intermediate state. In this case, efficient transfer of population is likely to fail.
Therefore as a conclusion, it can be asserted that the intuitive laser pulse sequence also allows for efficient population transfer in the adiabatic limit for detunings from single photon resonance. Two remarks should be made accompanying this statement however. First of all, the adiabatic $|a^-\rangle$ state followed by the state vector when applying the intuitive pulse sequence, has some overlap with the intermediate state. Strong decay from this intermediate state will therefore reduce the transfer efficiency significantly. Secondly, the adiabatic regime, determining the efficiency, is more difficult to achieve for intuitive pulse sequences than for their counter-intuitive counterpart as explained in more detail in [28].

5.5 Summary

To conclude the theoretical basis of a STIRAP process and to prepare for some additions to this basis, a short summary of a STIRAP evolution is described. Before any laser interacts with the atom, the system is in the atomic ground state which is equal to the $|a^0\rangle$ adiabatic state. When the system starts interacting with the lasers, the atomic states are no longer eigenstates of the Hamiltonian and one should follow the adiabatic states, which are the instantaneous eigenstates of the interacting system. For a time-independent Hamiltonian, the system would stay in $|a^0\rangle$ forever when it has started there. Because in the STIRAP case, the Hamiltonian is time dependent, the adiabatic theorem states that one can make the same conclusion if only the coupling between the adiabatic states during the evolution stays small. Satisfying this adiabatic condition, the state vector of the system remains equal to $|a^0\rangle$ during the evolution. Having the pulse sequence as depicted in figure 5.3, the $|a^0\rangle$ state will then evolve from the atomic ground state to an atomic excited state without any influence from the intermediate state. In the ideal case, this results in a 100 percent efficient population transfer.

5.6 Theoretical Extras

As seen in the previous section, STIRAP offers the possibility to efficiently excite population from one quantum level to another. This efficient transfer of population is not the only characteristic of a STIRAP process. For example, because two photons are used, a normally forbidden transition can be used for excitation from one level to another. Other properties of a STIRAP process will be shortly discussed in following sections. These characteristics, next to

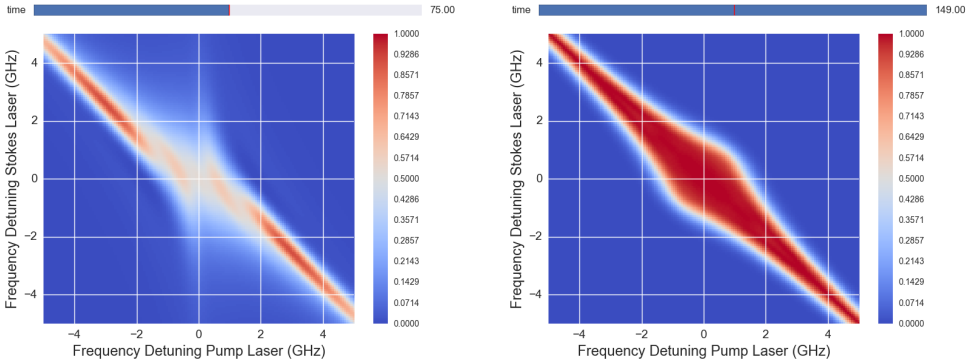

(a) *Frequency dependent excited state population at the central time when both laser partially overlap.*

(b) *Frequency dependent excited state population at the final time when the STIRAP process is completed.*

Figure 5.5: *STIRAP signature, displayed as the population of the final state as a function of both laser frequencies. The color code shows the efficient region. Clearly the diagonal for which double photon resonance is fulfilled forms the foundations of this structure.*

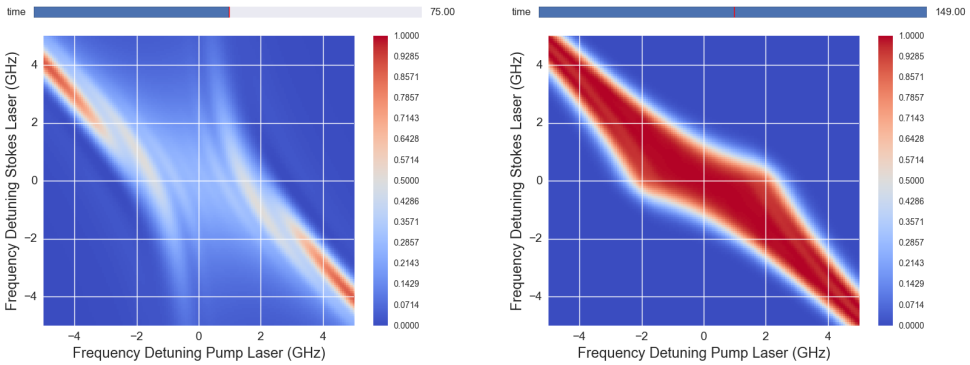

(a) *Frequency dependent excited state population at the central time when both laser overlap.*

(b) *Frequency dependent excited state population at the final time when the STIRAP process is completed.*

Figure 5.6: *STIRAP signature, displayed as the population of the metastable or top excited state as a function of both laser frequencies for a different coupling strength of both transitions.*

the explanation of the STIRAP signature, figure 5.5, are required to understand the possible applications in the following chapter.

5.6.1 Frequency Robustness

The discussion in section 5.2 applied to the case where double photon resonance was fulfilled. This means that efficient transfer is still possible for large detunings from single photon resonances for both pump and Stokes transitions. Ultimately the transfer efficiency will die out because the transition strengths will have dropped significantly, reducing the validity of the adiabatic criterion [29]. To observe what happens to the transfer efficiency beyond this double photon resonance line, which is represented by the efficient diagonal in figure 5.5, a very similar theoretical derivation as in section 5.2 can be done but with more complex algebraic expressions. The complete description can be found in [30].
A brief summary of the results is presented here to understand the efficiency structure shown in figure 5.5. Following the adiabatic condition (5.6), both the coupling factors in the adiabatic base and the difference of the eigenvalues should be considered. Moving away from the double photon line puts more and more stress on (5.6), explaining the decreasing efficiency. However, this process is dependent on the ratio of the Rabi frequencies. As seen in figure 5.6, a ratio (Ω_P/Ω_S) different from one can induce strong asymmetric behavior of the STIRAP signature. This asymmetry could prove to be useful in the applications. More information can be found in [29] and [30], with some useful tools in [31], [32] and [33].

5.6.2 Spontaneous Decay

The spontaneous decay process should be added to the description of STIRAP when a feasibility study is to be made for experimental purposes concerning atomic levels. As stated before, the excitation process presented by STIRAP also offers a relatively large insensitivity with respect to the decay of the intermediate state. Here a difference between the Λ and ladder-scheme reveals itself. The Λ-scheme will move the ground state population to a metastable state. In this case only the decay from the intermediate state has to be taken into account. In the case of the ladder-scheme, also decay from the final state should be considered.
Decay to and from states in the reduced Hilbert space, can be described by a Lindblad term as in equation 2.2. Decay to states outside the system can be included by adding imaginary terms $(i\Gamma)$ to the particular diagonal elements in the Hamiltonian 5.1. These terms will induce population loss with a rate Γ. This addition of imaginary terms will be discussed when considering the STIRAP process to an auto-ionization state. The addition of the Lindblad term to the equations of motion induces changes in the STIRAP process due to the incoherences it brings. The influence of this term on the STIRAP population transfer efficiency is described for example in [34]. Here, we present their conclusion for a Λ scheme considering thus only the decay of the intermediate state towards the initial and final level.
The STIRAP process remains largely unaffected by spontaneous decay for small to intermediate decay rates (compared to the peak Rabi frequency and depending on which decay branch is the strongest). In the adiabatic limit the intermediate state will not be populated, explaining the robustness of STIRAP in this case. Non adiabatic couplings have to be taken into account to accommodate the spontaneous emission effect from the intermediate state. For small to normal decay rates, no significant decrease in STIRAP's efficiency can be determined. For intermediate to strong decay rates, the optical pumping process becomes indistinguishable from the STIRAP

process. For very strong decay rates however, the quantum overdamping effect comes into play destroying any sort of population transfer from the ground state. This quantum overdamping effect was already encountered in section 3.5 when dealing with large ionization laser powers which decreased the excitation efficiency markedly. These statements are all again dependent on which decay branch of the intermediate level is the leading decay pathway. Stronger decay towards the final state than to the ground state is helpful for the STIRAP process while the opposite reduces the efficiency. The relative insensitivity to spontaneous decay for common decay rates, makes that the STIRAP process has been verified experimentally in many cases.

5.6.3 Continuum Structure

The intermediate state in a STIRAP process does not have to be a discrete bound quantum level. Theoretically as well as experimentally obtained results show that STIRAP is for example still possible when the final state has the same level structure as in the continuum. In this case multiple situations are possible. Considering first a two-level scheme being probed in a two-step ionization process. Firing the ionization laser first could induce an increase in the ionization efficiency compared to a normal laser excitation-ionization experiment. Therefore a STIRAP process with the initial and intermediate state being discrete quantum states and the final state lying in the continuum possesses enough coherence to enhance ionization rates. This ionization rate can be further enlarged by embedding a discrete-like state in the continuum with the use of a third laser. Examples can be found in [35], [36] and [37].

Chapter 6

Applications

In this chapter a few possible applications of the STIRAP technique in nuclear physics methods are examined. Using the theory of chapter 5 and simulations on the model of chapter 1, the feasibility of introducing STIRAP into a few existing techniques is studied. Recall that all quoted frequencies are in angular frequency space unless stated otherwise.

6.1 Introduction

As an introduction, three possible applications of STIRAP will be named.
First of all, STIRAP could be envisioned as way to probe the hyperfine structure. It could maybe even enlarge the efficiency of the RIS experiments, discussed before. Secondly, STIRAP could be used as a tool to efficiently ionize an ensemble via the use of an auto-ionizing state. In addition to this, the Λ-scheme STIRAP could be used for e.g. preparation of radioactive beams into metastable states. This is currently done using optical pumping methods. For these optical pumping procedures however, closed quantum systems are required with constraints on the spontaneous decay pathway characteristics of the quantum levels. On top of this a long interaction time between atoms and photons is needed to optimize population transfer. In the case of STIRAP, a similar setup could maintain the same efficiency or even better, but in a much shorter time and in a much less sensitive (to atomic state characteristics) way. Potentially, this could even be applied to Doppler-broadened ensembles. Many other potential applications could of course exist.

To be able to simulate the STIRAP procedure, the model of chapters 1 and 2 was adapted to include a third quantum level, without ionization. Simulations on the three-level system were therefore possible with the potential inclusion of substructure. Following this, to visualize the complex dynamics of the STIRAP process, a visualization tool was written in python. An example is shown in figure 6.1. Using this, the population as a function of time for each level can be studied while the dynamics of the adiabatic energy values, the eigenvalues of the system, the eigenvectors, etc. can be monitored on the other graphs. These tools have helped greatly in understanding and checking theoretical predictions. The simulation code was again supported by a similar graphical user interface as 3.1, adapted to a three-level scheme.

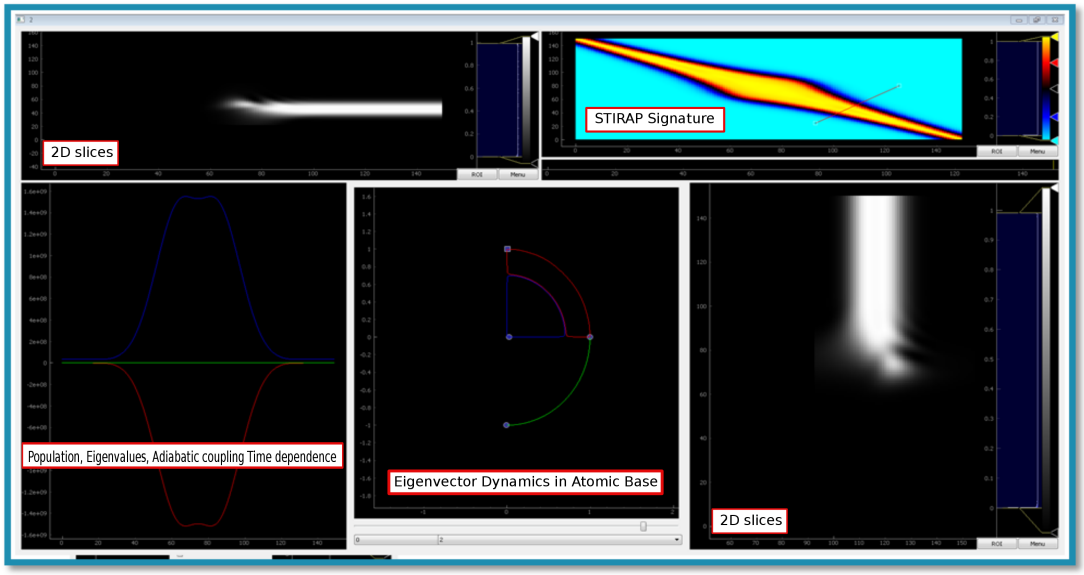

Figure 6.1: *A visualization of the STIRAP procedure in its entirety. To clarify the different figures, titles are added. So is the population of a level of choice studied by the top right graph as a function of both laser frequencies via a time slider, which visualizes the third dimension and two 2D-slices presented in the top left and bottom right part. The time dependence of the population, adiabatic energy values, eigenvalues, adiabatic coupling factors are available in the bottom left graph, while the dynamics of the eigenvectors is visible by the presentation of their projection on the atomic base vectors in the middle figure at the bottom. Understanding all aspects of the STIRAP process is vital for the determination of the applicability for experiments.*

6.2 STIRAP and Multilevel Systems

6.2.1 Hyperfine Structure Probe

As a first application, the feasibility of using STIRAP as a probe for the hyperfine structure, was studied. The goal is to obtain hyperfine parameters while taking advantage of the superior population transfer efficiency of STIRAP.
As a start, stated in section 5.6.3, using a reversed pulse order could already have a significant effect on the obtained efficiency. Via this pulse scheme, the ionization efficiency could be enhanced depending on the amount of stress put on the intuitive-sequence adiabatic pathway. However as was seen in experiment and confirmed by theory and simulations (see also [36]), the STIRAP method results in broad lineshapes. An example is shown in figure 6.2. For high resolution laser spectroscopy studies, STIRAP is therefore not immediately useful. In addition to this, in the normal RIS pulse sequence, as was argued in chapter 1, weak transitions should be sought for. For the STIRAP pulse sequence however, strong transitions should be used to simplify the adiabatic condition and therefore increase ionization efficiency. However, as discussed in chapter 1, $A_{>}$ transitions have other limitations.

Generally, the inclusion of the hyperfine structure also introduces a multilevel configuration to the STIRAP method. An introduction to this can be found in [38] and [39], which discuss the

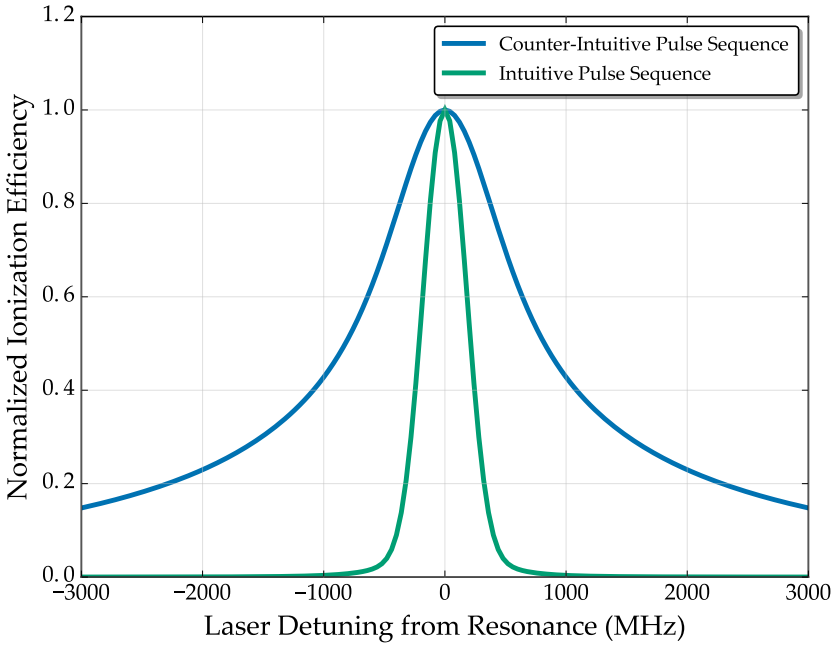

Figure 6.2: *Two simulations of a ionization spectrum following an excitation-ionization scheme for a STIRAP pulse sequence and a normal pulse sequence. In this case, roughly similar ionization efficiency was obtained, showing clearly that the atomic parameters were such that the intuitive pulse sequence was not detrimental to the outcome (see section 5.4).*

role of magnetic substates. First of all, one has to make sure that the presence of an extra state besides the normal three-state STIRAP scheme doesn't influence the adiabatic following criterion.

To start, consider the effect of the inclusion of an extra final level which is separated from the other by an energy gap of ϵ. In this case, two out of four eigenvectors of the system are degenerate with eigenvalue 0. If one of the eigenstates in the degenerate eigenbasis is designed as the familiar dark state of a STIRAP process, the other is completely defined. Now, due to their degeneracy, the fulfilment of the adiabatic condition is not assured. (5.6) is evaluated considering the coupling factor in the adiabatic Hamiltonian between the two degenerate eigenstates for Gaussian pulses of length τ. In the case of double photon resonance with one of the final states, according to [27], the adiabatic condition becomes, after cumbersome algebra (the standard deviation in time of the laser pulses is taken to be 10ns):

$$\epsilon \gg \frac{0.94}{\tau}. \tag{6.1}$$

Following condition (6.1), the conclusion can be made that the usual STIRAP dark state can be followed throughout the interaction without any significant coupling to the other degenerate state, by sustaining the Fourier limited bandwidth of the laser at least an order of magnitude larger than the energy splitting between the two final levels. [27] delivers the quantitative statement that STIRAP will continue to work in the case of a high density of final states if the density does not surpass one level every 14MHz. To obtain this value, both transitions are assumed equally strong. In this case the quantum levels do not interfere, and forcing a double photon resonance between one initial and one final state can deliver a population transfer of 100 percent. The case of multiple initial levels is entirely analogous. Concerning the study

of the hyperfine structure via STIRAP, this translates into the fact that for strongly collapsed level structures, the unique STIRAP population transfer will not succeed.
As a next case, two intermediate levels can be studied. An example of a simulation for a 1-2-1 level scheme, is shown in figure 6.3. A distinctive loss in efficiency is noticed when tuning the laser frequencies in between the two intermediate levels. This could perhaps be explained by looking again at two eigenvectors which are degenerate with energy 0. These eigenvectors ($|a_{0,1}\rangle$ and $|a_{0,2}\rangle$) are given by (for equal transition strengths Ω, intermediate level splitting 2δ and intermediate level tuning of the laser, without normalization factors):

$$\begin{aligned} |a_{0,1}\rangle &= \frac{\delta}{\Omega}|1\rangle - |2\rangle + |3\rangle, \\ |a_{0,2}\rangle &= -|1\rangle + |4\rangle. \end{aligned} \tag{6.2}$$

$|a_{0,1}\rangle$ and $|a_{0,2}\rangle$ are thus coupled by a factor which is dependent on the ratio between the splitting of the intermediate levels and the coupling strength. Therefore dependent on the ratio $\frac{\delta}{\Omega}$, strong coupling between the degenerate eigenvectors could occur at intermediate tuning between the STIRAP dark state and the other degenerate state, thus destabilizing the STIRAP procedure at those intermediate frequencies. However the 100 percent efficient population transfer between initial and final state levels are perfectly possible when tuning the lasers close to double photon resonance and close to one of the intermediate levels as was the case for multiple final levels. Here however, a difference with the previous discussion is stated in [27]. There is not an immediate limit on the density of states which could allow a STIRAP process. This fact is supported by observations and analytic calculations which allow for a STIRAP procedure with the intermediate state in a continuum of states ($\delta \ll \Omega$).

To summarize the possible difficulties which could be encountered when applying STIRAP on multilevel systems, [39] and [38] propose following checks to be considered

- When the pump pulse is absent, one adiabatic state should coincide with the atomic ground state. This adiabatic state will hopefully become the STIRAP dark state.
- The adiabatic theorem should be fulfilled for the entirety of the interaction. Multilevel systems cause an increasingly complex interplay between adiabatic eigenvalues which could render a clean STIRAP transfer impossible due to level crossings.
- The dark state should evolve during the interaction from the initial ground state to the final one.
- The dark state should have as little overlap as possible with any other adiabatic states, this to reduce any non-adiabatic evolution, destroying perfect population transfer.

An example of applying the STIRAP signature to a multilevel scheme is shown in figure 6.4 for a realistic 2-2-4 level-scheme. In figure 6.4 regions of high and low transfer efficiency are found in what is an all in all seemingly unstructured graph. These kind of examples show that hyperfine analysis using any kind of laser scan will be enormously difficult to analyze. However, each combination of levels could be returned to a simple three-level STIRAP scheme if the density of states is not too high. Optimizing on each separate three-level scheme and doing a two-laser scan could be possible to extract the hyperfine parameters with still the increased spectral linewidth as drawback to be considered.

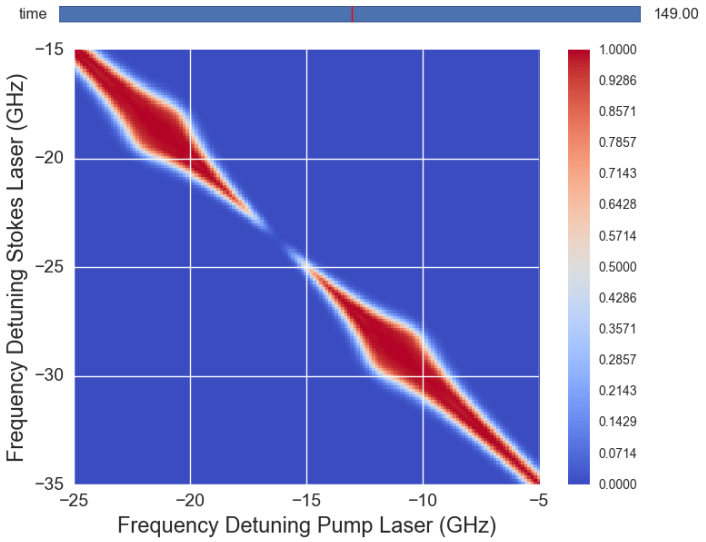

Figure 6.3: *A visualization of the STIRAP procedure for a 1-2-1 level scheme. A distinct loss in efficiency is noticed when the laser frequencies are tuned in between the two intermediate levels.*

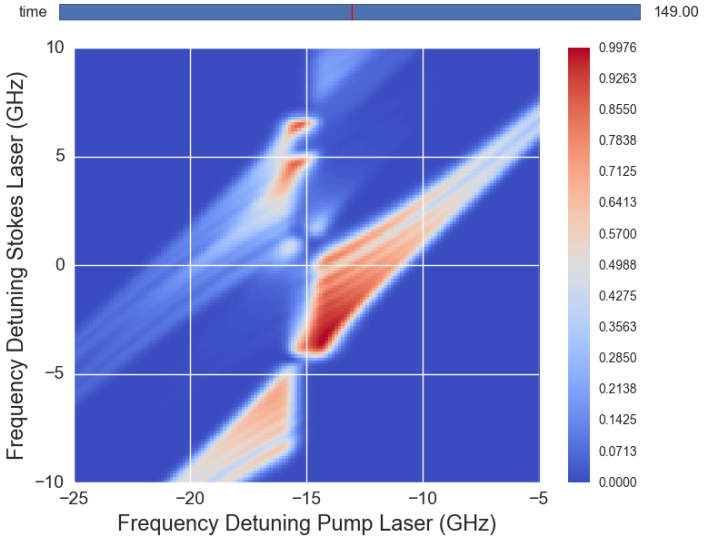

Figure 6.4: *A visualization of the STIRAP procedure for a 2-2-4 level scheme. The population transfer dependence for all final levels is shown. The increasingly difficult structure makes hyperfine analysis difficult.*

6.2.2 Conclusion

As a conclusion, the use of the STIRAP pulse sequence for obtaining hyperfine parameters suffers from some drawbacks and its immediate application in determining these nuclear parameters in any way better than existing methods is in question. The drawbacks situate mainly in two areas.

First of all, although the excitation efficiency in a stirap process can be 100 percent, the spectral linewidths will increase by a significant amount compared to normal RIS schemes while the required substantial laser power making STIRAP possible is difficult to reconcile with high spectral precision. Therefore, applying STIRAP for high precision hyperfine studies is not rec-

ommended.
Secondly dealing with hyperfine structures, means applying the STIRAP procedure to multilevel systems. This transfer from a three-level scheme to an arbitrary number of states is not trivial by any means. As discussed in previous sections, the density of states for initial and final levels may not be too high while the density for the intermediate level has less of an influence on the population transfer efficiency. On top of this, an increasingly difficult interplay between the adiabatic eigenvalues occurs, possibly destroying the adiabatic pathway. At the same time, the coupling strengths have their influence on the STIRAP signature. One can imagine now that when realistic level structures are studied, increasingly more difficult signatures are obtained as a function of laser frequency, rendering the analysis near impossible.

6.3 STIRAP vs Optical Pumping

6.3.1 Introduction

As a next application, the replacement of the optical pumping scheme by a STIRAP procedure is considered. An introduction to and a more complex application of the optical pumping method can be found in chapter six of [40].
In its simplest form, optical pumping will be performed on a Λ-scheme as shown in figure 5.1, with only the pump laser interacting with the system. The pump laser, which is continuous wave, will populate the intermediate state. By spontaneous decay, population is transferred then to the meta-stable state. Of course, the intermediate state can decay into many other pathways, reducing the optical pumping efficiency. Among those pathways are: decay back to the ground state, decay back to a another level in the ground state hyperfine multiplet, decay towards a state outside the system,... Therefore optical pumping is strongly dependent on the interaction time between the lasers and the characteristics of the atomic level scheme. Many cycles of excitation and decay should be allowed before efficient transfer is possible. Specifically, for hyperfine parameter studies, optical pumping is used for example if an atomic meta-stable state is more interesting from a physics point of view (larger energy splitting due to the hyperfine interaction for example). Optical pumping is also often used to create polarized beams by pumping all population to a particular $|m_F, F\rangle$ state.
This Λ-scheme resembles in many ways the scheme in figure 5.1 on which a STIRAP pulse sequence can be applied. Therefore, the following section will examine the possible use of STIRAP as a replacement of the optical pumping scheme. The goal is thus to excite as efficiently as possible population to the meta-stable state in a much shorter interaction region than is possible via optical pumping, plus with a much smaller sensitivity to the decay pathways of the intermediate state.
Thus, in this work, two cases will be compared with one another on the basis of their population transfer efficiency (see figure 6.5). The first is the optical pumping procedure which demands long interaction times and a collinear beam-laser geometry to reduce as much as possible the Doppler effect. Secondly, the STIRAP alternative for optical pumping is shown, presenting a much smaller setup with cross-beam laser geometry, allowing the atoms to see a counter-intuitive pulse-like laser beam. The possible use of continuous wave lasers offers another advantage in their inherently superior coherence characteristics reducing the adiabatic requirements. In cross-beam geometry, the Doppler effect cannot be ignored, which is the subject of the next section.

Three cases are then considered in which the optical pumping procedure is compared to STIRAP efficiency. The simplified level scheme of these three cases is shown in figure 6.6. The goal is to investigate whether the population of the meta-stable state can reach comparable values via the STIRAP procedure as via optical pumping. In the case this is feasible, which means that the power densities required for STIRAP's adiabatic pathway are reasonable, the long interaction region needed for optical pumping methods could be reduced significantly. The three cases boil down to the study of a spin 0 system (closed three-level scheme), a spin $1/2$ system (with J=$1/2$, this causes two sublevels for each state) and a level scheme for which the intermediate level not only decays back to the ground state and the meta-stable state but also towards some other quantum states outside the system. Other quantum numbers are fixed for all systems.
As a side note, stimulated Emission Pumping (SEP) could be done by returning to the intuitive pulse sequence, pump pulse before Stokes pulse or overlapping both, but this efficiency is often improved by STIRAP with a factor of three or more.

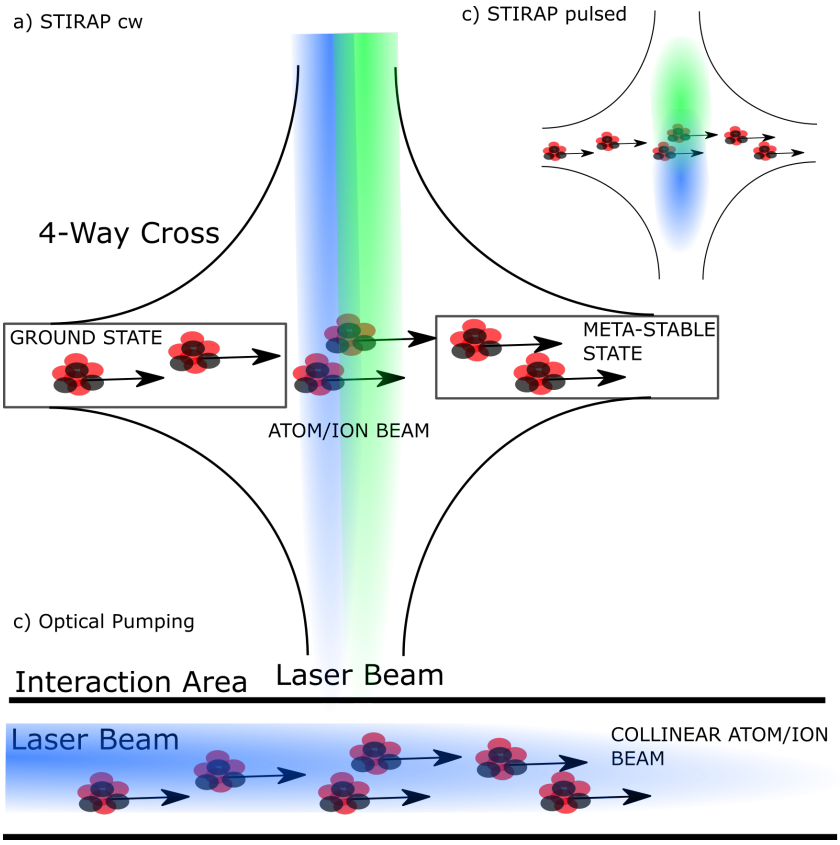

Figure 6.5: *Pictorial representation of the practical use of the STIRAP method (a) with cw-radiation or pulsed lasers (b) and its optical pumping counterpart (c). In the STIRAP optical pumping equivalent, the atoms will see the perpendicularly propagating continuous laser beams as pulses.*

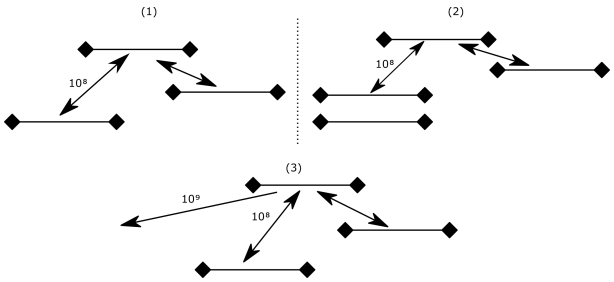

Figure 6.6: *The level schemes of the three cases for which optical pumping is compared to STIRAP. (1) is the spin O case, (2) is spin $1/2$ and (3) has the included extra loss factor.*

6.3.2 Optical Pumping

The above mentioned three cases are simulated via a validated code for optical pumping via the use of rate equation based simulations, [41] with extra implementations from Wouter Gins (PhD student at IKS, KU Leuven). The laser power was chosen to be 8W/m^2, which is an experimentally easily accessible intensity. As a check, simulations with the model considered in this thesis were done on similar systems. The code designed to simulate STIRAP procedures was therefore used with the Stokes laser intensity reduced to zero, for long interaction times. These simulations based on the density matrix formalism showed roughly similar population transfer efficiency as the simulations based on the rate equations. This is expected as the density matrix formalism converges to the rate equations for high decoherence rates or long interaction times.
For every case, the total population in the meta stable state is considered for three different interaction times and four different A parameters of the Stokes transition. The A parameter of the pump transition is fixed to 10^8s^{-1}. The results are shown in figures 6.7 and 6.8. For all three cases, a distinct increase in the efficiency occurs for increasing A parameter of the Stokes transition. Increasing this A parameter allows for faster spontaneous decay from the intermediate state towards the meta-stable state, just what is needed for faster optical pumping. Going from the results of the $I = 0$ case to those of the $I = \frac{1}{2}$ system or the lossy case, the efficiency decreases again because of the fact that more decay pathways open up which are not directed towards the meta-stable state. In the former the level scheme results in two hyperfine levels for the ground state, which is less ideal because one of them is a dark state. The overall efficiency will therefore decrease more for longer interaction times.
To compare this classical optical pumping method with STIRAP, some physical characteristics of typical experiments are useful. Assuming one works with an element of mass 50u with energy 50keV, the interaction length required to obtain $0.5 - 5 - 50$ μs of interaction time is respectively $\simeq 0.2 - 2 - 20$ m. From the simulation it is clear that appreciable efficiency requires $>$ m interaction length (considering more powerful pumping lasers, this is reduced by some amount towards $\simeq$ m). Therefore the optical pumping setup will present constraints on the physical dimensions of the experimental setup.

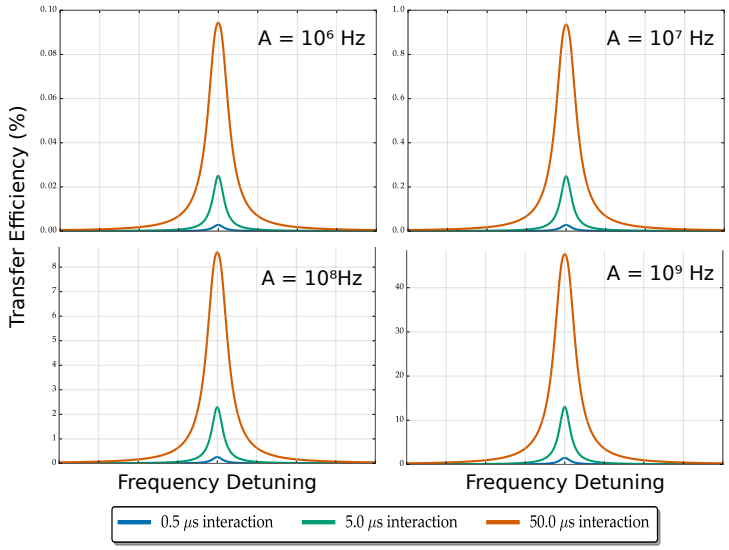

(a) $I = 0$

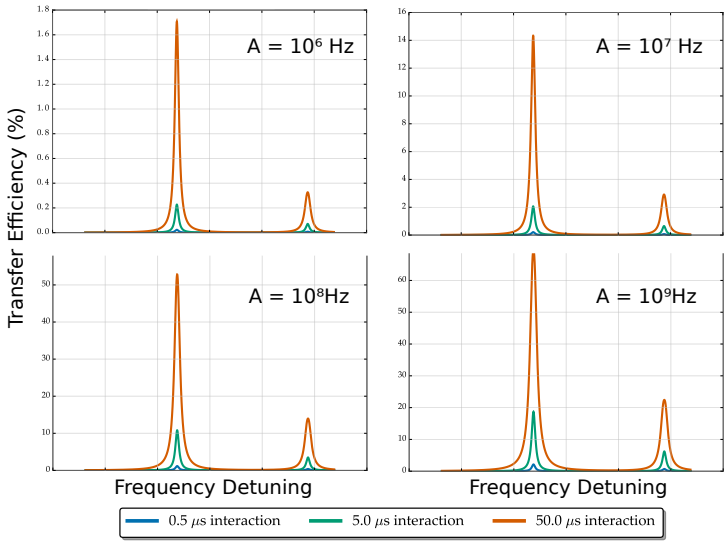

(b) $I = \frac{1}{2}$

Figure 6.7: *Simulated optical pumping efficiency for a $I = 0$ and $I = \frac{1}{2}$ Λ-scheme. The Einstein A parameter is for both cases equal to 10^8 for the pump transition while the A parameter for the the decay to the meta-stable state is shown on the figure. The cw laser intensity used in these simulations offer around 8W/m^2.*

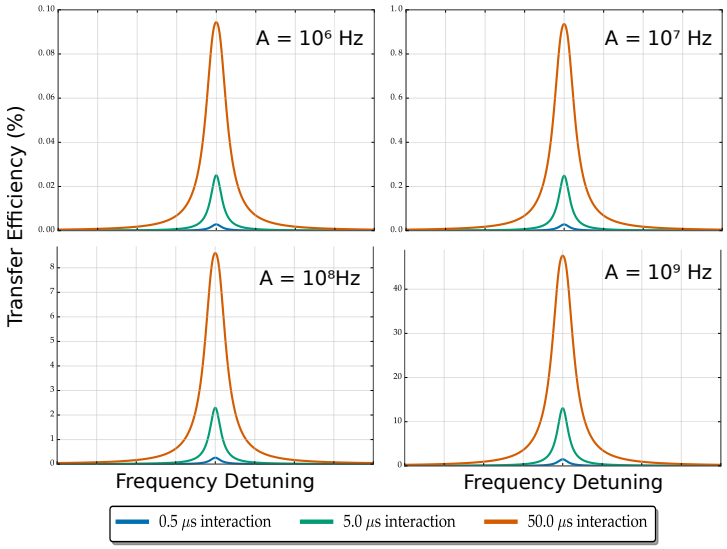

Figure 6.8: *Simulated optical pumping efficiency for a $I = 0$ Λ-scheme with an extra loss term added to the intermediate state. The total loss rate and the A parameter for the pump transition are respectively 10^9 and 10^8, while the A parameter for the decay to the meta-stable state is shown on the figure. This figure should be compared to figure 6.7. The cw laser intensity used in these simulations offer around 8W/m^2.*

6.3.3 STIRAP

Via the rate equations or the similar simulations on the density matrix formalism, the typical optical pumping efficiency for the above mentioned three cases is known. For each of the three cases named above, the STIRAP efficiency for each system will be investigated as a function of the laser intensities of both lasers. At the same time, this population transfer efficiency will be compared to optical pumping in the same interaction time.
For these simulations a pulse duration of 15ns standard deviation is chosen. In the perpendicular cw laser-setup geometry, the same 50 keV beam as for the optical pumping simulations results in a total interaction length of around 0.01 m. These parameters result in a total interaction time of $50 - 100$ns. To conclude on the feasibility of STIRAP as a replacement for the optical pumping method, experimentally acceptable laser powers should be known. For the cross-beam geometry, the cw-lasers will be in the mW-W power range, which is around $10^{-3} - 10^{-6}$J/m^2 that is accessible (increasing the pulse length in the cross-beam geometry with cw-lasers results in a reduction of the power density since it means making the beam spots larger). These units should be compared to the ones for which the adiabatic following condition is satisfied and STIRAP offers an efficient population transfer mechanism. Experimental applications of STIRAP, as cited in [25], with continuous wave lasers have succeeded with these kind of laser powers.

Figure 6.9 shows the transfer efficiency in the STIRAP laser pulse sequence for the four different decay strengths from intermediate to meta-stable level. In all four cases, three regions can be distinguished. First, for small powers, there is a non-efficient zone. This is followed by an asymmetric region of efficiency for high pump laser power. The population transfer mechanism in this last region is evolving towards optical pumping, because the influence of the Stokes laser continues to decrease. The efficiency obtained in this region should be taken with a grain

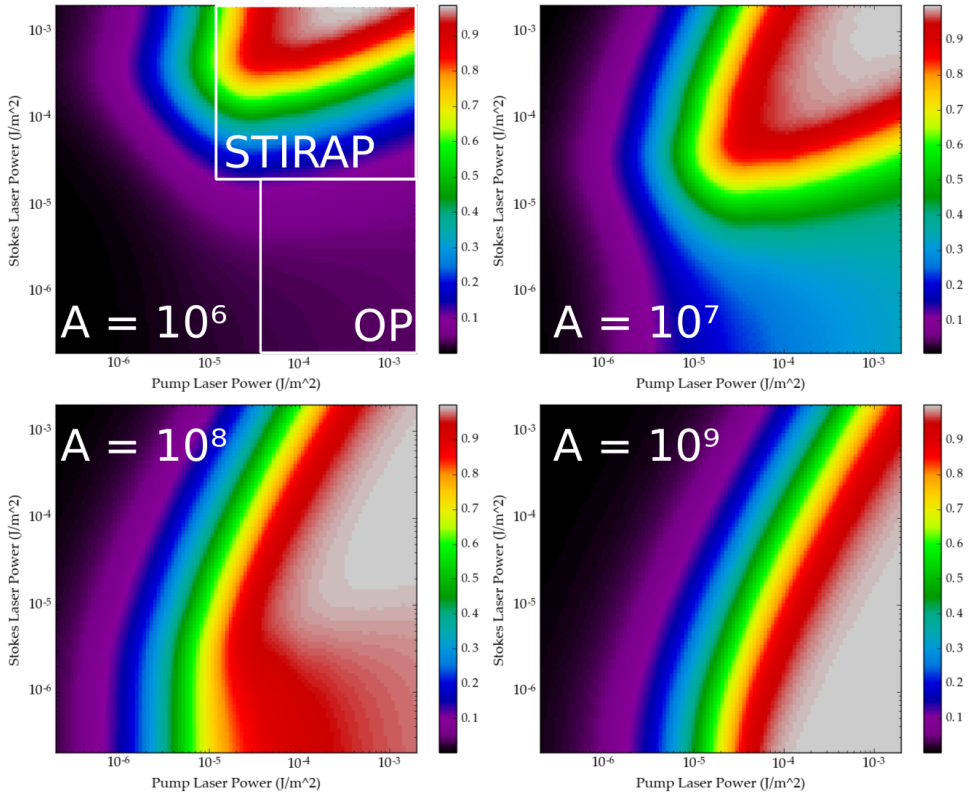

Figure 6.9: *Simulated STIRAP population transfer efficiency for a $I = 0$ Λ-scheme. The Einstein A parameter is for both cases equal to 10^8 for the pump transition while the A parameter for the decay to the meta-stable state is shown on the figure. The different regions discussed are given on the first figure.*

of salt however because the laser profile in the spatial dimension should be taken into account, reducing the efficiency. For the STIRAP method, this spatial profile is exactly necessary to obtain the pulsed-like character, therefore less efficiency reduction should be expected here in real life experiments. The last region in the top right of the 2D graphs can be interpreted as the adiabatic STIRAP population transfer. As the ratequation simulations show, the optical pumping region efficiency deteriorates for smaller decay strength, while the STIRAP efficiency roughly remains the same as long as adiabaticity is fulfilled. The reason why optical pumping and STIRAP procedures are indistinguishable for high A parameters is explained in [34].
The spin $1/2$ configuration should present no decreased population transfer efficiency for the STIRAP pulse sequence. Keeping the limits on maximal level densities of section 6.2.1 in mind, maintaining a double photon resonance between a hyperfine ground state level and another hyperfine meta-stable level should result in a 100 percent efficient population transfer if adiabaticity conditions are fulfilled. However, problematic is the fact that only one of the hyperfine ground states is connected to the final state. Due to the small energy difference between hyperfine levels, an equilibrium population distribution is quickly established for all hyperfine ground levels without any external interaction. This means that via a STIRAP or optical pumping procedure, only the population in one of the hyperfine levels can be transferred. Figure 6.10 shows the simulation results. Except for the fact that only a part of the population is available for STIRAP purposes and the obvious decrease in efficiency for optical pumping methods, the results are similar to figure 6.9.

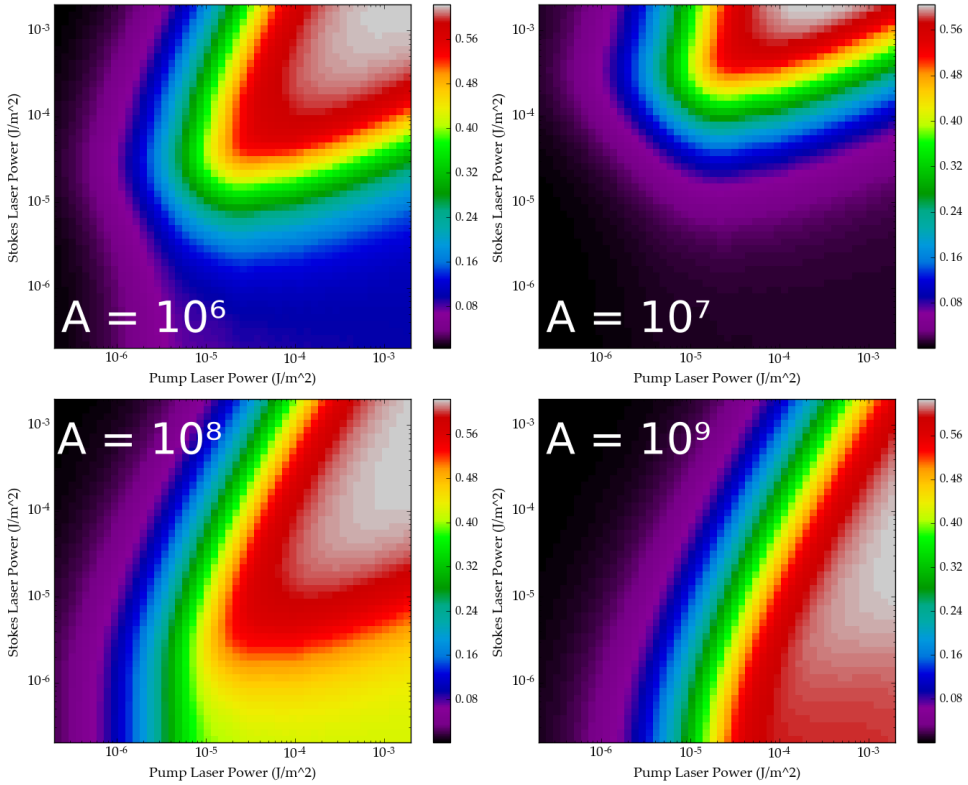

Figure 6.10: *Simulated STIRAP population transfer efficiency for an $I = \frac{1}{2}$ Λ-scheme. The Einstein A parameter is for all cases equal to 10^8 for the pump transition while the A parameter for the decay to the meta-stable state is shown on the figure. The different regions discussed are given on figure 6.9.*

As a last case, an extra loss term, of magnitude 10^9Hz, was added to the intermediate state, deteriorating the optical pumping efficiency by adding a decay path towards states outside the system (assume the decay rate quoted is the sum of all partial decay rates). Figure 6.10 shows the outcome of the simulations in this case. As expected only for the A parameter of 10^9Hz, for which the desired decay pathway is in a fair competition with the loss rate, the optical pumping region still shows some efficiency. For smaller decay rates, optical pumping completely loses its population transfer capabilities. The STIRAP procedure however still retains significant population transfer efficiency. The loss term does influence the STIRAP pathway when non ideal adiabatic conditions are present, reducing the perfect 100 percent transfer of population. For example, if the laser intensity is not adequate enough to ensure adiabatic following, population resides in the intermediate which is prone to population loss.

6.3.4 Conclusion

Concluding on the practical use of STIRAP for optical pumping procedures, the required laser intensity should be compared with the currently available continuous wave laser powers. From figures 6.9, 6.10 and 6.11, one deduces that the required intensity range to obtain a significant population transfer lies in the $10^{-5} - 10^{-3}$ J/m^2 range depending on the magnitude of the factors deteriorating adiabaticity. Comparing this to the before quoted available laser intensities of $10^{-6} - 10^{-3}$ J/m^2, signifies that according to the model used in this work, STIRAP could represent a feasible replacement of optical pumping methods for nuclear physics applications.

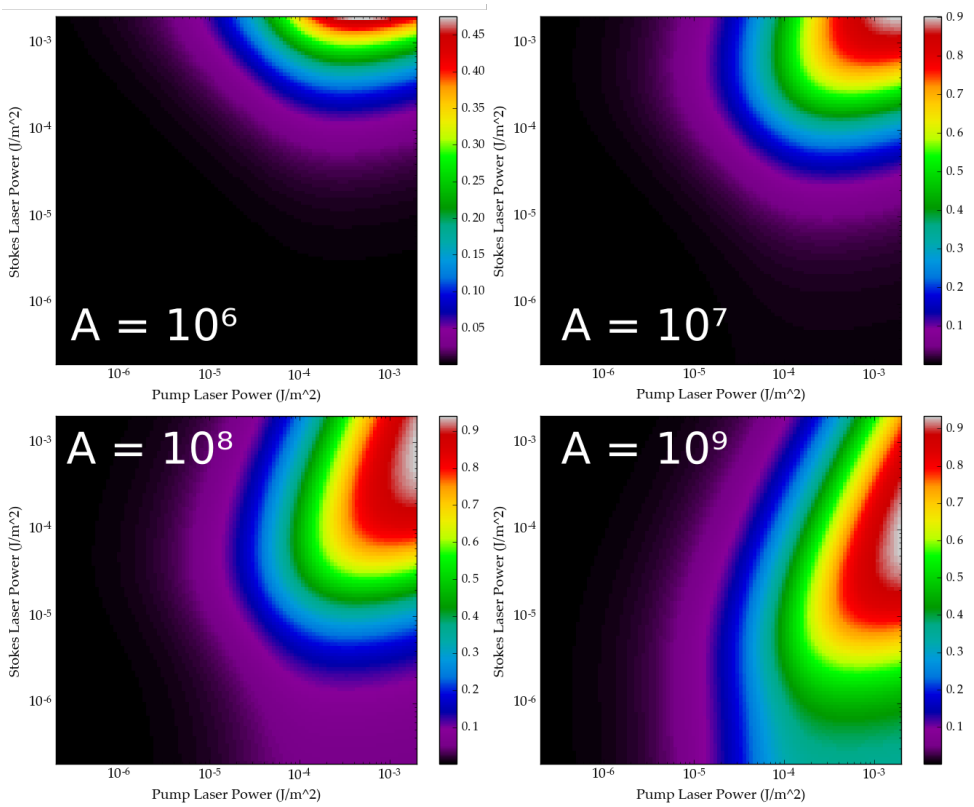

Figure 6.11: *Simulated STIRAP population transfer efficiency for a closed three-level Λ-scheme with an extra loss term added to the intermediate state. The Einstein A parameter is for both cases equal to 10^8 for the pump transition while the A parameter for the decay to the meta-stable state is shown on the figure. This figure should be compared to figure 6.9.*

STIRAP's efficiency in this setup of a few cm is comparable with long interaction length ($\sim$ m) optical pumping procedures when the atomic scheme favors optical pumping and exceeds the efficiency when the scheme is less favorable, as can be seen from figure 6.7 and 6.8. Regarding figure 6.5, pumping to a metastable state via STIRAP could be achieved for an in beam experiment by simply adding a four-way cross to the experimental setup.
In the case that the available atomic parameters are sufficiently detrimental such that higher laser powers are required to maintain the adiabatic regime, one can always consider using a pulsed laser setup. However as discussed in section 5, the increased power comes along with increased incoherences. Experimentally pulsed laser STIRAP has proven to work with pulse energies of around 1mJ. In this case however nearly transform-limited radiation is vital, otherwise very high pulse energies of around 1J are required. Transform limited radiation can be for example achieved from pulse amplification of cw-laser light [42]. Applied to the optical pumping replacement setup, pulsed lasers can also be used in a cross-beam geometry by firing them collinearly with a certain delay as in figure 6.5. However in this case, pulsed particle beams are no longer an option because of the limited repetition rate of the pulsed lasers. More concretely, only a small fraction of the atom/ion bunch will be illuminated. Gas-jet application among others could present an alternative.
One remark should be added, firing cw or pulsed lasers perpendicularly to the collinear beam setup requires mechanisms to deal with the Doppler spread on the ensemble, which is not

minimized as such when firing along the high energy beam. This remark will be dealt with in the next section.
The comparison between optical pumping simulations for long interaction times and STIRAP transfer calculations confirms STIRAP's insensitivity to external mechanisms (especially in the case of the added extra loss factor) which would normally reduce the optical pumping efficiency. Considering the fact that atomic level schemes including the hyperfine interaction are only rarely a closed three level system for which optical pumping operates most efficiently, STIRAP presents a feasible alternative.

6.4 STIRAP in a Doppler Ensemble

6.4.1 Introduction

The following possible application considers the use of STIRAP on a Doppler-broadened ensemble. In this case, the system consists of an ensemble of atoms, which have velocity vectors randomly distributed in space, interacting with laser photons. The magnitude of the velocity vectors are distributed according to a Maxwellian distribution, depending on temperature and mass. The relativistic Doppler shift is defined by:

$$\frac{f}{f_0} = \sqrt{\left(\frac{1+\left(\frac{v}{c}\right)}{1-\left(\frac{v}{c}\right)}\right)}. \tag{6.3}$$

Here f is the frequency seen by a particular atom when the photon frequency equals f_0. v is the component of the atom's velocity vector on the line collinear with the laser beam and c is the speed of light. The frequency of the laser photons, seen by the atom, is therefore shifted up whenever these atoms are traveling towards the light source and down when the opposite is true.
For such a system, using laser light to resonantly excite the entire system from one quantum state to another is inefficient because of the Doppler effect, shifting the wavelength of the laser photons differently for each velocity-vector (up to GHz shifting for $\sim 10^2$K). Therefore the shift in frequency is different for all atoms and thus broadband radiation will be required to achieve any efficiency.
The effect of the Doppler shift on the spectral line shapes as in RIS is called Doppler broadening, because the width of the lineshapes increases. Being able to resonantly excite an entire Doppler ensemble with narrow band lasers could result in applications for in-source laser spectroscopy for example, where the temperature of the source causes significant Doppler broadening. The focus of this section however lies on the application of STIRAP's optical pumping variant discussed in the previous section. Firing the laser perpendicularly to the particle beam will inherently result in some extra Doppler broadening compared to the situation where the laser is fired collinearly.

The relative unimportance of the single photon detuning on a STIRAP process could be an important step towards succeeding in applying efficiently a STIRAP pulse sequence to a Doppler-broadened ensemble. The idea is presented in figure 6.12. Assume one has an atom which interacts with two laser photons, one from each STIRAP laser, which travel in the same direction. Because the velocity vector of the atom appears at a certain angle with respect to

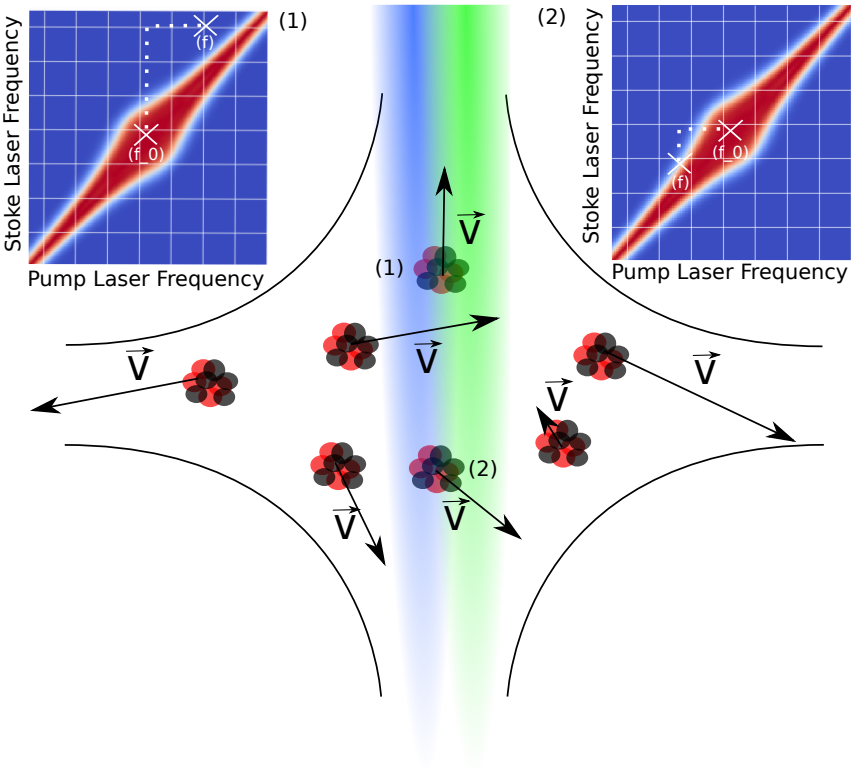

Figure 6.12: *Simulated STIRAP population transfer efficiency for a Λ-scheme. The resulting frequencies $f = (f_1, f_2)$, seen by the atom when firing both the Stokes as well as the pump pulse in the same direction (cross-beam geometry) at frequency $f_0 = (f_{01}, f_{02})$, is shown by the white dotted line on the STIRAP signature for two cases. The atom at (1) flies in the opposite direction of the laser photons, the Doppler shift is therefore in the direction of increasing frequency.*

the laser photons, the Doppler effect will shift both frequencies (f_0 to f). This effect is shown by the white dotted line in figure 6.12. By applying both lasers in the same direction, the result, depending on the transition frequencies of both atomic transitions, will remain close to the double photon resonance line for the Λ-scheme, [42]. For the ladder scheme, similar arguments hold when the lasers are aimed in opposite direction. Following this reasoning, efficient STIRAP population transfer is still possible in a Doppler-broadened ensemble because the transfer efficiency remains significant even when single photon resonance is not fulfilled. Two side notes should be made. First it should be observed that the degree of single photon detuning that a STIRAP process allows, while retaining high transfer efficiency, is strongly dependent on laser power density. Secondly, a bigger difference in transition wavelengths results in a frequency shift which will be further away from the double photon resonance line because the Doppler shift is dependent on the absolute magnitude of the frequency. Again, the maximum double photon resonance detuning allowing efficient transfer is dependent on laser power, [30]. A verification of this reasoning was done in [42] and checked by the code in this thesis. The results are similar, therefore a brief discussion of the outcome of [42] will be held to lay the ground work of the combination of the Doppler-broadened ensemble and optical pumping. Following the reasoning in the previous paragraph, three important parameters reduce the total efficiency for efficient excitation of a doppler-broadened ensemble, without considering any hyperfine structure.

First of all, because of the dependence on absolute frequency, the greater the difference in pump and Stokes transition wavelength, the more the Doppler shifted value will lie further from the double photon resonance, for example figure 6.14. Secondly, higher temperatures increase the Doppler broadening of the system. Therefore larger single photon detunings are required to excite the slowest and fastest particles. Finally, the smaller the power, the smaller STIRAP's efficient area in frequency space becomes (=STIRAP's signature). These intuitive arguments are confirmed by the simulations done in [42] and in this work. To show the feasibility of this application, experimental and simulation results of section 4 in [42] are shown in figure 6.13. Results of simulations done for this work, representing the three factors which determine the Doppler excitation efficiency, are shown in figure 6.14.

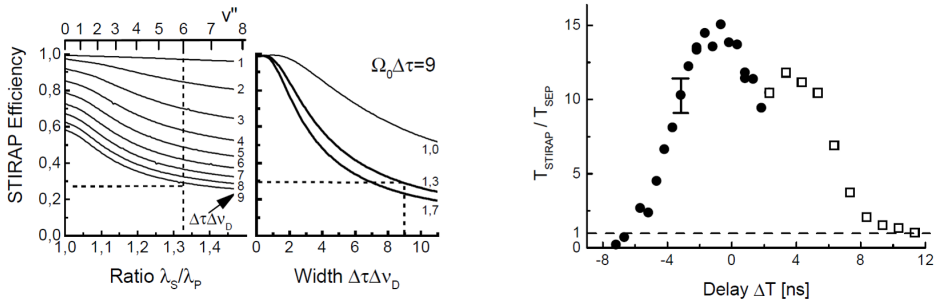

Figure 6.13: *Simulation and experimental results from [42]. The graph on the left shows the STIRAP efficiency as a function of the ratio of the transition wavelengths for a variety of temperatures. This confirms the first two assumptions in the text. The figure on the right shows the experimental results obtained when exciting NO molecules between their respective vibrational states at T=300K for different time delays between the pulses. Both the STIRAP process on the left (black dots) as the SEP process on the right (white squares) is visible.*

Two remarks should be added to the foregoing results which were not documented in [42]. First of all following the discussion in [30], a realistic atomic Λ-scheme will possess a certain asymmetry due to the angular momentum coupling rules defined in the Rabi frequency, as for example seen in figure 6.14. Studying figure 6.14 reveals that this asymmetry could be beneficial or detrimental to the population transfer efficiency, when the asymmetry points in the same direction as the diagonal from of the Doppler histogram (as is seen in figure 6.16 of the next section). This extra degree of freedom could be used for further optimization of the system by, if possible, manipulation of laser powers, which could enhance further the asymmetry. In the example of figure 6.14, reversing the ratio of the Rabi frequencies which determine the direction of the asymmetric bumps, reveals a efficiency drop by almost 40 percent. Finally, simulations with hyperfine structure were done. The basic principle is exactly the same and visualized in figure 6.15. Code is available to determine the population transfer efficiency to the ensemble of meta-stable levels or to a particular hyperfine level of this ensemble. Again asymmetry and proper frequency choices have to be considered when optimizing the setup. For this optimization procedure, simulation code is available.

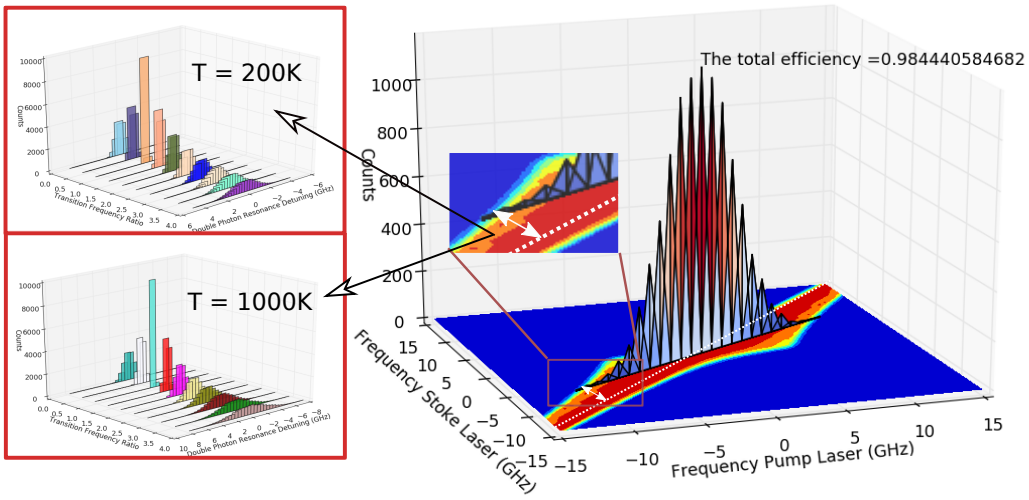

Figure 6.14: *Simulation of a STIRAP signature applied to a Doppler-broadened ensemble. The excitation efficiency is visualized together with a histogram showing the number of atoms interacting with a particular combination of possible frequencies due to the Doppler shift for a set of external parameters. The three parameters determining the transfer efficiency are displayed. In the inset, the histogram of frequency detuning from double photon resonance (in GHz) seen by the atoms is shown (which is the shift visualized by the white double arrow). This is done for two temperatures and several different transition wavelengths. If both Stokes and pump transition are the same, all atoms have zero detuning with respect to the double photon resonance. For larger ratios between laser frequencies, the histogram diagonal will shift with respect to the STIRAP diagonal. Finally the power dependence will increase the STIRAP signature.*

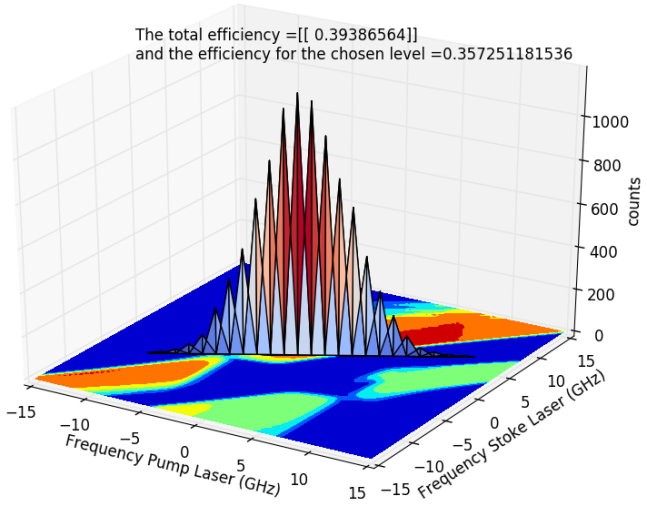

Figure 6.15: *Simulation of a STIRAP signature applied to a Doppler-broadened ensemble for a Λ-scheme with hyperfine sublevels. Both the total excitation efficiency and the efficiency towards a particular hyperfine sublevel of choice is calculated (here the level fed by the biggest STIRAP signature).*

6.4.2 Optical Pumping on a Doppler-Broadened Ensemble

As stated before, the focus here lies on applying the potentially feasible STIRAP optical pumping replacement to a Doppler-broadened ensemble without losing too much population transfer efficiency. As an example, two figures similar to 6.9, 6.10 and 6.11 will be shown when STIRAP is applied to a Doppler-broadened ensemble. The total efficiency e for each combination of laser intensities was then calculated via:

$$e = \sum_{\vec{v}} P(\vec{v})e(\vec{v}). \tag{6.4}$$

Here, $P(\vec{v})$ is the probability of the particular orientation the velocity vector of the atom has with respect to the laser beam. $e(\vec{v})$ represents then, for a particular Doppler shifted pump and Stokes laser frequency, the population transfer efficiency. Around 2GHz of maximum Doppler shift is expected for a bath of 400K. This should be close to the experimental conditions confronted when working with cross beam geometry laser excitation. The results of this scheme are shown in figure 6.16. Decreasing population transfer is visible with more profound effects for larger frequency ratios between both transitions. However, still a significant efficiency is maintained within available laser powers.

6.4.3 Conclusion

The goal of sections 6.3 and 6.4 was to prove the feasibility of introducing STIRAP as optical pumping replacement in nuclear physics methods. As discussed in 6.3, this could be done by introducing a four way cross element to the beam-line and firing pump and Stokes lasers perpendicularly to the particle beam. In this geometry however, the Doppler shift should be taken into account. The introduction of the Doppler ensemble to the simulation results in, the in section 6.3.3 revealed, transfer losses. However, significant transfer efficiency is still obtainable for available cw-laser powers when the transition wavelengths of both pump and Stokes pulse are not too far apart (too far determined by the available magnitude of the laser intensity). As a conclusion, one can state that applying counter-intuitive pulses perpendicularly to a atom/ion beam delivers comparable population transfer efficiency in a few cm as optical pumping methods does in more than a meter of interaction length. So far this application of STIRAP proves to be achievable in most cases.

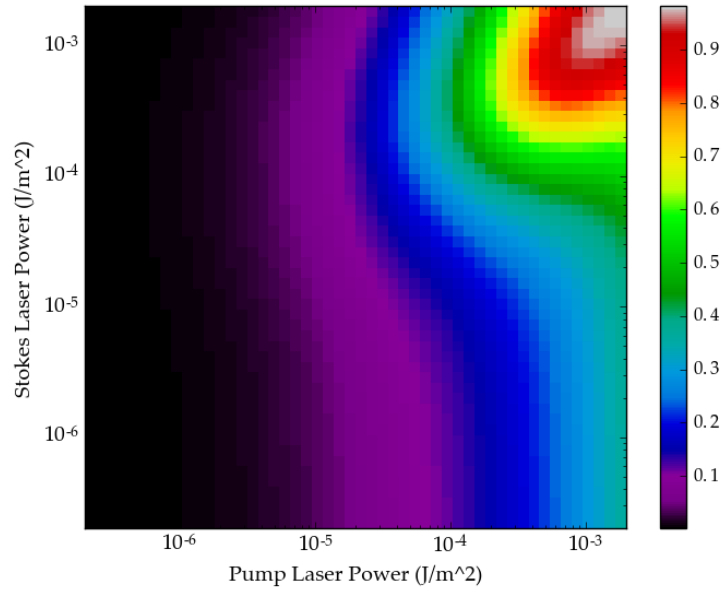

(a) $\lambda_{pump}/\lambda_{Stokes} = 1$

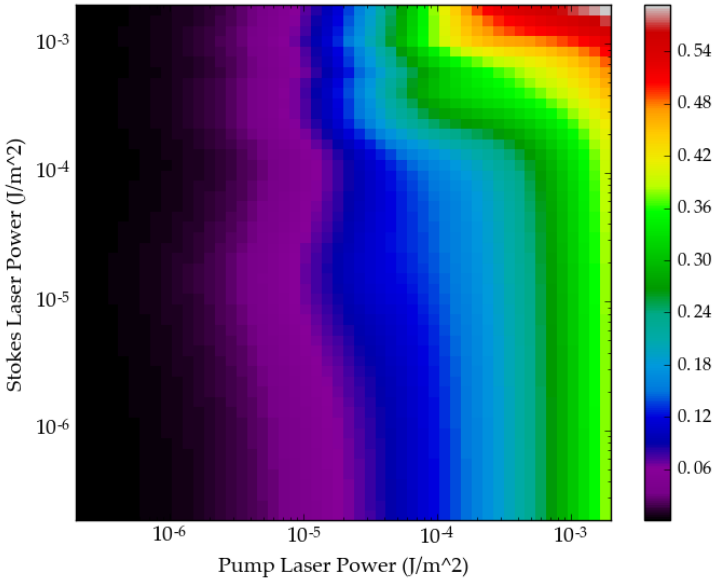

(b) $\lambda_{pump}/\lambda_{Stokes} = 1.5$

Figure 6.16: *Similar STIRAP efficiency graphs as those discussed in figures 6.9, 6.10 and 6.11. However for these simulations a Doppler ensemble with average temperature of 400K was considered resulting in around 1GHz average Doppler shift. Both figures were simulated for an A parameter of* 10^8 *for the two transitions. The other cases of 6.9, 6.10 and 6.11 will show similar effects. A decrease in population efficiency compared to figures 6.9, 6.10 and 6.11 is noticeable but not detrimental. As expected, increasing transition wavelength ratios deliver more detrimental effects on the STIRAP efficiency.*

6.5 STIRAP with Auto-Ionizing levels

6.5.1 Efficient Ionization?

As previously discussed in section 5.6.3, a STIRAP sequence involving the continuum as one of its levels is still possible [35], [36] and [37]. As illustrated in these references, adding structure to the continuum will only improve population transfer efficiency. The focus on this section lies on the application of the STIRAP procedure to auto-ionizing levels, which are discrete level structures in the continuum. This has been done before, [43], where the auto-ionizing level was located as the middle level of the three-step scheme. Their analytic results will be summarized and applied to the case where the auto-ionizing level is the final level of the three-step ladder scheme. The goal is as always to excite as efficiently as possible the ground state population to the auto-ionizing level. As a consequence of this however, most of the auto-ionizing level population will decay to the continuum and leave the atom ionized. The goal of this section is therefore to investigate if auto-ionizing levels can be used with STIRAP or the intuitive pulse sequence as efficient ionization pathways.

To describe the auto-ionizing state in the quantum mechanical model applied in this work and understand the influence it has on the STIRAP process, one is referred to [43]. Here the auto-ionizing level is described similarly as any other atomic state, supplied with an irreversible decay rate, γ_a for a three-level Λ-scheme. This decay rate is then added as an imaginary term on the respective diagonal element of the Hamiltonian. Following [43], the Hamiltonian in the atomic and adiabatic basis is (double photon resonance is assumed):

$$H \sim \begin{pmatrix} 0 & \Omega_P(t) & 0 \\ \Omega_P(t) & \Delta - i\gamma_a & \Omega_S(t) \\ 0 & \Omega_S(t) & 0 \end{pmatrix}. \tag{6.5}$$

$$H_{ad} \sim \begin{pmatrix} \Omega_{eff}\cot(\Phi) - i\gamma_a \cos(\Phi)^2 & i\dot{\Theta}\sin(\Phi) & i\dot{\Phi} + 1/2 i\gamma_a \sin(2\Phi) \\ -i\dot{\Theta}\sin(\Phi) & 0 & -i\dot{\Theta}\cos(\Phi) \\ -i\dot{\Phi} + 1/2 i\gamma_a \sin(2\Phi) & i\dot{\Theta}\cos(\Phi) & \Omega_{eff}\tan(\Phi) - i\gamma_a \sin(\Phi)^2 \end{pmatrix}. \tag{6.6}$$

All parameters are defined as before. The fact that the goal in this case is maximum population transfer efficiency rules out using the intuitive pulse sequence because of the overlap of the desired adiabatic state with the intermediate level, which ionizes quickly, see section 5.4. The STIRAP insensitivity to the characteristics of the intermediate level are useful in the case where ionization is not the goal.
Therefore [43] reports an exponentially decreasing population transfer ,as a function of ionizing strength, to the final state when using the intuitive pulse sequence. Using the counter-intuitive pulse sequence however, no population will reside in the intermediate level when the adiabatic condition is resolved. For this case then, depending on a on the parameter values, even γ_a in the GHz range still allows for an efficient STIRAP procedure. For increasing γ_a, the population which does enter the intermediate state for non-perfect adiabatic conditions will leave the system more efficiently. For even larger γ_a, the already encountered quantum overdamping effect destroys any remaining efficiency.

Following these discussions, a similar model was investigated where the auto-ionizing state

represented the final state of the ensemble. In this case, no trivial advantage for the counter-intuitive STIRAP sequence or the normal intuitive laser pulse sequence could be determined but their insensitivity towards the single photon detuning could bring possibilities for efficient Doppler ensemble ionization. In this case, as opposed to [43], the goal is ionization.
In-source laser spectroscopy achieves element specific ionization by using broadband lasers to wash away the Doppler ensemble supplemented by a powerful non resonant ionization laser pulse or a step towards an auto-ionization state. This can be efficient in the ~ 10 percent range.
Following simulations, the use of narrow-band band laser for efficient Doppler excitation is investigated for counter-intuitive pulse sequences. Both Hamiltonians, similar to (6.5) and (6.6) are (the adiabatic Hamiltonian has been written, for clarity purposes, as the difference between (5.4), H_{ad}, and the adiabatic Hamiltonian obtained for the three level ladder-scheme with auto-ionizing final state, $H_{ad/auto}$):

$$H \sim \begin{pmatrix} 0 & \Omega_P(t) & 0 \\ \Omega_P(t) & \Delta & \Omega_S(t) \\ 0 & \Omega_S(t) & -i\gamma_a \end{pmatrix}. \tag{6.7}$$

$$H_{ad} - H_{ad/auto} \sim \begin{pmatrix} -i\gamma_a \cos(\Theta)^2(\cos(\Phi)^2 - 1) & -i\gamma_a \cos(\Theta)\sin(\Theta)\sin(\Phi) & i\gamma_a \cos(\Theta)^2 \sin(\Phi)\cos(\Phi) \\ -i\gamma_a \cos(\Theta)\sin(\Theta)\sin(\Phi) & -i\gamma_a(\cos(\Theta)^2 - 1) & -i\gamma_a \cos(\Theta)\sin(\Theta)\cos(\Phi) \\ i\gamma_a \cos(\Theta)^2 \sin(\Phi)\cos(\Phi) & -i\gamma_a \cos(\Theta)\sin(\Theta)\sin(\Phi) & i\gamma_a \cos(\Theta)^2 \cos(\Phi)^2 \end{pmatrix}. \tag{6.8}$$

Accompanying the fact that for a three-level ladder-scheme, STIRAP is inherently less efficient than for a Λ-scheme, some other comments can be made regarding the use of the counter-intuitive pulse sequence for efficient ionization via auto-ionizing levels.
First of all, the obvious advantage of STIRAP over intuitive pulse sequences because of its insensitivity to intermediate decay pathways, is no longer of importance. Only when the intermediate state would be decaying towards an external state, this statement should be revised.
Secondly, looking at (6.8), shows that increasing γ_a, increases the non-adiabatic coupling between the STIRAP dark state $|a^0\rangle$ and all others, which is detrimental for STIRAP's highly efficient population transfer. In the previous case, with the auto-ionizing state as intermediate level, only the coupling between $|a^-\rangle$ and $|a^+\rangle$ is influenced by the magnitude of γ_a. Therefore it is expected that a counter-intuitive pulse sequence does not offer any significant advantages above present day methods working by intuitive pulse sequence to auto-ionizing states. This is confirmed by simulations.

6.5.2 Conclusion

Theoretical arguments, confirmed by simulations, show no clear advantage for increased counter-intuitive efficient population transfer to an auto-ionizing state. Present day, broad-band, high powered laser methods are likely to overrule the efficiency offered by lower powered-narrow band coherent transfer methods by intuitive or counter-intuitive pulse sequences.

Part IV

Conclusion and Appendix

Chapter 7

Conclusion and Outlook

This thesis consists of two major parts. First of all, the relevant laser-atom interactions in resonant laser ionization experiments were studied with the goal to improve the extraction of experimental parameters.
The second part of this thesis dealt with the introduction of an efficient coherent population transfer method between quantum states. This new procedure was examined and its potential applications in nuclear physics methods studied.

Optimizing laser-atom interactions for RIS experiments involves understanding three major effects on the experimental observables caused by this quantum phenomenon of photon-atom interactions. First and second, the interaction of excitation and ionization lasers with the atoms or ions determines the spectral resolution achievable by the experiment and the accuracy of the obtained parameters. Third, the atom-laser interaction is a vital parameter which determines the total efficiency of the experimental setup. A model to describe the entire quantum mechanical laser-related interaction in a RIS experiment with pulsed laser radiation was extensively covered in [1]. The conclusion of that work, supported by theoretical and experimental arguments, states that separating the two laser pulses in time offers improvements on not only on the accuracy of the obtained data but also on the precision. The only issue lies with strong transitions. These transitions will cause a strong decay of excited population back to the ground state before the ionization laser has fired, reducing the efficiency of the process.
The quantum phenomenon of spontaneous decay and other theoretical findings, added to the model in this thesis proved to be vital in the understanding of the link between the decay/coupling strength of two quantum levels. In full agreement with the recommendations of [1], a complete argumentation in favor of using weak transitions for high precision laser spectroscopy was developed. This argumentation dealt with the advantageous characteristics of weak transitions in the possibility for delayed ionization, inherent linewidth, saturation and steady-state population of the excited level. It was shown that decreasing the Einstein A parameter of the transition has a similar effect to the attainable excited state population as increasing the laser power. This meant however increasing the excitation laser pulse length. It was therefore concluded that experimentally comparable efficiencies can be obtained for pulsed high power laser excitation as for low power, high resolution, chopped cw radiation. This chopped cw laser light is most likely not powerful enough to saturate the atomic transitions in many cases, therefore it could be beneficial to use weak transition to increase the efficiency in the case the superior resolution of the chopped cw radiation is required

Thus, weak transitions are capable of offering high resolution characteristics by using chopped cw-light and delaying the ionization pulse with respect to the excitation laser. On top of this, high experimental efficiency by increasing the excitation laser pulse length can be obtained. The overall characteristics of the model were tested on two different experimental data-sets, and proved to be conform reality.

Many applications in nuclear physics, involving the interaction of lasers with atoms, are in one way or another related to the excitation of population from one quantum level to another. The STIRAP coherent population transfer mechanism offers a 100 percent efficient way of doing this. Therefore many potential applications in nuclear physics techniques could be envisioned. The feasibility study of a few of these applications was performed in this work. The replacement of long interaction time, collinear beam, optical pumping practices by a much shorter cross-beam geometry STIRAP was found to show promising results.

This work has presented a theoretical summary of two major applications of laser-atom interactions in nuclear physics. The characteristics of this interaction were studied via the aid of simulations on the theoretical model. From these characteristics, improvements to experimental practice, for more accurate, precise and efficient determination of nuclear observables, were suggested alongside their feasibility. A next, vital step, would be the conversion from theory to practice of these general recommendations and to check their validity and therefore the validity of the model. The influence of increasing pulse length on weak transitions could thus be tested in off-line experiments. For the STIRAP optical pumping procedure the same outlook is applicable.

Appendix A

CRIS

This chapter will give an overview of the CRIS experimental setup which is located at ISOLDE-CERN. Its goals as well as its advantages and downsides will be explained. A detailed scheme of the setup itself is also included. First however a brief introduction to nuclear moments is given

A.1 Nuclear Moments

The CRIS setup is used to obtain the nuclear moments by laser spectroscopy. This boils down to comparing to very high precision the electron energy levels in a hyperfine multiplet of the exotic isotopes. The interaction between the nuclear moments and the electron fields is visible in the hyperfine splitting of these electron levels [44]. The observed spectra can therefore be used to obtain these moments.

A.1.1 Hyperfine Interaction

To describe the hyperfine interaction, the complete atom-electron cloud system should be considered. If it is assumed that the nucleus is in a certain quantum state $|I\rangle$ and the entire electron cloud can be described by a wave function $|\psi\rangle$, the expected energy of the complete atom, thus the vector product of both nuclear and electron systems, can be written as:

$$\begin{aligned} E = &\langle \psi \otimes I | T_e + U_e - \frac{e^2 N Z}{4\pi\epsilon_0 r_e} | \psi \otimes I \rangle \\ &+ \langle \psi \otimes I | - \frac{e^2 N Z}{\epsilon_0} \left(\sum_{n=1}^{\infty} \frac{r_n^n}{r_e^{n+1}} \frac{1}{2n+1} Y^n(\theta_n, \phi_n) Y^n(\theta_e, \phi_e) \right) | \psi \otimes I \rangle . \\ &- \left(\langle \psi \otimes I | \sum_{n=0}^{\infty} \frac{B^n \cdot M^n}{2n+1} | \psi \otimes I \rangle \right) \end{aligned} \tag{A.1}$$

In this equation, one can find many familiar terms. T_e and U_e represent respectively the kinetic energy contribution of the electrons and the electron-electron interaction. The subscript e is used to denote electronic characteristics and n for nuclear. The first term on the right of equation (A.1) determines the fine structure levels. This interaction includes electron-electron interaction and the first order term in the electron-nucleus interaction. The second and third

term give the expansion of the remaining part of the latter interaction (charge-charge and current-current in rising order of spherical harmonics). This expansion can be seen as the interaction between nuclear multipole moments and electron multipole fields. The current-current interaction term can't be written in an enlightening expansion as can the charge-charge interaction because this interaction is of a vector character and therefore more complicated. These different interactions will shift the energy levels of the electrons determined by their first order Coulomb interaction. For the purposes of this report, considering the quadrupole term of the charge-charge interaction and the dipole term of the current-current interaction is sufficient. Because of this interaction, the nucleus-electron cloud system is often described by its total spin F, whereby $|I-J| < F < I+J$.

A.1.2 From Hyperfine Spectra to Nuclear Observables

Generally there are two ways to analyze the measured hyperfine structures [45]. The most straightforward way to look at the data is direct evaluation of the hyperfine structure in terms of energy differences between the peaks. This can give information on the nuclear dipole moment, the nuclear spin and the electric quadrupole moment. A second way to look at the hyperfine splitting is by comparing the spectra of two isotopes and calculating the so called isotope shifts between the two isotopes. This isotope shift is related to the mean squared charge radius $\langle r^2 \rangle$. When analyzing the hyperfine spectrum directly, the hyperfine parameters A and B can be deduced. These parameters can be calculated with following equations:

$$W_F = \frac{1}{2}AC + B\frac{\frac{3}{4}C(C+1) - I(I+1)J(J+1)}{2I(2I-1)J(2J-1)}, \tag{A.2a}$$

$$C = F(F+1) - I(I+1) - J(J+1), \tag{A.2b}$$

where W_F is the energy of the F-level of the hyperfine structure multiplet. The nuclear spin I is not necessarily known, especially in the case of exotic isotopes. However, the nuclear spin can also be determined from the spectrum. Two separate situations are possible according to the fact that $|I-J| < F < I+J$. When $I < J$, each fine level will be split in $2I+1$ hyperfine levels. In this case the amount of hyperfine levels can be counted to obtain I. The second possibility is that $I > J$ in which case there are now $2J+1$ hyperfine levels and thus there is no simple relation between the amount of levels and I. Most often, given a spectrum of hyperfine levels, advanced fitting procedures with the use of Voigt profiles are applied to characterize the resonant peaks. The optimal fitting parameters then give the hyperfine A and B unknowns which are strongly related to the nuclear observables one is interested in. Following the derivation of equation (A.2a), one can see that the A parameter can be written as:

$$A = \frac{\mu_I B_{e,0}}{IJ}. \tag{A.3}$$

In this equation, μ_I represents the magnetic dipole moment of the nucleus with spin I. $B_{e,0}$ is the magnetic field caused by the electrons in an orbit characterized by the total angular momentum J and projection $J_z = J$ at the origin. The parameter B is directly related to the electric quadrupole moment, namely

$$B = eQ_s V_{zz,0}, \tag{A.4}$$

where Q_s is the electric quadrupole moment and $V_{zz,0}$ the electric field gradient due to the electrons. As mentioned earlier, through the measurement of the isotope shift of the hyperfine structure one can determine the mean squared charge radii of various isotopes. This also provides valuable information on possible deformations of the nucleus. The shifts are usually extremely small and are given by

$$\delta\nu_i^{A,A'} = F_i\delta\langle r^2\rangle^{A,A'} + M_i\frac{m_{A'}m_A}{m_{A'}m_A}, \tag{A.5}$$

where F_i is the field shift constant and M_i the mass shift of the ith transition and m_A and $m_{A'}$ the masses of the two isotopes. The constants F_i and M_i can be calculated theoretically. The first term is the *Field shift*. This term can be understood by realizing that the nucleus is a finite distribution of protons and neutrons. Changing the amount of neutrons, going along an isotopic chain will change the volume distribution of the nucleons due to the added neutrons. The second term is the *Mass shift* and is caused by a change in kinetic energy due to the change in nuclear mass. So when the mean squared charge radius for a given isotope, for example the stable isotope, is known, the other radii can be determined.

A.2 Collinear Laser-Spectroscopy

A.2.1 Introduction

As stated before in the previous sections, the ultimate goal of laser-spectroscopy is, in the case of interest for this thesis, to determine nuclear moments derived from hyperfine spectra. The goal of this experimental method is to provide a way in which these observables can be obtained for very exotic nuclei. This means that laser-spectroscopic methods have to be developed which bring extreme selectivity, high efficiency and equally high resolution to the table. The collinear resonant ionization laser spectroscopy technique is well suited to tackle these challenges.

A.2.2 Resonance Laser Spectroscopy

In this subsection, the basic principles and advantages of collinear resonant ionization laser spectroscopy (CRIS) are briefly covered. In a CRIS experiment an n-step ionization laser scheme is searched to obtain at the same time the required high selectivity and resolution. First of all, the unique transition frequencies for every isotope deliver the perfect scenery to probe one isotope at a time by resonant excitation. Firing a laser at a certain frequency which just matches the unique transition frequency of the isotope in question will induce an enormous rise in the cross section for excitation for this particular isotope while not interacting at all with others. Immediately (at the same time or with a certain delay) firing an ionization laser will, if the frequencies are well tuned, only ionize those isotopes which were already excited. As claimed before, any number of excited steps can in theory be applied. The decision in how many steps to use lies first and foremost in the desired transition wavelengths and their availability for the present lasers. First experiments with CRIS used one excitation step.
The final spectra are then obtained by scanning the excitation laser frequency over a broad range which covers completely the hyperfine levels one is interested in, see figure A.1. At each resonant frequency, there will be a distinct rise in ion yield detected by ion detectors (see section A.3.4). These spectra are then fitted with Voigt profiles to obtain the corresponding

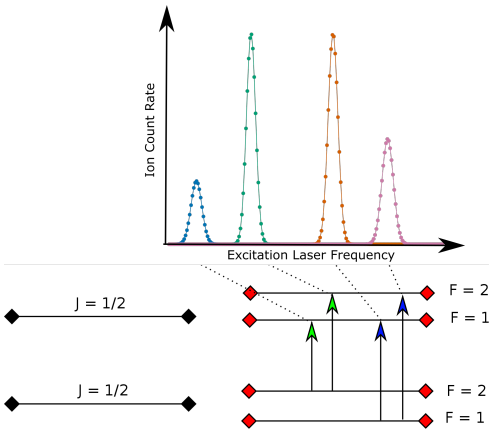

Figure A.1: *A pictorial representation of the method used by a RIS experiment to obtain the nuclear observables.*

resonances. From this one can extract the nuclear observables as in section A.1. Second, a very good resolution is, as stated before, vital for the experiments. This is the main reason why the collinear geometry is applied to the resonance ionization laser spectroscopy method. Accelerating the ion beam and firing the laser exactly on the same line as the ion beam minimizes the Doppler spread of the isotopes in question which makes the resolution of the experiment mainly dependent on the laser linewidths. Other features of this experimental method boosting the resolution, sensitivity and efficiency are further shown in figure A.3 and explained in following sections.

A.3 CRIS: Setup

The CRIS setup at ISOLDE has been developed for the experimental research of radioactive isotopes far from the stability line. The major goal of this setup is to obtain data to determine the magnetic moment, quadrupole moment and charge radii of the nucleus of these isotopes through hyperfine interaction studies and isotope shifts as described in Section A.1. The CRIS setup offers through its high detection efficiency, low background and very high resolution a good way of determining these values for isotopes with yields as low as 1 atom/s [46]. In this section an actual CRIS setup will be described. The description is based on the setup installed at ISOLDE, CERN which has four major components. The incoming beam, the CRIS beamline itself, the laser systems and the detection chamber.

A.3.1 The ISOLDE Cooler (ISCOOL)

The desired isotopes are produced at the ISOLDE facility by bombarding a target, for example uranium, with protons coming from the PSBooster. An entire collection of elements will be produced in this reaction. These ions are then accelerated to 30-50 keV and mass separated. In the early days the beam would then arrive continuously at the setup. This resulted in huge duty cycle losses and the efficiency for a CRIS experiment was as low as 0.001 % [47]. The magnitude of this number led to a new interest in the use of bunched beams together with pulsed lasers, this would in principle increase the duty cycle by a few orders of magnitude. At ISOLDE the increase in efficiency in this current stage of the experiment is due to cooling

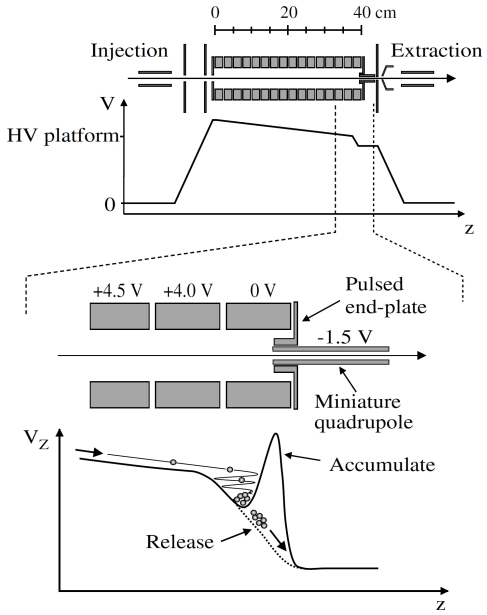

Figure A.2: *A representation of the general components of the cooling and bunching technique. The RF quadrupole cools the ions, then the ions are bunched by switching the potential barrier on and off. The figure was adapted from reference [46].*

and bunching the ions in a gas-filled RF quadrupole linear Paul trap. This setup is called the ISOLDE cooler or ISCOOL [48]. This is the last stage before the beam enters the actual CRIS setup. The ISCOOL arrangement shown in Figure A.2 has two objectives, namely improving the emittance and energy spread of the ion beam compared to the situation in which the beam was not bunched. On top of this, it creates short bunches of ions with repetition rates as high as 200Hz.

The general setup of ion traps like ISCOOL consists of a gas-filled RF quadrupole placed on high voltage. This voltage is a few hundred volts lower than the separator potential. This causes the ions to decelerate as they enter the trap. The quadrupole structure is made out of four rods for which adjacent rods have opposite parity RF voltage and the same DC voltage. The RF voltages are used to focus the beam, while the DC voltage is used to guide the ions to the exit. This cooler setup has made a 60-70 % transmission efficiency and an energy spread of 1 eV possible. At the end of the cooler the bunching of the ion beam occurs. Here the ions are first thermalized by a buffer gas while still under the influence of a weak axial field. This axial field guides the beam to the trapping region. In this trapping region a stronger axial field gradient is provided alongside a potential barrier which can be turned off and on to bunch the beam. After cooling and bunching, the total energy spread of the beam is of the order of one part in 10^5 of the total energy which is of the order of 10 keV. This makes sure that the Doppler broadening of the atomic energy levels is smaller than their natural linewidth. An extra advantage of this technique to make a bunched ion beam is that more background events are suppressed.

A.3.2 The CRIS Beamline

The complete beam line is shown in Figure A.3 [49]. The first distinct region of the CRIS beamline is the charge exchange cell. In this cell the accelerated ion beam will interact with a potassium vapor at 150 degrees centigrade. This will cause a neutralization of the beam through collisions with the potassium atoms. The pressure of about 10^{-6} mbar in this region is the highest pressure reached in the beamline. The neutralization process has been tested with a 60 keV beam of ^{85}Rb, which demonstrated an efficiency of around 70 % dependent on the neutralization gas and the incoming beam. Non-neutralized atoms are deflected away from the beam at the end of the charge exchange cell.
The completely neutralized beam then continues through a differential pumping setup to the interaction region, where they will overlap with lasers. This differential pumping region is necessary because one wants the pressure in the interaction region to be as low as possible. This way there is a lower probability that one of the neutralized isotopes collides with rest gas in the interaction area and ionizes through collisional ionization. When this happens at frequencies at which no resonant ionization should occur for certain isotopes, these ions will simply add to the background of the spectrum, which one obviously wants to keep as low as possible. To achieve this goal the pressure is lowered in the differential pumping section from the value attained in the charge exchange cell to 10^{-8}-10^{-9} mbar in the interaction region. The overlap with the lasers will make the multistep resonant ionization possible. An additional bend makes sure no neutral atoms can reach the final detection station and therefore cannot contribute to the eventual signal. The resonantly ionized atoms can be measured in two different ways.
First of all, they can be made to proceed to a MCP device, which measures the incoming beam current.
The beam could also be send towards ion detection system or, if the alpha decays of the isotopes are to be studied, to the Alpha Decay Spectroscopy Station (DSS).
Due to the collinear geometry of the setup, the ions can easily be accelerated. This acceleration results in a reduction Doppler broadening of measured peaks in the spectra. That this reduction works by accelerating the beam, can easily be seen by looking at the following equation:

$$\Delta v = \Delta v_0 \sqrt{\frac{\Delta E}{eU}}, \tag{A.6}$$

where Δv_0 is the initial velocity spread, ΔE the energy spread which remains constant after acceleration and U the applied voltage. Another advantage of this geometry is that just prior to the gas exchange cell, the velocity of the ions can be changed slightly by applying a voltage. This will cause a shift in the energy of the hyperfine levels. This process is called *Doppler tuning*. This way a fixed frequency can be chosen for the laser which is used to excite the isotopes. Scanning of the frequencies until resonance occurs can thus effectively be done by tuning the voltage and thus the energy of the hyperfine levels. The advantage of this is that in general a voltage is easier to stabilize after changing it, rather than the frequency of the laser. However, modern lasers are capable of offering large inherent scanning ranges with increased stability. Therefore, recent CRIS experiments have switched from Doppler tuning to laser tuning.

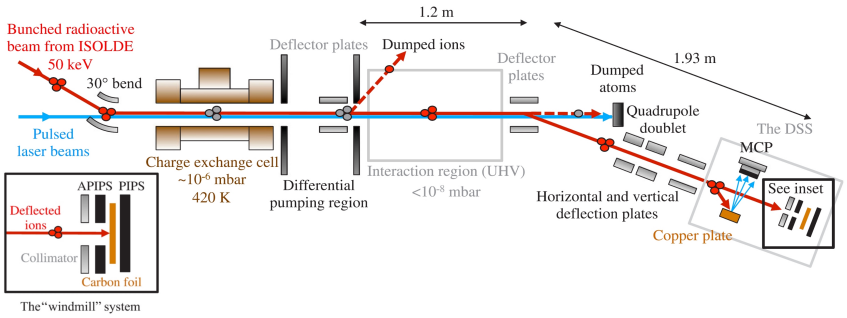

Figure A.3: *Graphical representation of the different components of the CRIS beamline as discussed in this paper. The ions are first neutralized so that the resonant ionization occurs properly. In the interaction area, the ions are also accelerated to reduce the Doppler broadening. This figure was adapted from Reference [50].*

A.3.3 The Laser System

In recent years, a completely new laser lab has been installed at ISOLDE-CERN. The CRIS collaboration now has collected a considerable amount of laser systems, suited to tackle a variety of physics cases. The ultimate goal of CRIS is to offer high efficient and high resolution laser spectroscopy. The lasers constitute a very important element in the experimental chain to obtain these goals, therefore high power and small linewidth laser systems are vital.
In the current setup, CRIS has at its disposal a number of lasers. First of all, high power pulsed lasers are available: pulsed Ti:Sa's pumped by a Lee laser and a pulsed dye laser pumped by a Lightron source. Next, also a special high powered, high resolution, injection seeded Ti:Sa is at hand [18]. Alongside the pulsed laser, also high resolution continuous wave lasers are accessible: a M^2 and a Matisse dye laser.
In these kinds of experiments, achieving the best resolution possible to completely resolve the hyperfine levels is of utmost importance. As explained before, the use of a collinear geometry minimizes the Doppler broadening and the resolution is thus mainly determined by the inherent laser bandwidth. Small bandwidth pulses can be achieved by chopping the laser light of a CW laser. This chopped laser then uses the inherent smaller bandwidth of continuous wave lasers alongside the advantages delivered by conventional pulsed laser beams. The chopping of the CW laser beam can be done with the use of a Pockel cell. The optical axis of this cell can be altered by applying voltages to it. The voltages needed are very high so the use of this cell to chop the beam at the needed frequency is far from trivial [13].

A.3.4 The Detection Chamber

The ions finally emerging from the beam line are then deflected to their end station in the detection chamber. Two possibilities exist here. The ions can be deflected to a copper plate to produce secondary electrons. These electrons are then detected by a MCP. The efficiency of the apparatus was estimated to be more than 30 %. Problems existed with background counts due to radioactivity of the copper plate itself or random noise in the electronic equipment. Counts from the radioactivity of the copper plate were dependent on the intensity of the beam and the half-lives of the decay products. These unwanted counts could therefore be minimized by avoiding high intensity beams. When high sensitivity is needed, the activity of the plate was allowed to decrease before new measurements were taken [50].

The ions can also be deflected to an α-decay spectroscopy setup to get additional information on the decays of the isotopes. The main components of this setup are the carbon foils for implantation of the ions, planted on a rotatable wheel with different entries, controlled by a stepper motor and a silicon detector setup. The use of this device results in a high solid angle coverage and α-particle detection efficiency of about 68 %. High purity germanium detectors can be mounted on the detection chamber unit to measure coincident gamma rays with the charged particles. For future experiments the beam line will be fitted with a new MCP detector placed directly after the bend following the interaction region. This addition will lead to even higher detection efficiencies. This is explained by the fact that this bend is followed by a doublet focusing device. The problem is however that the bend causes an additional defocusing which cannot be undone by the doublet. Introducing an additional MCP will therefore cancel this defocusing effect when the DSS module is not required for the experiments.

Appendix B

Paper: In Preparation

Efficient, high resolution resonance laser ionization spectroscopy using weak transitions to long-lived excited states

R. P. de Groote[1], M. Verlinde[1], G. Neyens[1], and others

[1]*KU Leuven, Instituut voor Kern- en Stralingsfysica, B-3001 Leuven, Belgium*

Laser spectroscopic studies of minute samples of radioactive nuclei require very efficient experimental techniques. In addition, high resolving powers are required to allow extraction of nuclear structure information. Here we investigate how using of weak transitions can enable resonance laser ionization spectroscopy to reach the required efficiency and precision. Using a simple model for resonance ionization we argue how such weak transitions We furthermore experimentally illustrate how using such weak transitions can lead to narrow experimental linewidths and improved experimental lineshapes. The role of the delay of the ionization laser with respect to the excitation laser is crucial: the use of a delayed ionization step allows for the best resolving powers and lineshapes.

I. INTRODUCTION

The study of the ground state properties of exotic nuclei forms one of the goals in contemporary nuclear physics research [1]. The theoretical description of the nucleus, a strongly interacting many-particle system, relies crucially on experimental input. Experimentally measuring the key observables is a challenging task; the most exotic nuclei have short radioactive half-lives and are typically only produced in minute quantities, accompanied by a large amount of unwanted contaminations. Typically, facilities that produce these exotic nuclei only allot a limited time to a given experiment, which means that study of the very exotic cases requires techniques that are both very selective and efficient. Many laser spectroscopic techniques have been applied in nuclear physics research [2, 3]. Resonance Ionization Spectroscopy (RIS) methods, which rely on multi-step laser ionization and subsequent ion detection, are typically more sensitive than methods based on fluorescence detection, motivating the development of numerous RIS experiments at online separators [4].

For techniques based on the detection of fluorescence photons emitted by excited atoms, excited states with a short lifetime are required to maximize the number of photons emitted while the radioactive beam travels in front of the detector. Often, this means that the transition that is used to excite the atom or ion has to be a strong transition, although weaker lines have sometimes been used. These strong transitions can usually be saturated with continuous-wave laser systems, even if the laser light has to be frequency-doubled or quadrupled. A downside of populating short-lived excited states is that they have a larger natural width. Furthermore, since power broadening is proportional to this natural linewidth in the steady-state limit [5], experimental linewidths increase significantly with the laser power. This means a balance must be struck between experimental efficiency and experimental resolving powers.

This article will demonstrate the advantages offered by weak transitions to long-lived excited states and will demonstrate the feasibility using weak transitions for efficient resonance laser ionization spectroscopy (section V). Additionally, two arguments in favor of using a weak transition in combination with a delayed ionization step will be discussed in detail. Firstly, it is possible to remove virtually all power broadening due to both lasers in a two-step RIS scheme by choosing a suitable delay for the ionization laser. Theoretical and experimental work on this topic was first suggested in [6] and then further proven and developed in [7, 8], and these findings will be complemented experimentally in section III. Secondly, lineshape distortions due to the presence of a strong ionizing laser field while the atom is excited by the first laser can cause significant lineshape distortions, which can be removed by using a delayed ionization step. This will be discussed in detail in section IV, with measurements performed on radioactive beams of Francium.

A simple model for resonance ionization will be used to illustrate some key concepts and help interpret the experimental results. This model will first be introduced.

II. A MODEL FOR RIS

The evolution of the population of a two level system irradiated by a laser tuned close to resonance can be calculated by solving the Shrödinger equations with the following Hamiltonian:

$$H = \frac{\hbar}{2}\begin{pmatrix} 0 & \Omega(t) \\ \Omega(t) & 2\Delta \end{pmatrix}, \tag{1}$$

where Δ is the laser-atom detuning and $\Omega(t)$ the coupling parameter of the two states, also called the Rabi frequency. When using linearly polarized laser light with a frequency ω_e, this coupling strength of the ground state level at an energy $\hbar\omega_0$ and an excited state at an energy $\hbar\omega_1$ can be calculated using

$$\begin{aligned}\Omega =& \sqrt{AP_e}\left(\frac{c}{\omega_1-\omega_0}\right)^{3/2}(2F_1+1) \\ &\times \sum_{m_{F_0},m_{F_1}} \begin{pmatrix} F_1 & 1 & F_0 \\ -m_{F_1} & 0 & m_{F_0}\end{pmatrix}\begin{Bmatrix} J_1 & F_1 & I \\ F_0 & J_0 & 1\end{Bmatrix},\end{aligned} \tag{2}$$

with F_i the total angular momentum of state i, () and {} respectively Wigner 3J and 6J symbols, A the Einstein A coefficient of the transition and $P_e(t)$ the power of the laser. With these definitions, $\Delta = \omega_1 - \omega_0 - \omega_e$.

A second laser with laser power $P_i(t)$ can ionize excited atoms, with a rate of $\Gamma = P_i(t)\sigma$, with σ the photo-ionization cross section of the excited state at the wavelength of the ionization laser. Photo-ionization requires modeling population loss, since population has to flow out of the two-level system, into the continuum. This requires a non-Hermitian Hamiltonian, given by

$$H = \frac{\hbar}{2}\begin{pmatrix} 0 & \Omega(t) \\ \Omega(t) & 2\Delta + 2S(t) - i\Gamma(t)\end{pmatrix}, \tag{3}$$

In this Hamiltonian S is the net dynamic Stark shift induced by both the ionization laser and excitation laser, with each laser contributing a shift proportional to the laser power [9, 10]. If there are no relaxation processes, the evolution of the system can be calculated using the time-dependent Shrodinger equation

$$\dot{\rho} = \frac{1}{i\hbar}\left(H\rho - \rho H^\dagger\right). \tag{4}$$

The right-hand side of this equation reduces to the more familiar commutator $[H, \rho]$ for Hermitian H. The populations of the states $P_i(t)$ are the diagonal elements of the density matrix, $P_i(t) = \rho_{ii}(t)$. Usually the spontaneous decay of the excited state to the ground state cannot be

neglected. Including incoherent relaxation processes into equation 4 can be done as follows:

$$\dot{\rho} = \frac{1}{i\hbar}\left(H\rho - \rho H^{\dagger}\right) + L(\rho). \tag{5}$$

For the two-level atom, L is given by

$$L = \begin{pmatrix} A\rho_{11} & -\frac{1}{2}A\rho_{01} \\ -\frac{1}{2}A\rho_{01} & -A\rho_{11} \end{pmatrix}, \tag{6}$$

where once again A is the Einstein A coefficient of the transition. This additional term in the equations of motion causes decay of the excited state to the lower-lying state, and exponentially dampens the coherence terms.

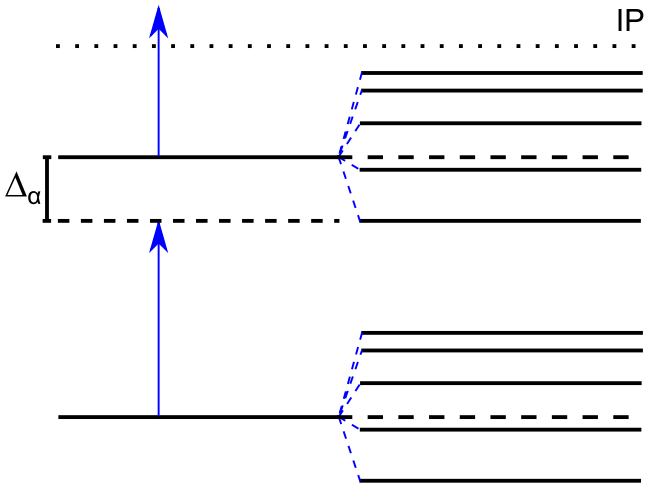

Figure 1. An atom with several levels in the ground-state and in the excited state multiplet.

These equations of motion can be generalized to systems with multiple levels in a ground- or excited state multiplet (see figure 1) in a relatively straightforward manner. Using greek indices for levels in the excited state multiplet and roman indices for the ground state multiplet, the Hamiltonian for such a system can be written down as

$$H_{ii}(t) = \hbar\omega_i \tag{7}$$
$$H_{ij}(t) = 0 \tag{8}$$
$$H_{\alpha\alpha}(t) = \hbar(S_\alpha(t) + \Delta_\alpha - \frac{i}{2}\Gamma(t)) \tag{9}$$
$$H_{i\alpha}(t) = H_{\alpha i}(t) = \frac{\hbar}{2}\Omega_{i\alpha}(t) \tag{10}$$
$$H_{\alpha\beta}(t) = -\frac{\hbar}{2}\Gamma(t)(q+i), \tag{11}$$

with $\hbar\omega_i$ and $\hbar\omega_\alpha$ the energy of the atomic states of the ground- and excited state multiplet, and $\Delta_\alpha = \omega_\alpha - \omega_e$. The off-diagonal terms in 11 are due to the embedding of structure into the continuum by the high-power ionization laser, and are characterized by a Fano parameter q [11]. This q parameter which plays a crucial role in laser-induced continuum phenomena and can be calculated from first principles (see e.g. [12–15]). The generalized form of the matrix L can be written down using the partial decay rates defined as

$$\gamma_{\alpha i} = \frac{4\alpha}{3}\frac{|\omega_\alpha - \omega_i|^3}{c^2}(2F_i+1)(2J_\alpha+1)(2J_i+1) \tag{12}$$
$$\times |\langle \alpha, L_\alpha || r || i, L_i \rangle|^2 \begin{Bmatrix} J_\alpha & 1 & J_i \\ F_i & I & F_\alpha \end{Bmatrix}^2 \begin{Bmatrix} L_\alpha & 1 & L_i \\ J_i & S & J_\alpha \end{Bmatrix}^2.$$

These rates can be calculated using the observation that the partial decay rates should sum to the Einstein A coefficient. Using this definition of the partial rates, L can be written down as

$$L(\rho)_{ii} = \sum_\alpha \rho_{\alpha\alpha}\gamma_{\alpha i} \tag{13}$$
$$L(\rho)_{\alpha\alpha} = -\sum_i \rho_{\alpha\alpha}\gamma_{\alpha i} \tag{14}$$
$$L(\rho)_{\alpha i} = -\frac{\rho_{\alpha i}}{2}\sum_j \gamma_{\alpha j} \tag{15}$$
$$L(\rho)_{\alpha i} = -\frac{\rho_{i\alpha}}{2}\sum_j \gamma_{\alpha j} \tag{16}$$
$$L(\rho)_{\alpha\beta} = -\frac{\rho_{\alpha\beta}}{2}\sum_j \gamma_{\alpha j} + \gamma_{\beta j} \tag{17}$$

These are the generalized equations that will be used for the simulations presented throughout this article.

III. POWER BROADENING AND DELAYED IONIZATION

In a two-step RIS scheme, there are two lasers that can broaden the resonance profiles. Power broadening due to the excitation laser in a closed two-level system is well understood in the steady-state limit. In this case, the linewidth of the optical resonance increases with the laser power [16]. For pulsed laser excitation, this result is not always valid [6]. Figure 2 illustrates this difference by presenting numerical solutions to the equations of motion using a Gaussian laser pulse of length T and an excitation pulse area of $20/T$.

Panel A of this figure shows the population of the first excited state, in absence of an ionization laser. Population is transfered to the excited state only in a relatively narrow band around $\Delta = 0$; for larger detuning the population transfer is transient (see panels C and D). Using the adiabatic theorem an estimate can be made for the range of detunings that result in a transfer to the excited state after the excitation laser pulse has passed. It can be derived that for a Gaussian shaped excitation laser pulse (in absence of ionization and spontaneous decay), this range is given by[8]

$$|\Delta| \lesssim \frac{\sqrt{\log(\Omega/\Delta)}}{T}. \tag{18}$$

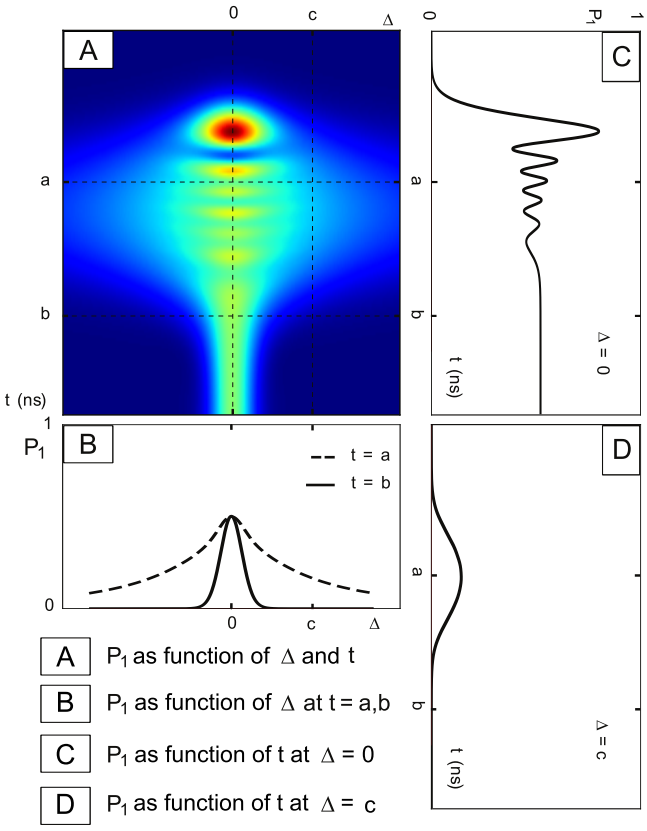

Figure 2. Panel A: Population of the excited state as function of time and laser detuning. Panel B: Population of the excited state as function of detuning at two different times. Panel C and D: Population of the excited state as function of time for $\Delta = 0$ and $\Delta = c$ respectively.

Since population excitations at detunings larger than the limits imposed by (18) are transient, this equation provides an estimate for the maximal width of the line shape. Relation (18) shows that for delayed (Gaussian) laser pulses the width of a line shape changes only logarithmically with power. On the other hand, for continuous wave irradiation, the spectral width always increases as the square root of the laser power [5]. This different power dependence represents a considerable improvement and therefore provides a strong argument in favor of delayed ionization. Note that using a delayed ionization strategy with short-lived excited atomic states can decrease the total ionization efficiency significantly.

Besides power broadening due to the excitation step, the ionization laser can also further broaden the optical lines if it is temporally overlapped with the excitation laser pulse, as can be understood in an intuitive way. Since the ionization laser couples the excited state to the continuum, the lifetime of this excited state is reduced. By virtue of the the Heisenberg energy-time uncertainty principle, this implies an increase in the energy uncertainty of the excited state. This energy uncertainty translates itself in a broadening of the optical resonance in the resonance ionization spectrum. If on the other hand the ionization laser is delayed with respect to the excitation laser step, this broadening does not occur, since the perturbing ionizing laser field is not present when the optical resonance is probed.

The goal of the experiments that are described below is to illustrate how power broadening can be mitigated by using a delayed ionization step. In this demonstration, the use of a weak transition to a long-lived excited state is crucial, since spontaneous decay from the excited state is minimal even with delayed ionization. This means that the resonance ionization process still occurs efficiently, which is critical for applications on exotic radioactive beams.

A. Experimental verification

1. *Description of the experiment*

In this first experiment, ^{63,65}Cu atoms were laser-ionized using a two-step resonance ionization process depicted in figure 3. This dataset was obtained at the IGISOL facility in Jyväskylä. The resonant 244.237 nm line from the $3d^{10}4s\ ^2S_{1/2}$ ground state to the $3d^9 4s4p\ ^4P^o_{1/2}$ state at 40943.78 cm^{-1} was followed by a 441.679 nm transition to the auto-ionizing $3d^9 4s\ ^3D\ 5s$ state at 63584.65 cm^{-1}. Given the long lifetime of the excited state (479(28) ns [17]), this dataset is well suited to study the behavior of power broadening for pulsed lasers and the role of the delay of the ionization laser. Furthermore, the laser system used to excite the transition could deliver an order of magnitude more laser power than the required saturation power density, resulting in clear power broadening effects. To produce the copper atoms, an electrothermally heated tantalum tube containing a sample of copper was heated. This atomic beam passed through a collimation slit and then orthogonally crossd the laser beams. Because of this orthogonal geometry and the collimation by the slit, Doppler broadening could be reduced significantly. An electrostatic lens extracted the laser ionized copper atoms and guided them to to an electron multiplier tube which served as the particle detector.

The laser system used for this work is described in detail in [18]. For the 244.237 nm line, an injection-locked Ti:sapphire laser system produced narrowband laser light (bandwidth $\approx$ 20 MHz), which was then frequency tripled. The master laser for this seeding cavity was a Matisse Ti:sapphire laser, which can be scanned continuously. The fundamental output of the laser was about 2.8 W at 10 kHz, which after beam transport losses resulted in up to 300 mW/cm^2 of tripled UV light entering into the atomic beam unit. Up to 1.6 W/cm^2 of 411.679 nm light was produced with a repetition rate of 10 kHz, using an intra-cavity frequency doubled pulsed Ti:sapphire laser. The two lasers were pumped using

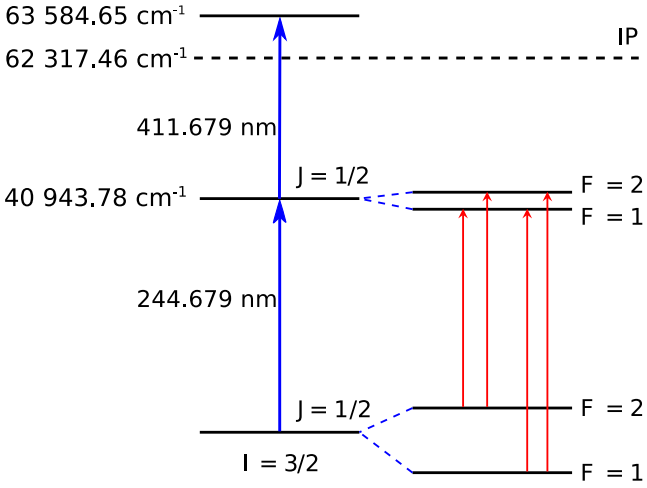

Figure 3. Ionization scheme used for ^{63}Cu and ^{65}Cu.

different Nd:YAG lasers, which introduces a jitter in the timing synchronization of both Ti:sapphire lasers of about 10 ns. This time jitter was of no consequence for the experiment. The pulse length of both lasers is typically 50 ns. The wavelength of the injection seeded TiSa was recorded using a High Finesse WS6 wavemeter and further monitored with a Toptica scanning Fabry Perot Interferometer FPI-100-0750-y with a free spectral range of 1 GHz. This interferometer was used to more precisely determine the wavelength of the laser as it was scanned.

2. *Discussion of results*

Several ionization spectra of and ^{63,65}Cu were obtained at different UV laser powers and for several time delays of the ionization step. The linewidth of the Gaussian component of the fitted Voigt profiles was found to be approximately 50 MHz for all experimental conditions. The linewidth of the Lorentzian component of the Voigt profile depends on the laser powers and delay time of the ionization step. The measurement performed at the lowest UV laser power (3 mW) and using a temporally overlapped excitation and ionization laser, resulted in a Lorentzian component with a width of 53.8(4) MHz. Increasing the power of the laser to 150 mW increased the linewidth of the Lorentzian component to 124.3(3) MHz. The two right-most components the full scan using this power is shown in figure 4 in red. Dots are the experimental data points, the full line is the fit. Keeping the laser power fixed, but delaying the ionization laser by 40(10) ns drastically reduces the width of the Lorentzian component to 21.0(3) MHz. Figure 4 also shows a zoomed-ion ionization spectrum at these settings in green. Note that the efficiency loss due to spontaneous decay is negligible due to the long lifetime of the excited state. This is the key advantage offered by using the weak transition to a long-lived state rather than a stronger transition.

The sharp reduction in linewidth as the ionization laser is delayed is explored in more detail with the inset of figure 4. This figure shows the measured linewidth of the Lorentzian component as a function the delay time, for a fixed laser power of 150 mW. The uncertainties on the extracted are smaller than the dots and of the order of 0.5 MHz. Delaying the ionization laser dramatically reduces the linewidth of the Lorentzian component; once the ionization laser is delayed more than about 40 ns, a constant linewdith of 19.2(0.1) MHz is obtained. Since this linewidth is less than the 53.8(4) MHz linewidth obtained at just at 3 mW, this directly provides evidence for the removal of power broadening of the UV laser, as well as the ionization laser. As the second step laser is futher delayed the efficiency of the RIS of course decreases gradually, but since the lifetime of the excited state is long, the efficiency loss is negligible for delays < 50 ns.

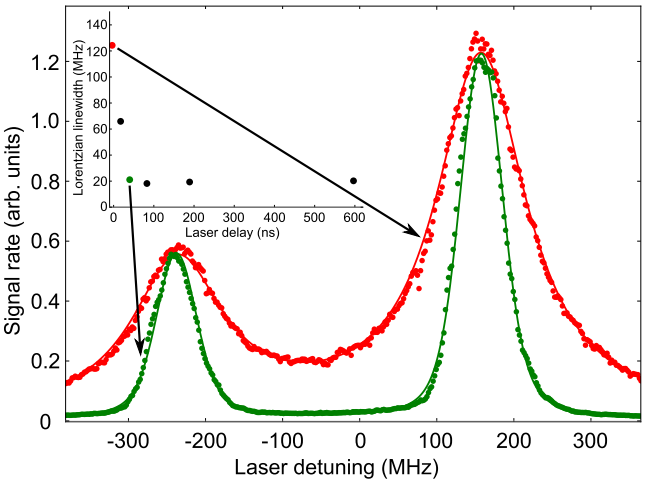

Figure 4. Two lines in the copper spectrum for temporally overlapping lasers (red) and with a delayed ionization step (green). Dots are the experimental data points, the full lines are the fit. The laser power was 150 mW / cm^2 for both measurements. A sharp reduction in the linewidth can be clearly seen, without loss in efficiency.
Inset: Linewdith of the lorentzian component of the voigt profile as function of the delay of the second laser pulse. By delaying the ionization step more than 40 ns the lorentzian linewidth reduces to an average 19(1) MHz.

IV. EXPERIMENTS ON LINESHAPE DISTORTIONS AND DELAYED IONIZATION

In addition to the power broadening effects discussed in the previous section, there is another effect to consider: the possibility of lineshape distortions induced by a high-power ionization laser. This section will discuss some experimental data which demonstrate lineshape distortions. We will also show that the basic model for laser ionzation of a two-level atom introduced in section I can be

used to qualitatively explain these distortions. Delaying the ionization laser in time with respect to the excitation laser removes the unwanted effects, since the distortion is induced after the atomic structure is already probed by the excitation laser. This will also be demonstrated with experimental data.

A. Description of the experiment

The possibility of ionization-related lineshape distortions, and how they can be removed by using a delayed ionization step, can be illustrated well with a RIS dataset obtained on radioactive beams of ^{221}Fr. The ionization scheme that was used is presented in figure 5, and consists of an excitation step from the $7s\ ^2S_{1/2}$ ground state to the $8p\ ^2P_{3/2}$ state at 23658.306 cm^{-1} using 422.7 nm light, and an ionization step that nonresonantly ionizes from the $8p\ ^2P_{3/2}$ state using pulsed 1064 nm light. The lifetime of the excited state is 83.5(1.5) ns, sufficiently long to justify the use of a delayed ionization pulse, even for work on radioactive samples produced in minute quantities.

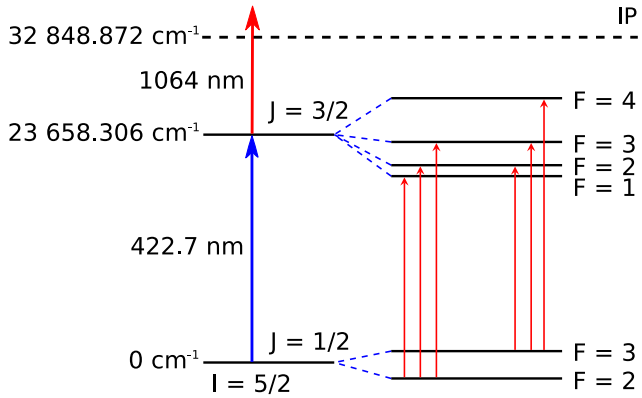

Figure 5. Ionization scheme used to excite and ionize ^{221}Fr.

A ^{221}Fr ion beam is produced by the ISOLDE facility at CERN by impinging 1.4 GeV protons onto a uranium carbide target. Francium ions diffuse out of this target and are then surface ionized in a hot capillary tube. The francium ion beam is then guided to a gas-filled linear Paul trap, where it is cooled and bunched. This beam is then accelerated to 30 kV and transported towards the CRIS experiment. The first stage of the CRIS experiment consists of neutralizing the ion beam through collisions with a hot potassium vapor. This is often required, since suitable transitions are usually easier to find for neutral atoms rather than ions. The non-neutralized fraction of the beam is electromagnetically deflected into a beam dump while the neutralized fraction is temporally and spatially overlapped with the laser beams in an UHV interaction region. This UHV is required to minimize collisional ionization that would otherwise result in a constant background in the hyperfine spectra. The laser-ionized atoms are then deflected onto a copper dynode, and the secondary electrons are detected using a microchannel plate (MCP) electron detector.

Because of the combination of an accelerated beam and the collinear overlap of the atom and laser beams, Doppler broadening is reduced to the point where it only contributes a few MHz to the total linewidth of the hyperfine structure spectra. The 422.7 nm laser light was produced by frequency doubling the output of a Matisse TS cw Ti-sapphire laser with a Wavetrain external cavity frequency doubler. This continuous light was chopped into pulses of variable length through the use of a pockels cell and subsequent polarization sensitive beam optics, described in detail in [19]. This experimental configuration was used to create light pulses with a pulse length 100 ns, at a repetition rate of 200 Hz. The 1064 nm light was produced using a dual-cavity Litron LPY 601 50–100 PIV laser system, operated at 100 Hz. After beam transport losses, 250 mW/cm^2 of continuous 422.7 nm laser light and 32 W/cm^2 of 1064 nm laser light reached the entry of the CRIS beamline.

B. Results

Figure 6 shows two measurements of the low-frequency component of the hyperfine structure of ^{221}Fr. The red spectrum is obtained with the ionization laser temporally overlapped with the excitation laser pulse, while the green spectrum was obtained with a delayed ionization pulse. The two pulse timings are illustrated in the inset of the figure. Using simultaneous laser pulses distorts the high-frequency side of the peaks, which display a clear asymmetry. This asymmetry disappears when the ionization laser is delayed, which indicates that the tailing is induced by the ionization laser.

The figure also shows simulations using the model introduced in section I. The ionization cross section σ was taken to be 1 Mb, which should at least be of the correct order of magnitude. The Fano q parameter was taken to be zero. The effective Stark shift S was tuned to give the best match with the experimental data; a final value of $S(t) \approx 4\Gamma(t)$ provided a good match. The simulations were also rescaled to the intensity of the highest peak in the experimental data.

Using these parameters, the asymmetric tail of the peaks is well reproduced, supporting the idea that the observed asymmetry is due to a Stark shift caused by the ionization laser. The intensity of the smallest resonance in the spectrum is not well reproduced by the model. The reason for this discrepancy is unclear.

As with the data on the copper isotopes, delaying the ionization step does not result in significant loss in efficiency, since the excited state is long-lived. The final linewidth of the optical resonances is 20(1) MHz. This linewidth could only be reached due to the removal of power broadening due to the delayed ionization and the

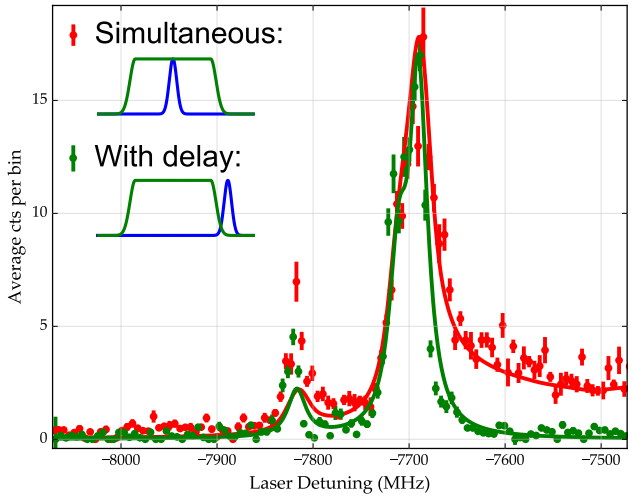

Figure 6. Resonance ionization spectra of the leftmost components of the hyperfine structure of ^{221}Fr, obtained with simultaneous laser pulses (red) and with a delayed ionization step (green). The solid lines are fits using the basic model for RIS presented in I.

removal of the lineshape-distorting AC Stark shifts. In turn, in a two-step resonance ionization scheme, this can only be done efficiently with a weak transition to a long-lived excited state.

V. EFFICIENT LASER EXCITATION AND IONIZATION WITH WEAK TRANSITIONS

Weak transitions have shown desirable features for laser spectroscopy purposes. In addition to the inherently small linewidth, weak transitions show no sign of efficiency loss when delaying the ionization pulse. This section will further argue that weak transitions to long-lived states can be excited with very high absolute efficiencies, comparable to efficiencies obtained with stronger lines.

Applying the model of section II, one obtains the steady state population of an excited level state in a two-level approximation:

$$P_{exc}(\Delta = 0) = \frac{\Omega^2}{A^2 + 2\Omega^2} \tag{19}$$

$$\propto \frac{IA}{A^2 + 2IA}, \tag{20}$$

$$= \frac{I/A}{1 + 2I/A}, \tag{21}$$

since $\Omega \sim \sqrt{IA}$, where A is the Einstein A parameter of the transition and I the laser intensity. Since, for a fixed laser intensity, this is monotonically decreasing function of A, weak transitions can achieve higher steady state population in the excited state. However, the irradiation time required to reach this steady state is longer than for strong transitions, though it also increases with laser power. Therefore, there are two strategies to consider when maximizing the efficiency of excitations using weak transitions. First of all, one can use high power pulsed laser systems which increase the rate at which the equilibrium population is reached, resulting in higher efficiency for short pulse lengths. This is the approach used for the first dataset in this article (see section III): a high-power pulsed laser can saturate the excitation step and therefore efficiently excite the system.

On the other hand, employing low powers but long interaction times, as in the experiment of IV, can offer high efficiency. This is illustrated in figure 7, which shows simulated ionization efficiencies for weak and strong transitions for a system with a ground state doublet and a single excited state, as a function of the pulse length using overlapping excitation and ionization lasers. With sufficiently long interaction times, weak transitions can be excited very effiently, with simulated ionization efficiencies better than or comparable to the efficiency obtained for short pulses and strong transitions. For separated lasers, the strong transition ionization efficiency never reaches that of the weak transition due to decay losses.

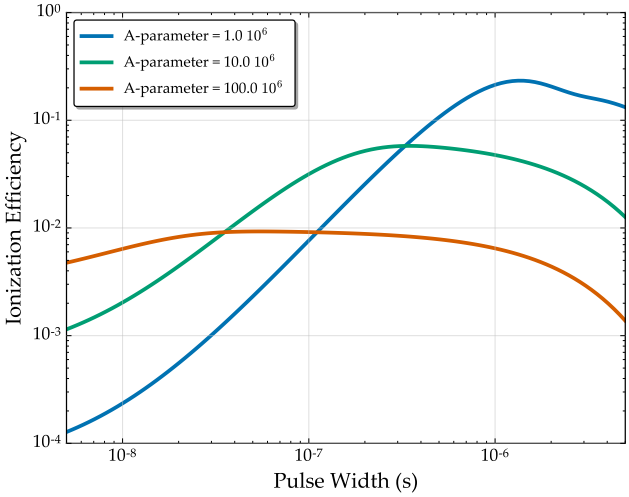

Figure 7. Ionization efficiency for small chopped cw-laser intensity, overlapping with the ionization pulse and variable pulse length for a ground and excited state, each consisting of 2 hyperfine sublevels. The laser is tuned to a single resonance frequency. Of the three transitions (in units of Hz), the weakest one will reach the highest efficiency if the pulse length is long enough. For extremely long laser pulses, the efficiency decreases due to optical pumping towards the other hyperfine level of the ground state.

VI. CONCLUSIONS

This article set out to argue that efficient resonance ionization spectroscopy with high resolving powers can

be achieved by using weak transitions to long-lived states. The advantage of these transitions is twofold.

Firstly, it is possible to remove virtually all power broadening due to both lasers in a two-step RIS scheme by choosing a suitable delay for the ionization laser. Secondly, lineshape distortions due to the presence of a strong ionizing laser field while the atom is excited by the first laser can cause significant lineshape distortions, which can be removed by using a delayed ionization step.

The long lifetime of the excited state ensures no significant efficiency losses occur due to the delay of the ionization laser. Experimental evidence for both advantages was presented and compared to a basic model for resonance ionization spectroscpy. The experimental data also illustrated that high efficiencies can be obtained using weak transitions.

ACKNOWLEDGMENTS

We acknowledge the support of the ISOLDE collaboration and technical teams. We are grateful to the COLLAPS collaboration for the use of their CW Ti:Sa laser system and wavetrain doubling unit. This work was supported by the BriX Research Program No. P7/12 and FWO-Vlaanderen (Belgium) and GOA 10/010 from KU Leuven, the Science and Technology Facilities Council consolidated grant ST/F012071/1 and continuation grant ST/J000159/1, and the EU Seventh Framework through ENSAR(506065). K. T. F. was supported by STFC Advanced Fellowship Scheme Grant No. ST/G006415/1 and ERC Consolidator Grant no. 648381. We acknowledge the financial aid from the Ed Schneiderman Fund at New York University.

[1] A. Bracco, P. Chomaz, J. Gaardh{\o}je, M. Makarow, P.-H. Heenen, G. Rosner, R. Kaiser, D. MacGregor, E. Widmann, and G. Korner, (2010).
[2] B. Cheal and K. T. Flanagan, Journal of Physics G: Nuclear and Particle Physics **37**, 113101 (2010).
[3] K. Blaum, J. Dilling, and W. Nörtershäuser, Physica Scripta **T152**, 014017 (2013).
[4] V. N. Fedosseev, Y. Kudryavtsev, and V. I. Mishin, Physica Scripta **85**, 058104 (2012).
[5] M. L. Citron, H. R. Gray, C. W. Gabel, and C. R. Stroud, Physical Review A **16**, 1507 (1977).
[6] N. Vitanov, Optics Communications **199**, 117 (2001).
[7] T. Halfmann, T. Rickes, N. V. Vitanov, and K. Bergmann, Optics Communications **220**, 353 (2003).
[8] I. I. Boradjiev and N. V. Vitanov, Optics Communications **288**, 91 (2013).
[9] N. B. Delone and V. P. Krainov, Physics-Uspekhi **42**, 669 (1999).
[10] S. Kumekov and V. Perel, Zh. Eksp. Teor. Fiz **81**, 1693 (1981).
[11] P. L. Knight and M. A. Lauder, Physics Reports **190**, 1 (1990).
[12] B. N. Dai and P. Lambropoulos, Physical Review A **36**, 5205 (1987).
[13] T. Nakajima, M. Elk, J. Zhang, and P. Lambropoulos, Physical Review A **50**, 915 (1994).
[14] L. P. Yatsenko, R. G. Unanyan, K. Bergmann, T. Halfmann, and B. W. Shore, Optics Communications **135**, 406 (1997).
[15] L. Yatsenko, T. Halfmann, B. Shore, and K. Bergmann, Physical Review A **59**, 2926 (1999).
[16] M. L. Citron, H. R. Gray, C. W. Gabel, and C. R. Stroud, Phys. Rev. A **16**, 1507 (1977).
[17] A. Kono and S. Hattori, Journal of Quantitative Spectroscopy and Radiative Transfer **28**, 383 (1982).
[18] V. Sonnenschein, *Laser Developments and High Resolution Resonance Ionization Spectroscopy of Actinide Elements*, Ph.D. thesis (2015).
[19] R. P. de Groote, I. Budinčević, J. Billowes, M. L. Bissell, T. E. Cocolios, G. J. Farooq-Smith, V. N. Fedosseev, K. T. Flanagan, S. Franchoo, R. F. G. Ruiz, H. Heylen, R. Li, K. M. Lynch, B. A. Marsh, G. Neyens, R. E. Rossel, S. Rothe, H. H. Stroke, K. D. A. Wendt, S. G. Wilkins, and X. Yang, Phys. Rev. Lett. **115** (2015), 10.1103/physrevlett.115.132501.

Bibliography

[1] R. De Groote. “Modeling and Simulation of Two-Step Resonance Ionization Processes using CW and Pulsed Lasers.” MA thesis. KU leuven,Belgium, 2013 (cit. on pp. 3, 4, 16, 19, 22–26, 31, 37, 44, 45, 66, 67, 72, 109).

[2] E.T. Jaynes and F.W. Cummings. *Comparison of quantum and semiclassical radiation theories with application to the beam maser.* Online Available, 1963, pp. 89–109 (cit. on p. 19).

[3] S. Gheysen G. Neyens and J. Odeurs. “Calculated hyperfine spectra for in-source laser spectroscopy and deduced magnetic moments and isomer shifts of Cu68 and Cu70 isomeric states.” In: *Physical Review C* 96 (2004) (cit. on p. 20).

[4] Y. B. Band. *Light and Matter, Electromagnetism, Optics, Spectroscopy and lasers.* Wiley, 2006 (cit. on pp. 25, 27, 31, 79).

[5] N.V. Vitanov et al. “Power broadening revisited: Theory and experiment.” In: *Optics Communications* 199 (2001) (cit. on pp. 26, 28).

[6] D. A. Steck. *Quantum and Atom Optics Textbook*. Center for Optics and Department of Physics, University of Orgeon (revision 0.10.2, 16 October 2015), 2007, p. 932 (cit. on pp. 31, 44, 47, 48, 60).

[7] J. Keeling. “Light-Matter Interactions and Quantum Optics.” In: *Course Notes on: Light-Matter Interactions and Quantum Optics*. University of St. Andrews: School of Physics and Astronomy, 2012, p. 123 (cit. on pp. 31, 44, 46, 60).

[8] B. E. King. “Angular Momentum Coupling and Rabi Frequencies for Simple Atomic Transitions.” In: *arXiv* (2008). arXiv: 0804.4528 (cit. on p. 32).

[9] P. M. Farrell and W. R. MacGillivray. “On the consistency of Rabi frequency calculations.” In: *Journal of Physics A: Mathematical and General* 28.1 (1995), pp. 209–221. ISSN: 0305-4470 (cit. on p. 32).

[10] P. R. Berman and V. S. Malinovsky. *Principles of Laser Spectroscopy and Quantum Optics*. Princeton University Press, 2011, pp. 375–382 (cit. on p. 33).

[11] J. D. Pritchard. “Cooperative Optical Non-lineariry in a blochaded Rydberg Ensemble.” PhD thesis. Department of Physics Durham University, may 14, 2011 (cit. on p. 34).

[12] Julio Gea-banacloche et al. “Electromagnetically induced transparency in ladder-type inhomogeneously broadened media: Theory and experiment.” In: *Physical Review A* 51.1 (1995) (cit. on p. 34).

[13] R. P. De Groote et al. “Use of a Continuous Wave Laser and Pockells Cell for sensitive High-resolution Collinear Resonance Ionisation Spectroscopy.” In: *Accepted for publication in Physical Review Letters* (2012) (cit. on pp. 35, 67, 117).

[14] N.B. Delone and V.P. Krainov. “AC Stark shift of atomic energy levels.” In: *Uspekhi Fizicheskih Nauk* 169.7 (1999), p. 753. ISSN: 0042-1294 (cit. on pp. 36, 63).

[15] W. Gins et al. In Preparation. 2016 (cit. on p. 43).

[16] B. W. Shore and N. V. Vitanov. “Overdamping of coherently driven quantum systems.” In: *Contemporary Physics* 47.6 (2006), pp. 341–362. ISSN: 0010-7514 (cit. on pp. 49, 57).

[17] R. F. Garcia Ruiz et al. “Laser Spectroscopy of neutron-deficient Sn isotopes.” In: *Proposal to the ISOLDE and Neutron Time-of-Flight Committee* (2016), pp. 1–13 (cit. on p. 65).

[18] V. Sonnenschein. “Laser Developments and High Resolution Resonance Ionization Spectroscopy of Actinide Elements.” PhD thesis. 2015 (cit. on pp. 69, 117).

[19] B. W. Shore. “Coherent manipulation of atoms using laser light.” In: *Acta Physica Slovaca* 58.3 (2008), pp. 243–486. ISSN: 03230465 (cit. on p. 75).

[20] T. Takekoshi et al. “Ultracold dense samples of dipolar RbCs molecules in the rovibrational and hyperfine ground state.” In: *Physical Review Letters* 113.20 (2014), pp. 1–5. ISSN: 10797114. arXiv: 1405.6037 (cit. on p. 76).

[21] K. Bergmann and T. Halfmann. “Population Switching between Vibrational Levels in Molecular Beams.” In: *Journal of Chemical Physics* 104 (1996) (cit. on p. 76).

[22] U. Gaubatz et al. “Population Switching between Vibrational Levels in Molecular Beams.” In: *Chemical Physics Letters* 149.5,6 (1988) (cit. on p. 76).

[23] A. S. Parkins et al. “Synthesis of arbitrary quantum states via adiabatic transfer of Zeeman coherence.” In: *Physical Review Letters* 71.19 (1993), pp. 3095–3098. ISSN: 00319007 (cit. on p. 76).

[24] N. V. Vitanov et al. “Laser-Induced Population Transfer by Adiabatic Passage Techniques.” In: *Annu. Rev. Phys. Chem* 52 (2001), pp. 763–809 (cit. on p. 77).

[25] K. Bergmann, N. V. Vitanov, and B. W. Shore. “Perspective: Stimulated Raman adiabatic passage: The status after 25 years.” In: *The Journal of Chemical Physics* 142.17 (2015), p. 170901. ISSN: 0021-9606 (cit. on pp. 76, 80, 94).

[26] K. Bergmann and T. Halfmann. “Population transfer through the continuum using laser-controlled Stark shifts.” In: *Optics Communications* 135 (1997), pp. 406–412 (cit. on p. 78).

[27] G. W. Coulston and K Bergmann. “Population transfer by stimulated Raman scattering with delayed pulses: analytical results for multilevel systems.” In: *J. Chem. Phys.* 96.5 (1992), p. 3467. ISSN: 00219606 (cit. on pp. 79, 87, 88).

[28] N. V. Vitanov and S. Stenholm. “Analytic properties and effective two-level problems in stimulated Raman adiabatic passage.” In: *Physical Review A* 55.1 (1997), pp. 648–660. ISSN: 1050-2947 (cit. on pp. 80, 81).

[29] N.V. Vitanov and S. Stenhom. “Properties of stimulated Raman adiabatic passage with intermediate-level detuning.” In: *Optics Communications* 135 (1996), pp. 394–405 (cit. on p. 83).

[30] I. I. Boradjiev and N. V. Vitanov. “Stimulated Raman adiabatic passage with unequal couplings: Beyond two-photon resonance.” In: *Physical Review A* 81.5 (2010), p. 053415. ISSN: 1050-2947. arXiv: arXiv:0909.4147v2 (cit. on pp. 83, 99, 100).

[31] C. Zener. “Non-Adiabatic Crossing of Energy Levels.” In: *Proc. R. Soc. Lond. A* 106 (1932), pp. 463–477 (cit. on p. 83).

[32] J. R. Rubbmark. “Dynamical effects at avoided level crossings: A study of the Landau-Zener effect using Rydberg atoms.” In: *Physical Review A* 23.6 (1981), pp. 3107–3117 (cit. on p. 83).

[33] J. P. Tae. “Transition probabilities at crossing in the Landau-Zener problem.” In: *Bulletin of the Korean Chemical Society* 26.11 (2005), pp. 1735–1737. ISSN: 02532964 (cit. on p. 83).

[34] P. Ivanov, N. Vitanov, and K. Bergmann. “Spontaneous emission in stimulated Raman adiabatic passage.” In: *Physical Review A* 72.5 (2005), p. 053412. ISSN: 1050-2947 (cit. on pp. 83, 95).

[35] L.P. Yatsenko, K. Bergmann, and T. Halfmann. “Population transfer through the continuum using laser-controlled Stark shifts.” In: *Optics Communications* 135 (1997), pp. 406–412 (cit. on pp. 84, 104).

[36] A. A. Rangelov, N. V. Vitanov, and E. Arimondo. “Stimulated Raman adiabatic passage into continuum.” In: *Physical Review A* 76.4 (2007), p. 043414. ISSN: 1050-2947 (cit. on pp. 84, 86, 104).

[37] C. E. Carroll and F. T. Hioe. “Coherent Population Transfer via the Continuum.” In: *Physical Review Letters* 68.24 (1992), pp. 3523–3526 (cit. on pp. 84, 104).

[38] B.W. Shore et al. “Coherent population transfer in multilevel systems with magnetic sublevels.” In: *Physical Review A* 52.1 (1995) (cit. on pp. 86, 88).

[39] J. Martin, B. W. Shore, and K. Bergmann. “Coherent population transfer in multilevel systems with magnetic sublevels.” In: *Physical Review A* 52.1 (1995) (cit. on pp. 86, 88).

[40] R. F. Garcia Ruiz. “Investigating the possible magicity of N = 32 , 34 in exotic Ca isotopes using laser spectroscopy methods.” PhD thesis. KU-Leuven, 2015 (cit. on p. 90).

[41] D.T. Yordanov. “From ^{27}Mg to ^{33}Mg: Transition to the Island of Inversion.” PhD thesis. KU leuven,Belgium, 2007 (cit. on p. 92).

[42] A. Kuhn, S. Steuerwald, and K. Bergmann. “Coherent population transfer in NO with pulsed lasers : the consequences of hyperfine structure , Doppler broadening and electromagnetically induced absorption.” In: *The European Physical Journal D* 70 (1998), pp. 57–70 (cit. on pp. 97, 99, 100).

[43] N. V. Vitanov and S. Stenholm. “Population transfer via a decaying state.” In: *Physical Review A* 56.2 (1997), pp. 1463–1471 (cit. on pp. 104, 105).

[44] S. Cottenier and M. Rots. *Hyperfine Interactions and their Applications in Nuclear Condensed Matter Physics: a microscopic introduction.* Lecture notes, unpublished, 2005 (cit. on p. 111).

[45] J. Papuga et al. “Shell structure of potassium isotopes deduced from their magnetic moments.” In: *Physical Review C* 90.3 (Sept. 2014), p. 034321. ISSN: 0556-2813 (cit. on p. 112).

[46] A. Nieminen et al. “On-line ion cooling and bunching for collinear laser spectroscopy.” In: *Physical review letters* 88.9 (Feb. 2002), p. 094801. ISSN: 0031-9007 (cit. on pp. 114, 115).

[47] C. Schultz, E. Arnold, and W. Borcherst. “Resonance ionzation spectroscopy on a fast atomic ytterbium beam.” In: *Journal of Physics B: Atomic, Molecular and Optical Physics* 4831 (24 1991) (cit. on p. 114).

[48] H. Franberg et al. “Off-line commissioning of the ISOLDE cooler.” In: *Nucl. Instr. and Meth. in Phys. Res. B* 266 (19-20 2008) (cit. on p. 115).

[49] T.E. Cocolios et al. “The Collinear Resonance Ionization Spectroscopy (CRIS) experimental setup at CERN-ISOLDE.” In: *Nuclear Instruments and Methods in Physics Research Section B: Beam Interactions with Materials and Atoms* 317 (Dec. 2013), pp. 565–569. ISSN: 0168583X (cit. on p. 116).

[50] K.M. Lynch et al. “CRIS: A new method in isomeric beam production.” In: *EPJ Web of Conferences* 63 (Dec. 2013). Ed. by C. Simenel et al., p. 01007. ISSN: 2100-014X (cit. on p. 117).

DEPARTEMENT NATUURKUNDE EN STERRENKUNDE
Celestijnenlaan 200d bus 2412
3001 HEVERLEE, BELGIË
tel. + 32 16 32 71 24
fys.kuleuven.be